Collapse phenomena of deformed cavitation bubbles

THÈSE N^{O} 8089 (2017)

PRÉSENTÉE LE 3 NOVEMBRE 2017
À LA FACULTÉ DES SCIENCES ET TECHNIQUES DE L'INGÉNIEUR
LABORATOIRE DE MACHINES HYDRAULIQUES
PROGRAMME DOCTORAL EN MÉCANIQUE

ÉCOLE POLYTECHNIQUE FÉDÉRALE DE LAUSANNE

POUR L'OBTENTION DU GRADE DE DOCTEUR ÈS SCIENCES

PAR

Outi SUPPONEN

acceptée sur proposition du jury:

Prof. J.-F. Molinari, président du jury
Dr M. Farhat, directeur de thèse
Prof. J. Katz, rapporteur
Prof. C.-D. Ohl, rapporteur
Prof. F. Gallaire, rapporteur

ÉCOLE POLYTECHNIQUE
FÉDÉRALE DE LAUSANNE

Suisse
2017

All things are so very uncertain, and that's exactly
what makes me feel reassured.

— Tove Jansson, *Moominland Midwinter*

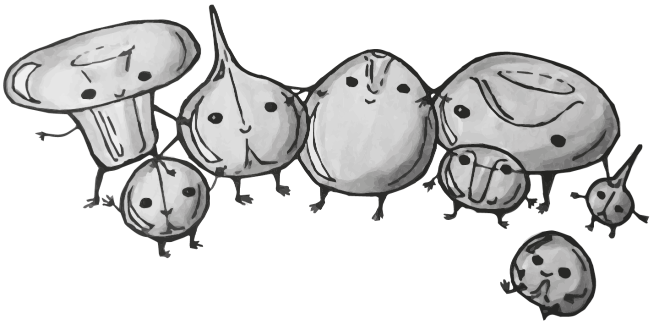

Acknowledgements

It is my pleasure to thank Mohamed for giving me, in addition to his full support, the best thing a doctoral student could possibly be granted by their advisor: trust.

I thank Prof. François Avellan for letting me pursue my doctoral studies in his laboratory.

I am sincerely grateful to Danail Obreschkow and Philippe Kobel for their enormous contribution in this work and for their priceless guidance and inspiration during my baby steps in research. I also thank Nicolas, Marc, and Aurèle in warmly welcoming me to their extraordinary Flash&Splash team. I am humbled to have taken part in something that started from pure passion within a close team of friends, which later evolved into an outstanding, internationally renowned science project. All together we have shared unique moments during the parabolic flight campaigns in Bordeaux and elsewhere, and I cannot thank them enough for these experiences.

I would like to thank my thesis jury members, my mentor Prof. Jean-François Molinari, Prof. Joseph Katz, Prof. Claus-Dieter Ohl, and Prof. François Gallaire, for challenging me in a constructive way during the defense and for triggering interesting discussions.

The project would not have been possible without the financial support of the Swiss National Science Foundation, nor without the unique opportunity to conduct experiments in variable gravity aboard parabolic flights by the European Space Agency. I appreciate all the advice I have received from the engineers at Novespace on the design of the experimental setup for the flights.

I am grateful to Prof. Sato and his lively laboratory at Tohoku University for our fruitful collaboration and for inviting me for an unforgettable visit in Sendai. I also thank Danail's colleagues at the International Centre for Radio Astronomy Research (UWA) for the warm welcome during my two memorable visits in Western Australia.

I thank Isabelle, not only for the invaluable administrative support, but also for the much-appreciated shared giggles and travel dreaming. I am grateful to Vincent for helping to find quick engineering solutions to the most absurd ideas I would ever come up with. I admire the exceptionally skilled technicians at LMH who helped re-build and improve the experimental setup in a short time: Maxime, Raymond, David, Victor, Christian and Louis. They truly taught me the importance of aesthetics in mechanical design.

Elena has been a true inspiration, solid support, and a great friend during my whole stay at LMH. I thank Swathi for sharing the final year joys of thesis writing with me and for being such a joyful and creative person. I am grateful to Quentin and Emmanuel for all the good moments shared during my first years at EPFL. I am thankful to Simon for the wonderful trip to the APS DFD conference in Portland and for sharing his unique knowledge on mountains and fish. I thank João, João, Ali, Sebastián, Siamak, and Alexis for the many laughs and interesting discussions on politics and life over lunches and beers, and I wish them the best of luck and fun with their own doctoral work. I thank Audrey, Keita, Pierre, Ebrahim, Loïc, Christian, Pascal, and Arthur for sharing all the lively coffee breaks in our windowless cafeteria. I am grateful to all the fun international visitors staying at our lab: Qin, Tao, Vinod, Chu, Takashi, Sayaka, Wu and Lu. I especially thank Foivos Koukouvinis for our successful collaboration. Thanks to the UNFoLD lab for adopting me as their honorary lab member over weekly lunches. I thank all my other colleagues, including previously graduated doctoral students, technicians, bureau d'études, engineers at the platforms, and master students for all the valuable help and for making my time at LMH such an enjoyable experience.

Extracurricular activities play a crucial role in the success of a doctorate. I therefore thank all the crazy skiers for the fabulous tours we have shared, in particular Fabrizio and Juan with whom I spent an unforgettable month in the Indian Himalayas exploring previously unskied mountains. I am grateful to all the runners who have encouraged me to run faster, longer and higher. I thank all the fencers at CAL and Unil/EPFL for receiving my aggression on the piste.

I am extremely grateful to all my friends. I will give special mentions to Sandra, Marcus, Marie, Blanca, and Stefano.

I do not know how I could express my gratitude to Céline. She just knows that without her I would not have achieved a doctorate. Marcello gets my special thanks for all the shared adventures in the past and in the future, and for introducing me to wonderful distractions from the routine, such as motorbiking, mountain biking, and mountaineering.

And finally, I thank the coolest and the most extraordinary family - Aura, Pippuri, Eloísa, Lauri, Marja, Sanna, maman, isi and co - who are my primary source of inspiration in pretty much everything.

Lausanne, October 2017 O. S.

Abstract

Cavitation bubbles are a topic of long-standing interest owing to the powerful phenomena associated with their collapse. Their unique ability to focus energy typically causes damage in hydraulic machinery (turbines, pumps, propellers, ...) but, if managed correctly, can also be beneficial in numerous applications such as cleaning practices and biomedical sciences. Here the complex problem of cavitation, often multi-scale both in time and space, is reduced to a simplified case study of the collapse of a single, initially spherical bubble. We study the bubble's energy distribution into its distinct collapse phenomena, namely the micro-jets, shock waves and luminescence, and aim to quantify and predict how such a distribution is affected by the bubble's deformation. Combining experiments with statistical analysis, numerical simulations and theoretical models, we seek to quantify and predict the key properties characterising each of the collapse phenomena.

The deformation of bubbles is characterised by the liquid micro-jets formed during their non-spherical collapse. A unified framework is proposed to describe the dynamics of such jets, driven by different external sources, through an anisotropy parameter ζ, which represents a dimensionless quantity of the liquid momentum at the bubble collapse (Kelvin impulse). The bubbles are carefully deformed in variable gravity aboard European Space Agency parabolic flights or by introducing surfaces nearby. Through high-speed visualisation, we measure key quantities associated with the micro-jet dynamics (e.g. jet speed, impact timing), which, upon normalisation, reduce to straightforward functions of ζ. This is verified by numerical simulations based on potential flow theory. Below a certain threshold, all of these functions can be approximated by useful power laws of ζ that are independent of the micro-jet driver.

For bubbles collapsing near a free surface, we identify and measure the shock waves generated through distinct mechanisms, such as the jet impact onto the opposite bubble wall and the individual collapses of the remaining bubble segments. The energy carried by each of these shocks is found to vary with ζ. We find that for bubbles that produce jets, the shock wave peak pressure may be approximated by the jet-induced water hammer pressure as a function of ζ. Following such an approximation, we also develop a semi-empirical model to explain the shock energy variation with ζ.

Finally, an innovative luminescence detection system is built to overcome the challenge of measuring the spectra (300-900 nm) of the weak, small, rapid and migrating flash light from individual bubble collapses. We find rapid quenching of the luminescence energy as a function of ζ. Surprisingly, the blackbody temperature of luminescence does not vary with ζ. Multiple peaks are measured within a time frame of approximately 200 ns, implying non-uniform gas compression during the collapse.

Overall, these results help in predicting bubble collapse characteristics in known pressure fields and can be useful for numerical benchmarking.

Key words: cavitation, bubble, collapse, micro-jet, shock wave, luminescence

Résumé

Les bulles de cavitation suscitent depuis longtemps un grand intérêt en raison des phénomènes énergétiques associés à leur implosion. Leur capacité extraordinaire à focaliser l'énergie peut conduire à l'endommagement de composants hydrauliques (turbines, pompes, hélices, ...). Toutefois, pour autant que leur dynamique soit maîtrisée, ces mêmes bulles de cavitation peuvent être bénéfiques dans de nombreuses applications telles que la médecine, la chimie ou l'industrie alimentaire.

Dans la présente étude, nous nous limitons au cas simplifié d'une bulle isolée, évoluant dans un liquide au repos en présence ou non d'un gradient de pression. Nous nous intéressons alors aux trois évènements majeurs associés à l'implosion d'une bulle de cavitation que sont les micro-jets, les ondes de choc et la luminescence. Notre but est de combiner l'observation expérimentale avec la simulation numérique et des modèles théoriques pour quantifier et prédire la fraction énergétique associée à chacun de ces phénomènes en fonction du degré de déformation de la bulle. Nous déformons la bulle à l'aide de la proximité d'une paroi solide ou d'une surface libre ainsi que la gravité variable, cette dernière étant réalisée aux vols paraboliques offerts par l'Agence Spatiale Européenne.

Nous proposons une relation semi-empirique unifiée pour décrire la dynamique des micro-jets en introduisant un paramètre d'anisotropie ζ qui représente la version adimensionnelle de la quantité de mouvement du liquide pendant l'implosion de la bulle (Kelvin impulse). Il est ainsi possible de prédire, entre autres, la vitesse du jet, l'instant de son impact avec l'interface et le déplacement du centre de la bulle, indépendamment de la source de déformation de la bulle.

L'émission des ondes de choc est examinée pour plusieurs degrés de déformation de la bulle à l'aide d'imagerie à haute vitesse et d'un hydrophone à large bande. Le cas particulier d'une bulle fortement déformée par une surface libre a révélé une succession complexe d'ondes de choc qui résulte de l'impact du jet sur l'interface (coup de bélier) et des implosions individuelles des fragments de la bulle. L'énergie de chacune de ces ondes de choc varie avec ζ. Nous trouvons que pour des bulles qui produisent des micro-jets, la pression maximale de l'onde de choc peut être approximée par la pression du coup de bélier en fonction de ζ.

Le dernier aspect couvert par la présente étude est celui de la luminescence. Le principal défi est de pouvoir détecter et mesurer le spectre (300-900 nm) de flashs lumineux émis par des sources minuscules, furtives et de très faible intensité. Pour ce faire, nous avons développé un système optique innovant qui utilise un miroir parabolique pour amplifier la lumière collectée et permet d'estimer la température d'une bulle avec une précision inégalée. Les résultats révèlent une décroissance rapide de l'énergie de la luminescence en fonction de ζ. Étonnamment, la température, estimée à l'aide de l'approximation du corps noir, ne varie pas avec ζ. En outre, l'analyse de la luminescence à l'aide d'une photodiode rapide révèle l'existence de plusieurs flash lumineux dans un intervalle d'environ 200 ns, suggérant une compression non-uniforme du gaz au stade final de l'implosion.

Dans l'ensemble, nos résultats permettent de mieux décrire et prédire les évènements caractéristiques de l'implosion d'une bulle de cavitation en présence d'un gradient de pression. Ils peuvent également servir de référence pour des études numériques.

Mots clefs : cavitation, bulle, implosion, micro-jet, onde de choc, luminescence

Contents

Acknowledgements **i**

Abstract **iii**

1 Introduction **1**
- 1.1 Cavitation: from hydraulic machinery to medicine 1
- 1.2 The collapse of a single bubble 2
- 1.3 Investigating bubble dynamics 5
  - 1.3.1 Theoretical models 5
  - 1.3.2 Numerical methods 7
  - 1.3.3 Experimental methods 7
- 1.4 Variable gravity aboard parabolic flights 9
- 1.5 Objective 10
- 1.6 Thesis outline 10

2 Micro-jets **11**
- Paper: Scaling laws for jets of single cavitation bubbles 11
- 2.1 Introduction 12
- 2.2 The diverse origins of micro-jets 13
- 2.3 Experimental set-up 16
- 2.4 Qualitative classification of jetting regimes 17
  - 2.4.1 Weak jets ($\zeta \leq 10^{-3}$) 18
  - 2.4.2 Intermediate jets ($10^{-3} < \zeta < 0.1$) 20
  - 2.4.3 Strong jets ($\zeta > 0.1$) 22
- 2.5 Quantitative analysis of jet dynamics 24
  - 2.5.1 Numerical simulation 25
  - 2.5.2 Jet impact time 28
  - 2.5.3 Jet speed 30
  - 2.5.4 Bubble displacement 32
  - 2.5.5 Bubble volume at jet impact 32
  - 2.5.6 Vapour-jet volume 35
- 2.6 Discussion 35
  - 2.6.1 Power-law approximations 35
  - 2.6.2 Application of scaling relations 38

2.6.3 Limitations 39
2.7 Conclusion 40
2.8 Appendix 41
2.8.1 Mathematical derivations 41
2.8.2 Numerical data 43

3 Shock waves 45
Paper: Shock waves from nonspherical cavitation bubbles 45
3.1 Introduction 46
3.2 Experimental methods 47
3.3 Detailed observations 50
3.3.1 Spherical collapse 50
3.3.2 Non-spherical collapse: Bubbles near a free surface 52
3.3.3 Energy distribution and event timings 57
3.4 Models for shock energy and pressure 60
3.5 Discussion 65
3.6 Conclusion 66

4 Luminescence 67
Paper: Luminescence from cavitation bubbles deformed in uniform pressure gradients 67
4.1 Introduction 68
4.2 Experimental setup 69
4.3 Spectral analysis in variable gravity 73
4.4 Time-resolved measurements 77
4.5 Discussion 82
4.6 Conclusion 86

5 Conclusion and perspectives 87
5.1 Conclusion 87
5.2 Perspectives 88

Bibliography 91

Curriculum Vitae 104

1 Introduction

1.1 Cavitation: from hydraulic machinery to medicine

Cavitation is a fascinating phenomenon that appears in countless physical and engineering flows involving pressure fluctuations. It literally means the formation of vapour cavities caused by the rupturing of the liquid due to a local pressure decrease below its vapourisation pressure [1, 2, 3]. Cavitation is analogous to boiling, where the liquid is vapourised due to a temperature rise over the boiling temperature, which, in fact, results in an increase of the vapourisation pressure. A key difference between cavitation and boiling is the way the vapour bubble formation and collapse occur in practice. The bubble dynamics associated to boiling is constrained by the difficulty to experience rapid and uniform temperature changes in the liquid. Cavitation, on the other hand, is dominated by inertial effects in the surrounding liquid where the pressure can change abruptly. These pressure changes can make the unstable cavitation bubbles suddenly find themselves in crushingly high pressure environments and experience a violent collapse, yielding powerful mechanical and chemical effects that will be discussed hereafter.

The study of cavitation began from marine technology where liquid vapourisation was observed around ship propellers running too fast. Many unwanted effects were detected, such as thrust reduction, propeller blade erosion, and underwater noise [4]. These effects can cause damage and a performance breakdown in numerous other types of hydraulic machinery, including hydraulic turbines [5], pumps [6], and artificial heart valves [7]. The associated flows typically cavitate within their low-pressure zones, such as regions of flow separation [8] and vortex cores [9]. Cavitation is known to be a problem also in liquid-propelled rocket engines [10], in lubricated bearings [11], and in trees [12]. Other victims of cavitation are the preys of a snapping shrimp (*alpheus heterochaelis*) or that of a mantis shrimp (*odontodactylus scyllarus*). These shrimps have understood the power of cavitation by defeating their prey through the rapid closure or movement of their claws that vapourises the liquid and thereby produces damaging cavitation phenomena [13, 14].

Despite having traditionally represented an adverse issue, more recent discoveries have found beneficial uses of the intense phenomena and the unique energy focusing associated with the collapse of cavitation bubbles. For instance, the biomedical field benefits from their remarkable properties for destroying kidney stones during lithotripsy by shock waves or by high-intensity focused ultrasound [15, 16, 17], for emulsifying the natural optical lens during cataract surgery [18], and for delivering drugs and targeting cells in a highly controllable way, which provides a new technique for cancer and gene therapy [19, 20, 21, 22, 23, 24, 25]. Laser-induced bubbles have a unique property for making small and precise incisions, which is used, for instance, in intraocular surgery [26]. Cavitation also offers interesting properties for cleaning surfaces [27, 28] or for micro-fluidic applications, such as for micro-fluidic pumps using a single cavitation bubble in the proximity of a concave free surface meniscus [29, 30]. The resulting extremely thin and fast jets emerging from the surface open paths for new methods in needle-free drug injection [31] or as an alternative to ink-jet printing [32]. Owing to their intense interior heating and compression, which yield the rupturing of water molecules, cavitation bubbles may serve as catalytic hosts for unique chemical reactions, offering a potential for environmental remediation [33] or fabrication of nanomaterials [34]. Cavitation may also be used to increase the efficiency of beer-brewing [35], and is known to be responsible of the fun sound associated with knuckle joint cracking [36].

1.2 The collapse of a single bubble

As it has now become clear, cavitation occurs in many places and there is a plethora of applications being harmed by it or benefiting from it. However, cavitation is a complex phenomenon, often involving multiple scales both in time and space, generally presenting itself as bubble clusters or clouds, and typically occurring in a liquid with strong pressure gradients. Many factors are in play in its formation and dynamics, such as the liquid gas content and the concentration and distribution of nucleation sites, and controlling its location and amount is challenging. Therefore, it can useful to reduce the problem of cavitation to a simplified case study, which is investigating the collapse of a single, initially spherical cavitation bubble in a liquid at rest.

The typical dynamics taking place during the lifetime of a single cavitation bubble collapsing spherically is illustrated in Figure 1.1. After nucleation (the birth of the bubble) under the effect of, say, a transient tension (negative pressure) wave or from a laser-induced plasma, a bubble expands. During the expansion, work is done against the ambient pressure p_∞, due to which the growth is decelerated and halts at a maximum bubble radius R_0. In this state, the liquid-bubble system has acquired a corresponding amount of potential energy (often simply referred to as 'bubble energy', $E_0 = (4\pi/3)R_0^3\Delta p$, where $\Delta p = p_\infty - p_v$ and p_v is the vapour pressure of the liquid) for it can perform positive work and gain kinetic energy by starting to shrink. During most of the growth and the shrinking of the bubble, it is generally assumed that the vaporisation-condensation processes maintain the vapour at its saturation pressure. During the shrinking, or *collapse* phase, the bubble interface accelerates towards its centre due to the driving ambient pressure. The time of the shrinking phase is denoted by the collapse time T_c, which, for a laser-induced bubble such as in Figure 1.1, happens to

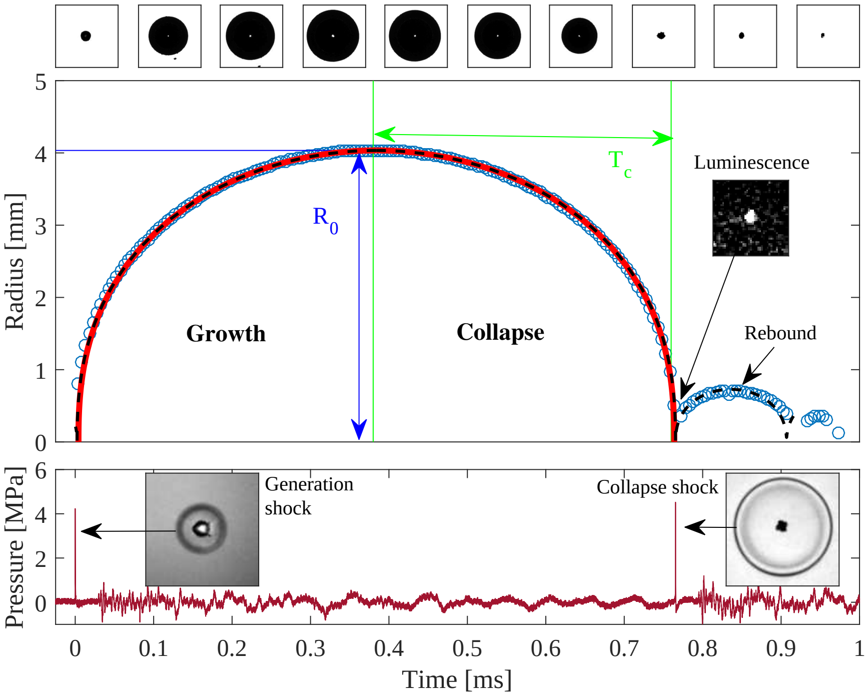

Figure 1.1: Shadowgraph visualisation of a spherical bubble growth and collapse (*top*), with interframe time 112 μs. The measured radial evolution (*middle*) and hydrophone pressure signal (*bottom*) are shown as a function of time. Rayleigh model in equation (1.1) (solid red line) and Keller-Miksis (KM) model in equation (1.7) (dashed black line), with p_{g_0} = 3.6 Pa determined by fitting with the observed rebound, are compared with the measured radial evolution. Between $T = 0$–T_c, the models are mirrored across the axis at $T = T_c$. The hydrophone signal has been shifted by 30 μs to account for the delay caused by the shock's propagation over a distance of 44.5 mm from the bubble.

be (quasi-)identical to the growth time. Eventually, the inward acceleration results in some violent collapse effects, which represent the following peculiar phenomena taking place often in an extremely short period of time:

Rebound - The bubble may contain non-condensible gases depending on its origin [37] and the properties of the liquid (e.g., dissolved gas content). Furthermore, it could also be that the vapour trapped inside the cavity may behave like a non-condensible gas, if the vapour condensation rate is not sufficiently high to keep up with the reduction of bubble volume during the last phase of its collapse [38]. Following the collapse, the bubble's interface is bounced off from these gaseous contents that act as a spring, leading to the expansion of a rebound bubble that grows and collapses several times, until its motion is damped due to viscous dissipation.

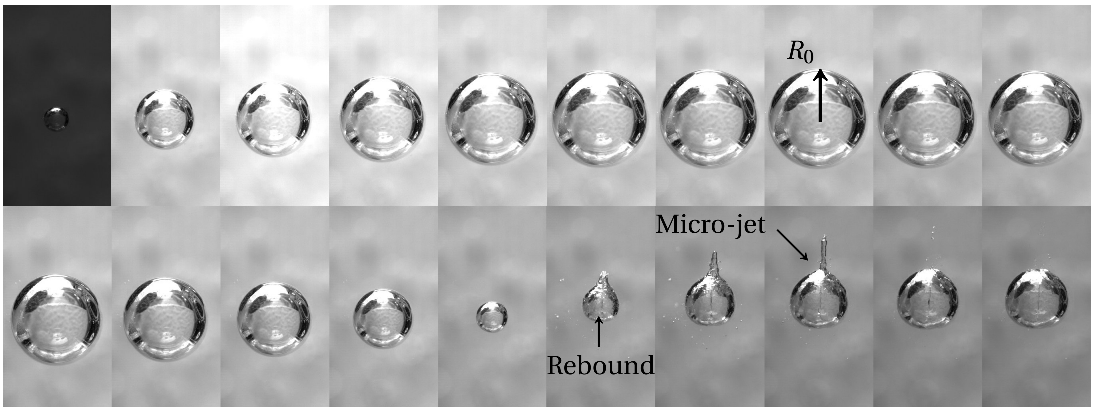

Figure 1.2: An example visualisation of a bubble collapsing non-spherically due to the gravity-induced pressure gradient, producing a micro-jet that emerges during the rebound phase. The interframe time is 360 μs and the maximum bubble radius R_0 is 5.6 mm.

Shock waves - Acoustic transients, or shock waves, are produced due to the compressibility of the liquid and the high velocities associated with the rapid bubble collapse [39]. The associated pressures, able to reach values on the order of GPa [40, 41], can be highly damaging to nearby surfaces. Figure 1.1 shows an example of a hydrophone measurement capturing the shock wave from a spherical bubble collapse. The collapse shock wave is often referred to as a single event, yet a non-spherically collapsing bubble may develop several distinct shock waves from multiple locations [42]. Note that a shock is also emitted at the generation of a laser-induced bubble (first peak in the hydrophone signal of Fig. 1.1) owing to its explosive growth, which first compresses the liquid in its immediate surroundings before radially accelerating it.

Luminescence - The gaseous contents of the bubble may be violently compressed during the last stages of its collapse, (nearly) adiabatically heating them to temperatures of several thousands of degrees, resulting in emission of light [43]. This light radiation carries the only information about the thermal state of the bubble during these stages. The exact mechanism or mechanisms behind the generation of the luminescent flash has not yet been fully revealed [44].

Micro-jets - When the spherical shape of the bubble is broken by pressure field anisotropies induced by nearby surfaces [45] or inertial forces such as gravity [45, 46], the bubble may be pierced by a re-entrant liquid jet during its collapse. This is due to one part of the bubble's interface advancing faster towards the bubble centre than the rest during the collapse. After its piercing, the micro-jet usually entrains a protrusion of the bubble's gaseous contents during its propagation away from the rebounding bubble [47]. An example of a non-spherically collapsing bubble producing an upward micro-jet is shown in Figure 1.2.

It has been shown that most of the energy of a spherically collapsing bubble is either carried away by a shock wave or used to form a rebound bubble [48, 49]. However, understanding how this energy distribution is affected by the bubble's deformation by external sources or by its initial sphericity remains poor.

1.3 Investigating bubble dynamics

1.3.1 Theoretical models

George Stokes and his students in 1847 [50], and later Lord Rayleigh precisely a century ago [51], were the first ones to model the motion of an empty, spherically collapsing bubble in an infinite volume of incompressible, inviscid and irrotational liquid with neglected surface tension and thermal effects, the latter having established the widely used Rayleigh equation:

$$\rho\left(R\ddot{R}+\frac{3}{2}\dot{R}^2\right)=-p_\infty, \tag{1.1}$$

where $R(T)$ is the radius of the bubble as a function of time T, p_∞ is the pressure of the liquid and ρ the liquid density. The above equation can be derived from the Navier-Stokes equations [2] or from energy conservation [52]. Equation (1.1) extends to the case of a vapour-filled bubble with a constant inner pressure p_v if the right-hand side of the equation is replaced by $p_v - p_\infty$ $(= -\Delta p)$. The Rayleigh equation provides a useful relation between the initial bubble radius R_0 and the bubble's collapse time T_c when integrated from time 0 to T_c and from radius R_0 to 0, which reads

$$T_c = \xi R_0 \left(\frac{\rho}{\Delta p}\right)^{1/2}, \tag{1.2}$$

where $\xi \approx 0.91468$ is the constant Rayleigh factor (see section 2.8.1 for the derivation). Equation (1.2) implies that for a given radius and liquid density, a bubble collapsing with a higher driving pressure Δp has a shorter lifetime. Consequently, for a bubble collapsing in a pressure gradient where one of the bubble sides is subject to a higher pressure than its opposing side, one would, intuitively speaking, expect differences in the collapse speed for the different parts of the interface, which would lead to the formation of a micro-jet [53].

An analytical solution to the Rayleigh equation, based on earlier approximations [54, 55, 56], was proposed only very recently [57]. When expressed in normalised coordinates, where $r \equiv R/R_0$ and $t \equiv T/T_c$, the Rayleigh equation may be simplified into a dimensionless first order differential equation:

$$\dot{r}^2 = \frac{2}{3}\xi^2\left(r^{-3}-1\right), \tag{1.3}$$

which satisfies $\dot{r} \propto r^{-3/2}$ [55]. The asymptotic behaviour of equation (1.3), as $r \to 0$ (and $t \to 1$), is [54, 55]

$$r(t) \cong \left(1-t^2\right)^{2/5}, \tag{1.4}$$

which actually approximates the full evolution of $r(t)$ within 1% error [55]. This interesting approximation will be used throughout the present work.

The Rayleigh equation includes a singularity as $T/T_c \to 1$, resulting in $R \to 0$ and $\dot{R} \to \infty$, a behaviour that is not realistic. Equation (1.1) was later improved by Plesset to include non-condensible gas inside the bubble, which prevents the bubble from becoming infinitely small, and to take into account surface tension and liquid viscosity, yielding the model commonly known as the Rayleigh-Plesset equation [58] that reads

$$\rho\left(R\ddot{R}+\frac{3}{2}\dot{R}^2\right)=p_B-p_\infty-\frac{2\sigma}{R}-4\mu\frac{\dot{R}}{R}, \tag{1.5}$$

where σ and μ are, respectively, the surface tension and the dynamic viscosity of the liquid, and p_B is the time-dependent pressure inside the bubble, which is assumed to be uniform and generally considered to comprise vapour (maintained at its constant saturation pressure) and non-condensible gas, i.e., $p_B = p_g(T) + p_v$. Using the adiabatic hypothesis, the time-dependent partial pressure of the gas may be expressed as $p_g = p_{g_0}(R_0/R)^{3\gamma}$, where p_{g_0} is the initial partial pressure and γ the adiabatic index of the non-condensible gas inside the bubble.

Numerous different compressible versions of the Rayleigh-Plesset model have been proposed [59, 60, 61, 62], many of which can be derived from a class of first-order models [63, 64, 62]:

$$\left[1-(\lambda+1)\frac{\dot{R}}{c}\right]R\ddot{R}+\frac{3}{2}\left[1-\frac{1}{3}(3\lambda+1)\frac{\dot{R}}{c}\right]\dot{R}^2=\frac{1}{\rho}\left[1-(\lambda-1)\frac{\dot{R}}{c}+\frac{R}{c}\frac{\mathrm{d}}{\mathrm{d}t}\right]\left(p_B-p_\infty\right)+O(c^{-2}), \tag{1.6}$$

where λ is an arbitrary parameter, c is the sound speed in the liquid and O is the order of error. One special case of this class is the Keller-Miksis model [60] where $\lambda = 0$, which, with $p_B = p_g + p_v$, reads

$$\left(1-\frac{\dot{R}}{c}\right)\rho R\ddot{R}=\left(p_g+p_v-p_\infty\right)\left(1+\frac{\dot{R}}{c}\right)+\frac{R\dot{p}_g}{c}-\left(3-\frac{\dot{R}}{c}\right)\frac{\dot{R}^2\rho}{2}. \tag{1.7}$$

The above equation will be used throughout this work. An example of the Keller-Miksis model compared with the observed radial evolution of a bubble is given in Figure 1.1.

Numerous further improvements have been proposed for these models, taking into account evaporation, condensation and mass transfer, source of bubble generation, chemical reactions, the evolution of the gas concentration within the bubble [41, 65, 66], and bubbles collapsing in finite volumes [52]. However, all these analytical models monitor the evolution of bubbles assumed to remain spherical, whilst often they deviate from the spherical shape due to the presence of strong anisotropies in the pressure field of the surrounding liquid.

It is challenging to derive analytical models for non-spherically collapsing bubbles. However, the concept of Kelvin impulse [45, 67, 68, 69] has been shown to quite conveniently quantify a non-spherical collapse. Kelvin impulse is the integrated linear momentum acquired by the surrounding liquid during the growth and the collapse of the bubble. For a perfectly spherically collapsing bubble that undergoes no translational motion during its lifetime, the Kelvin impulse equals zero. Despite being an integral value, it gives information on the gross motion of the bubble during its asymmetric collapse. It is a concept that will be largely used throughout this work.

1.3.2 Numerical methods

More precise dynamics associated with non-spherically collapsing bubbles can be reproduced though numerical simulations, as has been investigated in numerous studies in the past, of which only a small fraction is mentioned here. Boundary integral method (BIM), which discretises only the bubble surface with a piecewise-linear representation, has been widely used for this purpose. The first studies used incompressible versions, calculating the bubble shape evolution as long as the bubble is singly connected, i.e., up to the moment of the micro-jet impact onto the opposite bubble wall [70, 71, 72]. These have also been improved to model the evolution of the bubble even after the jet impact [73, 74] and to take into account liquid compressibility [75, 76, 49]. Also many domain approaches have been used to simulate non-spherical bubbles in compressible liquids, coupled with various interface-capturing schemes [77, 78, 79, 80, 81, 82, 83, 84, 85, 86, 87, 88, 89, 90]. These studies have investigated the interaction of bubbles with different types of boundaries with various shapes, bubbles collapsed under the effect of shock waves, among other scenarios. However, the sole use of numerical computations is not always sufficient or cost-efficient to predict the bubble collapse outcomes for a given application, and they need to be carefully validated by experimental observations.

1.3.3 Experimental methods

Many different ways exist to produce on-demand single bubbles of various scales for experimental cavitation studies. The most commonly used methods are expanding existing nuclei (e.g., air bubbles) by ultrasound [91, 92, 28] or a transient tension wave [93], focused lasers [94, 41, 71, 95, 96, 97], electric discharges [52, 98, 99], and underwater explosions [100, 101, 102]. Applying ultrasound sets the liquid locally into tension and, if positioning the standing waves correctly, one may create a stably oscillating, usually sub-millimetric single bubble which, thanks to its numerous successive life cycles, facilitates the study of, e.g., luminescence or chemical reactions. Following the same principle, a transient tension wave can be applied on an existing gas nucleus by, for example, reflecting a compression wave from a free surface (which may induce secondary cavitation, such as in ref. [103]) or by the 'tube arrest'-method [93]. Millimetric laser-induced vapour bubbles are produced as a focused pulsed laser triggers an optical breakdown that ruptures the liquid. Here enough laser energy is absorbed in the focal point that the liquid locally heats up to ionising temperatures and thereby produces a plasma, from which the explosively growing vapour bubble emerges. Electric discharge is another energy-depositing method that creates a plasma between electrodes, yielding the explosive growth of a vapour bubble that can typically reach centimetric sizes. Underwater explosions generate very large, meter-scaled bubbles using explosives.

The bubbles in the experiments presented in this work are generated with a focused laser. Producing bubbles this way has many advantages for studying the physics of cavitation bubbles. Laser-induced bubbles can be generated to a precise location, and their dynamics can be let evolve freely without the presence of an external sound field or neighbouring objects or surfaces. They can be made relatively large (millimetre scale), thereby increasing the spatio-temporal resolution of the measurements, and to collapse with controlled, adjustable deformations. The (dis-)similarity between laser-induced bubbles or other energy deposition methods with hydrodynamic cavitation bubbles (i.e., bubbles generated by low pressures) has, however, caused some concern when used for understanding the physics underlying cavitation. There exists evidence that lasers and sparks produce gases [37], and the resulting bubbles are generated by ionising temperatures [104], which could yield important thermal effects. However, the experimental observations from laser-induced bubbles (in our experiment) agree with Rayleigh's model to a very high accuracy (< 1 %), even when only vapour is accounted for inside the bubble [97]. This implies that the produced gases remain small in quantity, and after the initial plasma generation, the bubble contents quickly cool down to ambient temperature and condensate. Indeed, considering the typical expansion ratio from the initial plasma ($R_0/R_{\text{plasma}} \sim 100$), if an adiabatic expansion and ideal gas are assumed, an excess temperature of, say, 16000 K [104] would cool down to a temperature in the order of 10 K already as the bubble reaches 10% of its maximal expansion radius (i.e., a 1000-fold volume expansion!), which happens in the first 1% of its lifetime.

Large laser-induced bubbles typically have an important growth in shape instabilities near the end of the collapse, likely arising from anisotropy and perturbations in the initial plasma (e.g., due to the focal region of the laser being cone-shaped [105]), which can yield bubble splitting [106, 104]. The bubble surface during its growth phase, when $\dot{R} > 0$, is generally rather stable, allowing a bubble that is initially not spherical to assume a highly spherical shape at its maximum expansion. During the collapse ($\dot{R} < 0$), however, the surface modes become amplified, their growth rates being sensitive on the initial perturbations (see stability analysis by Plesset and Mitchell [107]). In fact, the effect of the initial shape of laser-induced bubbles on their collapse dynamics has been studied previously for the purpose of engineering micro-fluidic flows on-demand [108].

In order to maximise the control over the bubble's level of deformation, one must i) minimise the effect of the initial shape perturbations on the bubble's deformation - for this we need a highly point-like initial plasma with a high-convergence focusing device such as a parabolic mirror [97], in contrast to the more conventional use of converging lenses; and ii) control the external perturbations, with the introduction (or removal) of nearby boundaries and with varying (or suppressing) the gravity-induced hydrostatic pressure gradient.

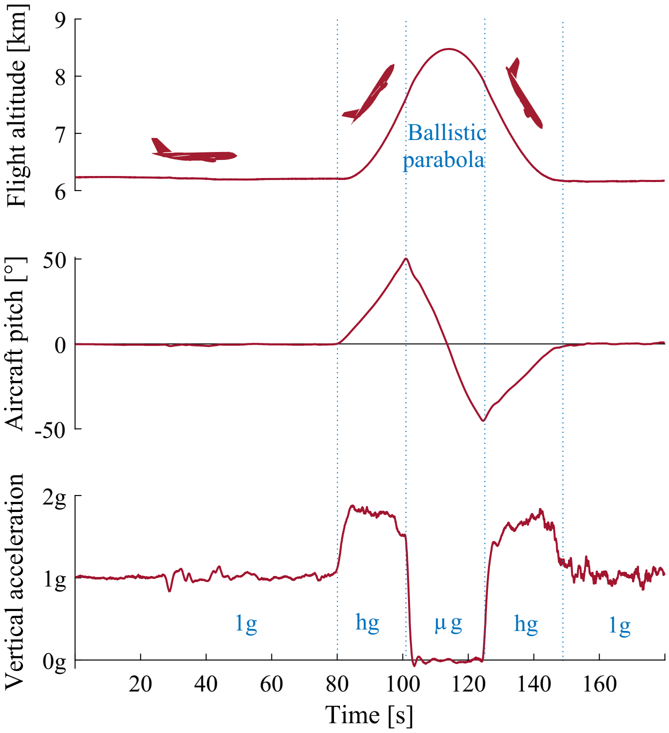

Figure 1.3: Typical measured flight altitude, aircraft pitch angle and perceived vertical acceleration (in units of $g = 9.81\ \mathrm{ms}^{-2}$) during a parabolic manoeuvre. The different indicated phases in the plots are normal gravity ($1g$), hyper-gravity (hg) and micro-gravity (μg).

1.4 Variable gravity aboard parabolic flights

Parabolic flights provide a possibility to carry out measurements in variable gravity. Variable gravity here denotes the gravity level perceived by the experiment and experimenters aboard the plane. Figure 1.3 illustrates a typical parabolic manoeuvre performed by the plane. A parabolic trajectory starts with a phase in which the objects inside the plane feel 'hyper-gravity' ($\approx 1.8\ g$ where $g = 9.81\ \mathrm{ms}^{-2}$ is the Earth's gravitational acceleration) lasting approximately 20 seconds, which is followed by 20 seconds of free-fall resulting in a perceived 'micro-gravity'. The parabolic trajectory ends with another phase of hyper-gravity. The vertical accelerational fluctuations in the micro-gravity phase remain small, with the maximum standard deviation being in the order of $0.02\ g$. The fluctuations of the horizontal accelerations also remain small ($< 0.03\ g$) throughout the parabola. The typical frequencies in the accelerational fluctuations range within 1–10 Hz, which are slow compared to the bubble oscillation period in our experiment.

The gravity-induced hydrostatic pressure gradient presents the advantage of being uniform in space and time, which is interesting because any practical instance of a pressure field in the liquid can be approximated to first order with such a uniform pressure gradient. Its correct modulation yields a highly controlled way of probing between highly spherical bubbles in micro-gravity to strongly deformed micro-jetting bubbles in hyper-gravity. Throughout this work are presented experiments carried out in parabolic flight campaigns operated by Novespace (Bordeaux, France) for the European Space Agency (ESA). One ESA campaign typically comprises three flights, in each of which a total of 31 parabolas are performed. Our experiment flew aboard an Airbus A300 ZERO-G in the 60th ESA campaign (2014), and aboard an Airbus A310 ZERO-G in its inaugural ESA (62^{nd}) campaign (2015). In addition, we participated in the first Swiss parabolic flight in Zurich (2015). To fulfill the new requirements imposed by the new A310 plane, the structures to host the experiment were re-built during this work. Additional details of the experimental setup and the parabolic flights may be found in refs. [97, 53].

1.5 Objective

The objective of this work is to develop predictive models for the most important quantities characterising micro-jets, shock waves, and luminescence of cavitation bubbles collapsing with varying levels of deformation. These models are strongly based on experimental observations searching for the full energy budget of a single bubble deformed by different sources, and supported by theoretical derivations and numerical simulations.

1.6 Thesis outline

This thesis is a compilation of three individual journal articles, each of which tackles one of the bubble's collapse phenomena. More specifically, *Scaling laws for jets of single cavitation bubbles* (chapter 2) is an analysis on micro-jets driven by different sources, and provides useful scaling laws for their key characteristics. *Shock waves from nonspherical cavitation bubbles* (chapter 3) presents experiments elucidating the complex shock wave emission associated with non-spherically collapsing bubbles, compares them for different sources of deformation, and proposes semi-empirical models for predicting their strengths. *Luminescence from cavitation bubbles deformed in uniform pressure gradients* (chapter 4) explores various properties of luminescence measured from the individual collapses of bubbles deformed by the hydrostatic pressure gradient, which is modulated via variable gravity. Finally, chapter 5 synthesises the main findings of the thesis, and discusses future prospectives.

2 Micro-jets

Scaling laws for jets of single cavitation bubbles

Reproduced version of

Outi Supponen, Danail Obreschkow, Marc Tinguely, Philippe Kobel, Nicolas Dorsaz and Mohamed Farhat. *Scaling laws for jets of single cavitation bubbles.* Journal of Fluid Mechanics **802**, pp. 263-293 (2016). DOI: 10.1017/jfm.2016.463,

with the permission of Cambridge University Press.[1]

The author's contribution:
The author performed the experiments and the analysis, and made a major contribution in the development of the scaling laws. She identified the regimes and helped to improve the numerical tool developed by Danail Obreschkow. She was the first author of this publication.

Abstract

Fast liquid jets, called micro-jets, are produced within cavitation bubbles experiencing an aspherical collapse. Here we review micro-jets of different origins, scales and appearances, and propose a unified framework to describe their dynamics by using an anisotropy parameter $\zeta \geq 0$, representing a dimensionless measure of the liquid momentum at the collapse point (Kelvin impulse). This parameter is rigorously defined for various jet drivers, including gravity and nearby boundaries. Combining theoretical considerations with hundreds of high-speed visualisations of bubbles collapsing near a rigid surface, near a free surface or in variable gravity, we classify the jets into three distinct regimes: weak, intermediate and strong. Weak jets ($\zeta < 10^{-3}$) hardly pierce the bubble, but remain within it throughout the collapse and rebound. Intermediate jets ($10^{-3} < \zeta < 0.1$) pierce the opposite bubble wall close to the last collapse phase and clearly emerge during the rebound. Strong jets ($\zeta > 0.1$) pierce the bubble early during the collapse. The dynamics of the jets is analysed through key observables, such as the jet impact time, jet speed, bubble displacement, bubble volume at jet impact and vapour-jet volume. We find that, upon normalising these observables to dimensionless

---

[1] Supplementary movies may be found at https://doi.org/10.1017/jfm.2016.463

jet parameters, they all reduce to straightforward functions of ζ, which we can reproduce numerically using potential flow theory. An interesting consequence of this result is that a measurement of a single observable, such as the bubble displacement, suffices to estimate any other parameter, such as the jet speed. Remarkably, the dimensionless parameters of intermediate and weak jets ($\zeta < 0.1$) depend only on ζ, not on the jet driver (i.e. gravity or boundaries). In the same regime, the jet parameters are found to be well approximated by power laws of ζ, which we explain through analytical arguments.

2.1 Introduction

Cavitation bubbles in liquids remain a central research topic due to their energetic properties, which can be damaging to, for example, hydraulic turbomachinery or ship propellers [109], or beneficial in applications such as microfluidics [29, 30] or medicine [110, 19]. In most cases, the damaging or beneficial effect comes from the shock and/or the micro-jet produced during the collapse of the cavitation bubbles, more specifically during the final collapse stage. In this paper, micro-jet always refers to the jet forming on the bubble wall and moving across the bubble interior, before piercing the wall on the opposite side. The dynamics of these micro-jets and their diverse origins constitute the framework of this review.

Decades of detailed research revealed a remarkable diversity of behaviours and effects of micro-jets, depending on the physical conditions (see reviews by Blake & Gibson [67] and Lauterborn & Kurz [44]). For instance, micro-jets can have diverse origins, including rigid or free surfaces near the bubble [67] or external force fields such as gravity [46] (section 2.2), and their evolution strongly depends on the properties of the liquid (section 2.4). To harvest the power of jets or suppress their damaging effects, we require an understanding of their physics across all possible conditions. In particular, we aim for a *general* description of the jet produced by a *single* cavitation bubble. Building such a general description requires both a unified theoretical model and systematic experimental studies across a wide range of parameters (e.g. bubble sizes, pressures, jet drivers).

Our objective is to describe the large variety of micro-jets and unify them in a single, theoretically supported framework. Contrary to previous works, we benefit from the luxury of increased computational power and cheaper high-speed imaging, enabling systematic numerical and experimental analyses of jetting bubbles in a large array of realistic conditions. Our experimental data not only cover a wide range of parameter space, but also contain some of the most spherical large cavitation bubbles and weakest jets studied to date. We combine these data with selected results from the literature, covering a large diversity of jets and bubble types. With the aim of comparing all these data, the results are suitably normalised to a set of dimensionless parameters characterising the jet physics. The statistics of these parameters are then compared against systematic theoretical predictions from customised numerical simulations. Finally, physical interpretations of the results are sought analytically.

The paper is structured as follows. Section 2.2 summarises the most prominent drivers of

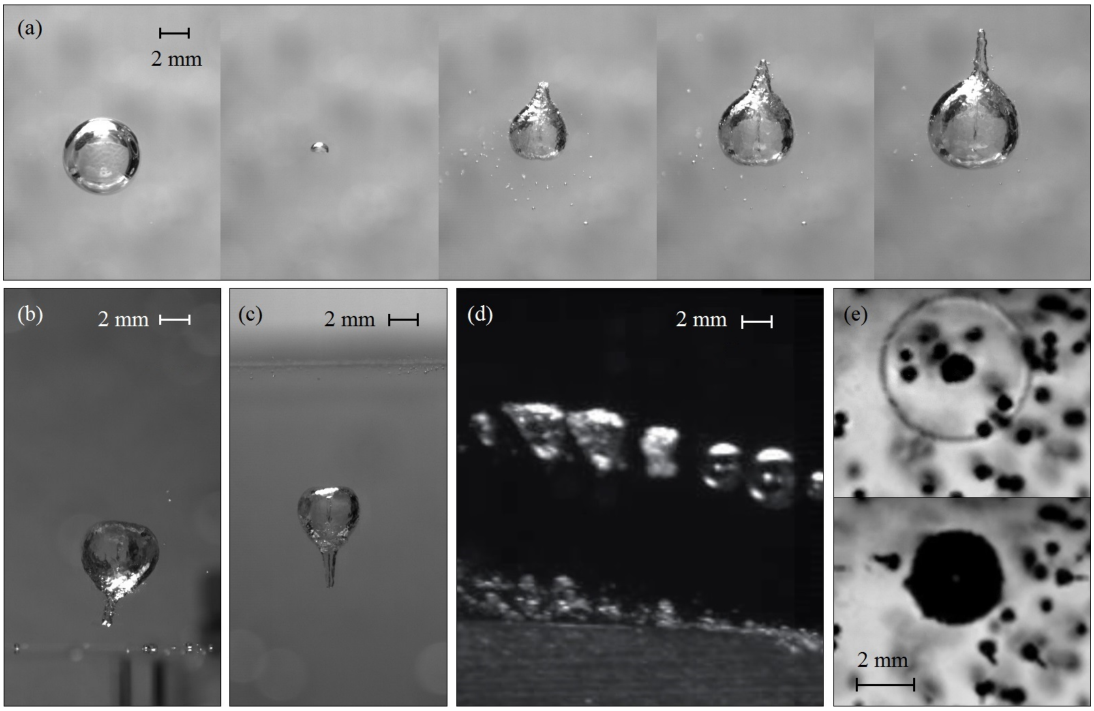

Figure 2.1: Micro-jets from different origins: a) Gravity, b) rigid surface, c) free surface, d) stationary flow (from [53]) and e) shock wave (see micro-bubbles). Images (a)-(d) correspond to equations (2.6) (a)-(d).

micro-jets and quantifies their 'strength' using a single parameter. Our experimental set-up for the systematic investigation of jets in various conditions is described in section 2.3. We then systematically study the variation of the micro-jet dynamics as a function of the pressure field anisotropy. First, we phenomenologically classify the jets into three visually distinct regimes in section 2.4. Section 2.5 follows up with a quantitative analysis of five dimensionless jet parameters, studied as a function of a suitable anisotropy parameter and compared against numerical simulations. Section 2.6 synthesises all the experimental and numerical results in a single figure, presents physical interpretations of the results and discusses potential applications and limitations.

2.2 The diverse origins of micro-jets

Micro-jets are produced during the aspherical collapse of cavitation bubbles. The sphericity of bubbles is broken by anisotropies in the surrounding pressure field. There are various possible origins for such anisotropies (see figure 2.1), with the most common ones being discussed hereafter.

Most micro-jet investigations have focused on bubbles collapsing near a rigid or a free surface (figures 2.1b and 2.1c). The level of bubble asphericity is generally quantified by a dimensionless stand-off parameter $\gamma = h/R_0$, where h is the distance from the initial bubble centre to the surface and R_0 is the maximum bubble radius. The usual findings are that γ governs much of the micro-jet dynamics, such as its speed or erosive force [111, 112, 113]. Most experimental studies are limited to $\gamma < 5$, as beyond this limit, the bubble undergoes a nearly spherical collapse that often appears indistinguishable from a boundary-free collapse, given the limited initial sphericity of the bubble. In highly symmetric experimental conditions (relying on mirror-focused lasers and/or microgravity conditions), it is nonetheless possible to detect jets beyond $\gamma = 10$, as we shall demonstrate in sections 2.4 and 2.5.

Another typical micro-jet driver, not accounted for by the stand-off parameter γ, is the gravity-induced hydrostatic pressure gradient, i.e. buoyancy [46] (figure 2.1a). Gravity becomes particularly apparent when dealing with larger bubbles and/or hypergravity environments, such as in the studies in refs. [45], [114] and [68]. To quantify the effect of buoyancy, Gibson introduced the dimensionless parameter $\sigma = \rho g R_0/\Delta p$, where ρ is the liquid density, g is the gravitational acceleration and $\Delta p \equiv p_0 - p_v$ is the driving pressure (p_0 is the pressure at infinity at the vertical position of the bubble centre and p_v is the vapour pressure). A similar parameter, $\delta = \sigma^{1/2}$, has also been used in the past to account for the effect of gravity [68, 98].

Further origins of cavitation bubble micro-jets are, for example, flows with pressure gradients [53, 69] (figure 2.1d), shock waves [115, 116] (figure 2.1e), focused ultrasound [117] or neighbouring bubbles [118]. Also, a combination of different jet drivers together can cause the bubble asphericity, enhancing the jet formation, or even suppressing it. An example of such a combination is seen in figure 2.1d where a bubble in a stationary flow collapses near a rigid hydrofoil. Its micro-jet, however, is not shot towards the nearest surface but, instead, directed more against the pressure gradient of the flow.

The plethora of micro-jet drivers and the fact that different drivers can act simultaneously highlight the need for a unified framework, approximately describing the jet dynamics for a multitude of jet drivers. To this end, we need to quantify the jet-driving pressure field anisotropy with a parameter defined for various origins of this anisotropy and applicable to bubbles of many sizes and external conditions. In general, any smooth pressure field can be expanded in the space coordinates as

$$p(\mathbf{x}, t_0) = p(\mathbf{x}_0, t_0) + (\mathbf{x}-\mathbf{x}_0)^\top \nabla p + \frac{1}{2}(\mathbf{x}-\mathbf{x}_0)^\top \mathbf{D}(p)\,(\mathbf{x}-\mathbf{x}_0) + O(\mathbf{x}^3), \tag{2.1}$$

where ∇p and $\mathbf{D}(p)$, respectively, denote the gradient and Hessian matrix of the pressure field at $\mathbf{x} = \mathbf{x}_0$ and $t = t_0$, here considered to be the bubble centroid and time at the instant of the bubble generation. To first order, the effects of pressure field anisotropies therefore depend on the constant ∇p.

To define a dimensionless anisotropy parameter, we can exploit the fact that the inviscid Navier-Stokes equations without surface tension are self-similar, such that they become dimensionless by normalising length scales by R_0, pressures by Δp and velocities by $(\Delta p/\rho)^{1/2}$.

The assumption for the minor role of surface tension and viscosity is widely accepted for the first bubble oscillation in water for bubbles bigger than $R_0 \sim 10^{-5}$ m (see e.g. [119]). Applying this normalisation to ∇p leads to the dimensionless vector parameter [46]

$$\boldsymbol{\zeta} \equiv -\nabla p R_0 \Delta p^{-1}, \tag{2.2}$$

where the minus sign ensures that the jet driven by ∇p is directed along $\boldsymbol{\zeta}$. A straightforward calculation (Appendix 2.8.1) shows that $\boldsymbol{\zeta}$ is a dimensionless version of the so-called Kelvin impulse [45, 68, 69] **I**, defined as the linear momentum acquired by the liquid during the asymmetric growth and collapse of the bubble,

$$\mathbf{I} = 4.789 R_0^3 \sqrt{\Delta p \rho}\, \boldsymbol{\zeta}. \tag{2.3}$$

The value 4.789 is strictly an irrational number, the exact value of which is given in equation (2.21) in the Appendix. The term $R_0^3\sqrt{\Delta p \rho}$ has the units of momentum, as expected.

In situations where the micro-jet cannot be attributed to an external ∇p, we can define $\boldsymbol{\zeta}$ such that equation (2.3) still returns the correct Kelvin impulse. For instance, if the jet is caused by a rigid or free surface at a stand-off parameter γ, the Kelvin impulse is given by (Appendix 2.8.1)

$$\mathbf{I}_{\mathbf{surface}} = 0.934 R_0^3 \sqrt{\Delta p \rho}\, \gamma^{-2} \mathbf{n} \cdot \begin{cases} -1 & \text{flat rigid surface} \\ +1 & \text{flat free surface} \end{cases}, \tag{2.4}$$

where **n** is the normal unit vector on the surface pointing to the cavity centre. The exact value of 0.934 is given in equation (2.25). Equating (2.3) and (2.4) yields

$$\zeta = 0.195 \gamma^{-2}. \tag{2.5}$$

with the exact expression of 0.195 given in equation (2.26). When expressing ζ as a function of γ in this way, equation (2.3) yields the correct Kelvin impulse for a rigid/free surface. An analogous approach can be used to derive $\boldsymbol{\zeta}$ for other types of boundaries [120, 69] and pressure gradients,

$$\boldsymbol{\zeta} = \begin{cases} -\rho \mathbf{g} R_0 \Delta p^{-1} & \text{gravitational field} & \text{(a)} \\ -0.195\gamma^{-2}\mathbf{n} & \text{flat rigid surface} & \text{(b)} \\ +0.195\gamma^{-2}\mathbf{n} & \text{flat free surface} & \text{(c)} \\ -\rho(\mathbf{u}\cdot\nabla)\mathbf{u} R_0 \Delta p^{-1} & \text{stationary potential flow} & \text{(d)} \\ 0.195\gamma^{-2}(\rho_1-\rho_2)(\rho_1+\rho_2)^{-1}\mathbf{n} & \text{liquid interface} & \text{(e)} \\ 0.195\gamma^{-2}(4\alpha - 1 - 8\alpha^2 e^{2\alpha} E_1(2\alpha))\mathbf{n} & \text{inertial boundary} & \text{(f)} \end{cases} \tag{2.6}$$

Here **u** is the velocity field, ρ_1 and ρ_2 are the different densities of the two liquids, α is defined as $\alpha \equiv \rho h/\Sigma$ (where ρ is the liquid density, h is the distance from the initial bubble centre to the surface and Σ is the surface density) [121] and $E_1(x) \equiv \int_x^\infty t^{-1}e^{-t}\mathrm{d}t$ is an exponential integral. In the linear expansion of the pressure field, the anisotropy parameter associated with a combination of drivers (e.g. gravity and flat surface) is given by the vector sum of the respective $\boldsymbol{\zeta}$. Defining a corresponding anisotropy parameter for more complicated jet drivers, such as neighbouring bubbles, shock waves or ultrasound that are strongly time-dependent, or boundaries with complex geometries, is not as straightforward as for the above examples. In the present work, we focus on unifying the jet drivers listed in equations (2.6), and restrict experimental verification to gravity, flat rigid and free surfaces.

We expect, and will show in the following, that the jet becomes more pronounced (in a sense specified in section 2.5) with increasing $\zeta \equiv |\boldsymbol{\zeta}|$. Importantly ζ, unlike the Kelvin impulse, has the special property that bubbles with equal values of ζ produce *similar* (i.e. identical in normalised coordinates) jets irrespective of the jet driver (e.g. gravity, rigid/free surface). This prediction naturally breaks down as the higher-order terms in equation (2.1) become significant. As we shall see (section 2.5), this is the case, for example, for strongly deformed bubbles (i.e. $\zeta > 0.1$, corresponding to $\gamma < 1.4$ following (2.5)). Following the same argument, other types of micro-jets, not treated in this work, are only well described by ζ if the time-constant gradient in the expansion of the pressure field dominates the jet formation.

2.3 Experimental set-up

Our experimental set-up - details of which are given in [97] - generates highly spherical bubbles by focusing a green pulsed laser (532 nm, 8 ns) inside a large cubic test chamber (18 cm×18 cm×18 cm) filled with degassed water. The laser beam is first expanded to a diameter of 5 cm using a lens system, and then focused onto a single point using a parabolic mirror with a high convergence angle (53°) to generate a point-like initial plasma. In this way, we obtain a bubble of very high initial sphericity, which is impossible to achieve with a pure lens system that is affected by refractive-index variations, spherical aberration and/or the proximity of the lens to the bubble. As a result, we are able to cover a large range of anisotropies ζ, including the delicate 'weak jet' regime previously unexplored, where the jets are barely observable (see section 2.4.1). We observe the micro-jets through high-speed visualisations with the Photron SA1.1 and Shimadzu HPV-X camera systems, reaching speeds up to 10 million frames per second. The bubbles are illuminated using a flashlamp (bubble interface and interior) or a parallel backlight light-emitting diode (shadowgraphy and shock waves).

Three parameters can be independently varied in our experiment: (i) the driving pressure Δp ($\sim$ 0.1-1 bar), (ii) the bubble energy $E_b = (4\pi/3)R_0^3\Delta p$ (1–12 mJ) and (iii) the gravity-induced pressure gradient ∇p, modulated aboard ESA parabolic flights (56th, 60th and 62nd parabolic flight campaigns). In addition, a free or a rigid surface may be introduced near the bubble at a controlled distance. The maximum bubble radii R_0 vary within the range 1.5–8.0 mm and the Rayleigh collapse times ($T_c = 0.915R_0(\rho/\Delta p)^{1/2}$) within the range 0.1–3 ms. The parameter space covered by the experiment is displayed in figure 2.2. A subsample of these data points is used in the following analyses.

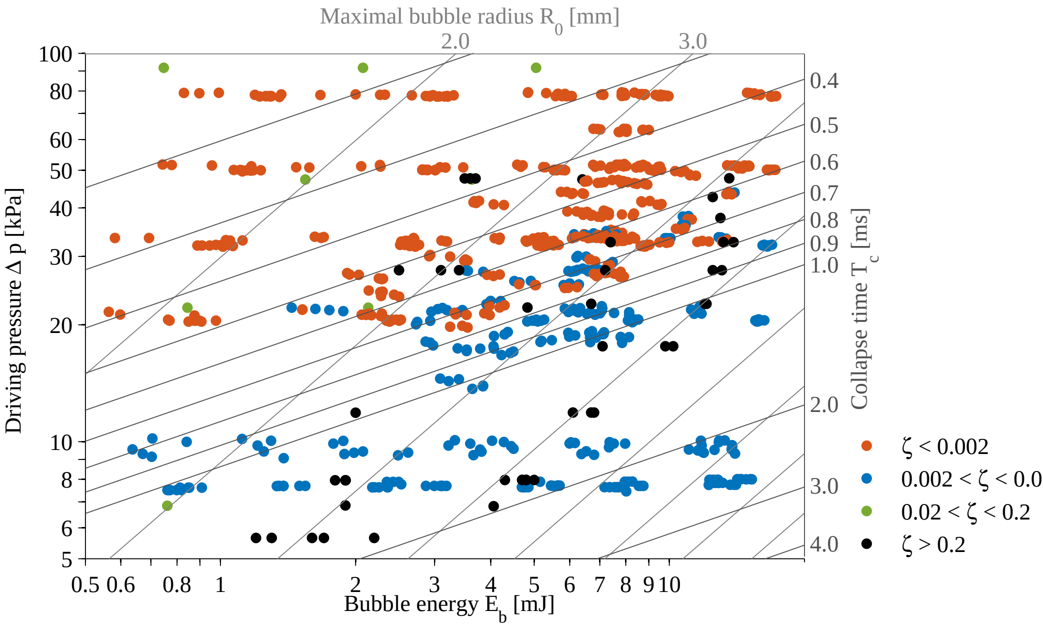

Figure 2.2: Overview of the parameter space covered by the experiment. The data points include bubbles subject to gravity and a nearby rigid/free surface. The four parameters E_b, Δp, R_0 and T_c are related via the two relations $E_b = (4\pi/3)R_0^3\Delta p$ and $T_c = 0.915R_0(\rho/\Delta p)^{1/2}$ (spherical collapse) and can therefore be reduced to any combination of just two parameters, representable in a two-dimensional plot.

2.4 Qualitative classification of jetting regimes

The micro-jet dynamics strongly varies with the anisotropy in the pressure field, that is with the anisotropy parameter ζ defined in eq. (2.6). This section introduces a phenomenological classification of the micro-jet dynamics into three separate regimes, ‘weak’, ‘intermediate’ and ‘strong’, identified with three distinct ranges of ζ. An example of a micro-jet in each regime is given in figure 2.3: weak (figure 2.3a) and intermediate (figure 2.3b) jets form so close to the collapse point that they are primarily visible during the rebound. Whereas intermediate jets push through the wall of the rebound bubble and drag along a conical vapour pocket (‘vapour-jet’), weak jets hardly pierce the rebound bubble and remain almost entirely inside it. In turn, strong jets (figure 2.3c) pierce the bubble well before the first collapse, leaving behind thick vortex rings.

The transition between weak and intermediate jets occurs around $\zeta = 10^{-3}$, whereas the division between intermediate and strong jets lies around $\zeta = 0.1$. These transitions are not sharp, since the jet dynamics changes continuously with ζ. The separation between weak, intermediate and strong jets nonetheless presents a useful thinking tool to establish a unified perspective on these visually distinct types of micro-jets. Each regime is discussed and visualised in detail in the following sections.

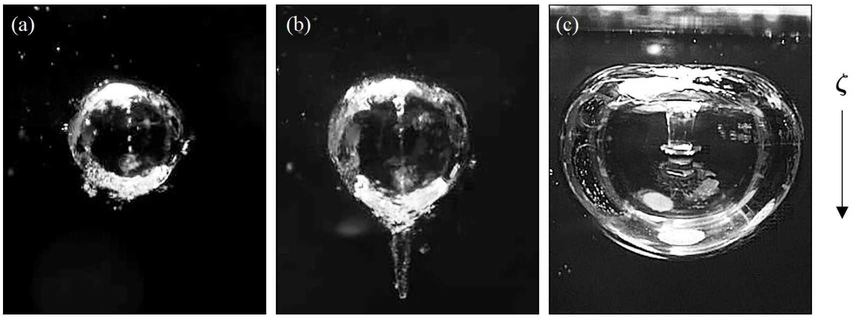

Figure 2.3: Observations of three distinct micro-jet types driven by a nearby free surface: (a) weak jet ($\zeta \lesssim 0.001$) seen only inside the rebound bubble following the collapse, (b) intermediate jet ($\zeta = 0.01$) emerging during the rebound and (c) strong jet ($\zeta = 0.64$, from [122]) seen early during the collapse. The arrow on the right shows the direction of the anisotropy parameter $\boldsymbol{\zeta}$.

2.4.1 Weak jets ($\zeta \leq 10^{-3}$)

Weak jets are the most delicate type of micro-jets. They are only seen during the rebound phase succeeding the first bubble collapse, and even then they remain entirely, or almost entirely, contained *inside* the rebound bubble. Therefore, weak jets can only be revealed using sophisticated visualisations of the bubble interior.

The reason why weak jets merit a regime of their own, despite their hidden existence, is the sensitivity of the collapse physics on even tiny pressure field anisotropies. For instance, the luminescence energy of bubbles near boundaries has been shown to vary with the stand-off parameter γ up to $\gamma \approx 20$ [123] ($\zeta \approx 5 \cdot 10^{-4}$). We find this to be the case for even lower values of ζ (discussed in a forthcoming publication).

Experimentally, an extremely high initial bubble sphericity is required for a weak jet to form. Based on numerical models used to design the experimental set-up (section 2.3), we estimate that the amplitude of the deformation of the initial bubble relative to its maximal radius should be less than 10^{-4}. Bubbles generated by discharge sparks (e.g. [114]) and lens-focused laser pulses (e.g. [112]) are generally not spherical enough to probe the regime $\zeta < 10^{-2}$ (see chapter 4 in [53]). Within the accuracy of such standard experiments, $\gamma > 4$ (or $\zeta < 0.012$) appears to produce a spherical collapse, where, in fact, the jet has been masked by perturbations that are more important than the jet itself. The hidden weak jet is also challenging to visualise due to its microscopic size, its unstable nature within the rebound and a non-transparency of the bubble interface at the early rebound stages.

Our experiment (section 2.3) is suitable for studying weak jets by virtue of its mirror-focused laser and the option to reduce gravity on parabolic flights. An example of a weak jet produced by a distant free surface ($\gamma \approx 14$) is shown in figure 2.3a. An alternative example of a gravity-driven weak jet is shown in figure 2.4. The bubble remains highly spherical throughout

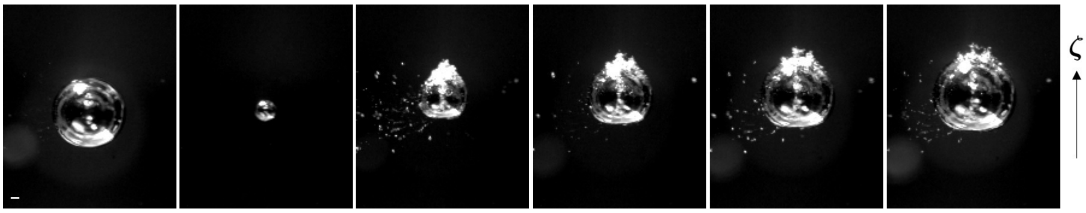

Figure 2.4: Weak jet formation driven by gravity. The interframe time is 90 μs. The white bar shows the 1 mm scale. The anisotropy parameter ζ equals 0.001. The arrow on the right shows the direction of $\boldsymbol{\zeta}$. See *Movie1.mp4*.

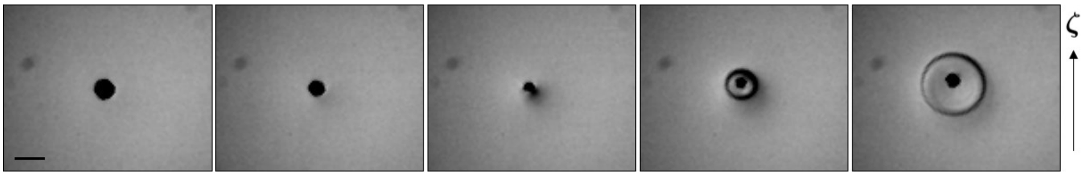

Figure 2.5: Shock wave emission at the collapse of a bubble with a gravity-driven weak jet. The interframe time is 300 ns. The exposure time is only 60 ns, leading to a sharp shock front. The black bar shows the 1 mm scale. The anisotropy parameter ζ equals 0.001. The arrow on the right shows the direction of $\boldsymbol{\zeta}$. See *Movie2.mp4*.

the collapse (frames 1–2) and rebound (frames 3–6). However, one can observe a jet inside the rebound bubble (frames 3–4). During the growth of the rebound bubble, the micro-jet becomes unstable and 'pulverises' into a chain of microscopic droplets. (The phenomenon is more readily observable in the linked supplementary movie.)

Bubbles with weak jets emit a single shock at their collapse, as shown in figure 2.5. The only way to tell that the bubble is subject to a deformation during its collapse is its translation, which is an expression of the momentum (Kelvin impulse) accumulated during the growth and collapse. The bubble has moved most significantly at its minimal radius between frames 3 and 4 in figure 2.5, as evidenced by the different centres of the bubble and the shock in frame 4.

By systematically varying ζ while taking visualisations similar to figure 2.4, we found $\zeta \leq 10^{-3}$ (corresponding to $\gamma \gtrsim 14$ for bubbles near a rigid or free surface) to be the anisotropy range of weak jets. Larger values of ζ produce jets that visibly emerge from the rebound bubble (see section 2.4.2). The limit is not a hard one, but nonetheless gives a fair indication on the pressure field anisotropy where a significant reduction in the vapour-jet size outside the rebound bubble is observed.

The observed instability of weak jets, as well as the fact that these jets live entirely inside the bubble gas (a medium of rapidly changing temperature and pressure), hint at complex physical mechanisms, beyond the scope of this work. A subtle question is whether a weak

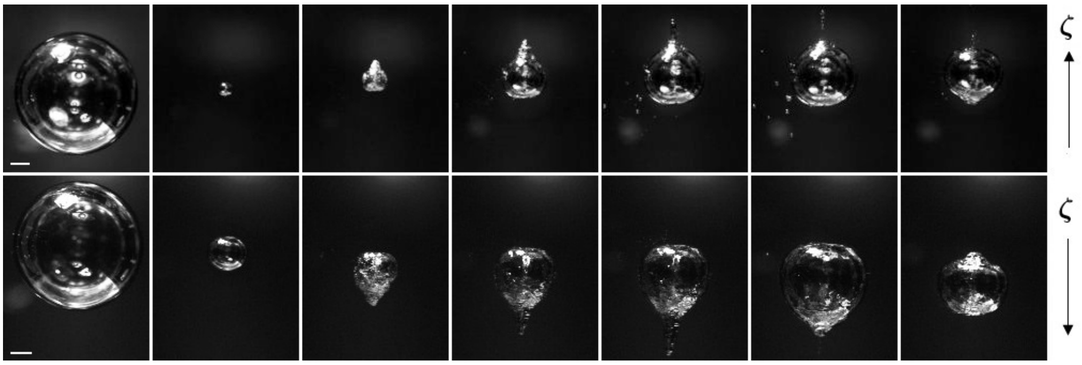

Figure 2.6: Selected images of bubbles with intermediate jets driven by gravity (upper) and a nearby free surface (lower). Images have been taken at times $t = 0.9$, 2.15, 2.25, 2.35, 2.45, 2.85 and 3.35 ms (upper) and $t = 2.05$, 4.15, 4.2, 4.35, 4.6, 4.75 and 6.2 ms (lower) from bubble generation. (The different evolution speeds are simply due to different liquid pressures chosen for the two experiments.) The white bar shows the 1 mm scale. The anisotropy parameter ζ equals 0.007, equivalent to a stand-off parameter γ of 5.3. The arrows on the right show the direction of $\boldsymbol{\zeta}$. See *Movie3.mp4* and *Movie4.mp4.*

jet slightly pierces the bubble at the collapse point. Potential flow theory of an empty bubble predicts that the jet always pierces the bubble [67] no matter how small the Kelvin impulse (> 0). However, our visualisations do not show clear evidence for such piercing – at least the jet does not entrain a vapour-jet. Perhaps weak jets are so small and low in kinetic energy that they are stopped by surface tension or heavily affected by the hot plasma at the last collapse stage. Detailed modelling, ideally using molecular dynamics simulations, is needed to uncover these details.

2.4.2 Intermediate jets ($10^{-3} < \zeta < 0.1$)

In the intermediate jet regime ($10^{-3} < \zeta < 0.1$), the jet pierces the bubble close to the moment of collapse and entrains a conical vapour-jet during the rebound phase.

Figure 2.6 shows an intermediate jet produced by gravity (upper) and by a nearby free surface (lower). The jet is visible inside the rebound bubble and as a conical protrusion of vapour dragged along while the jet is penetrating the liquid. The rebound bubble has a transparent interface and eventually regains a shape close to spherical. It is worth emphasising that, despite the different jet drivers in figure 2.6, the two bubbles exhibit nearly identical shapes apart from the opposite jet directions. This confirms our expectation (section 2.2) that identical values of ζ lead to similar jets, independently of the jet driver.

One can note a similar pulverisation of the jet inside the rebound bubble as observed in the case of the weak jets (more readily visible in the linked supplementary movie). Furthermore, the issue of initial bubble sphericity discussed in section 2.4.1 plays an important role in the intermediate regime as well. Micro-jet studies in the literature seldom observe jets at $\gamma > 4$,

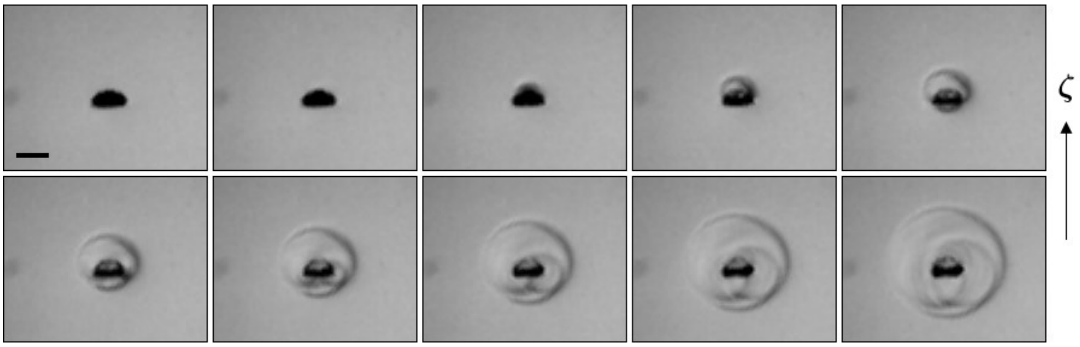

Figure 2.7: Shock wave emission at the collapse of a bubble with a gravity-driven intermediate jet. The interframe time is 100 ns, the exposure time is 60 ns. The black bar shows the 1 mm scale. The anisotropy parameter ζ equals 0.007. The arrow on the right shows the direction of $\boldsymbol{\zeta}$. See *Movie5.mp4*.

while we observe both gravity- and boundary-induced jets all the way down to the weak jet regime at $\zeta < 10^{-3}$, corresponding to $\gamma > 14$.

There is a peculiarity that we observe in the intermediate regime: the formation of a bump on the rebound bubble, at the location where the micro-jet initially develops (i.e. opposite from where the jet pierces the bubble). This bump can be seen in the last frames of figure 2.6. Vogel *et al.*[111] explained this phenomenon as a wake of a vortex ring inside the bubble, induced by the ring vortex in the liquid surrounding the rebounding bubble. However, our visualisations suggest that it is the pinch-off and the break-up of the jet within the rebound bubble that cause this deformation. Owing to surface tension, the remainder of the jet is pulled back and seen as a bulge on the interface. This part of the interface struggles to follow the rest of the bubble during the second collapse, making the deformation even more pronounced (see linked supplementary movies in figure 2.6). Such a deformation is predominantly seen in bubbles collapsing in the intermediate regime, although it is also marginally observed in bubbles with weak jets.

In the intermediate regime, the piercing of the bubble occurs so late in its lifetime that extreme temporal and spatial resolutions are needed to capture the jet before the collapse point. Interestingly, shock-wave visualisations can be exploited to increase the time resolution much beyond the frame rate by virtue of the high shock velocities. The multiple shock waves in figure 2.7, in particular the different radii of these shocks, clearly reveal that the jet pierces the bubble before the collapse of the torus, even though this is hard to see by looking at the bubble itself. An interesting feature that many micro-jet studies have come across in the intermediate jet regime (and partly in the strong jet regime) is a ‘counter-jet’ that appears immediately after the bubble collapse and moves in the opposite direction to the original micro-jet. Such a counter-jet has been reported to appear for bubbles collapsing near rigid surfaces at $1 < \gamma < 3$ [47] and to consist of a cluster of tiny bubbles. The formation of the counter-jet is attributed to the jet impact on the opposite bubble wall. However, the phenomenon has also been seen

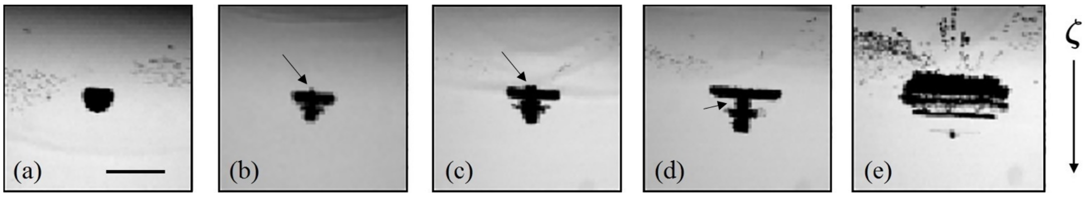

Figure 2.8: Selected images right after the collapse of bubbles near a free surface with (a) $\gamma = 2.1$, (b) $\gamma = 1.6$, (c) $\gamma = 1.3$, (d) $\gamma = 1.0$ and (e) $\gamma = 0.86$. Counter-jet formation is visible in (b), (c) and (d), indicated with arrows. The black bar shows the 1 mm scale. The arrow on the right shows the direction of $\boldsymbol{\zeta}$.

in bubbles with gravity-driven jets at $\zeta \approx 0.2$ (see figure 2 in ref. [98]). Furthermore, in our experiment we observe such counter-jets for bubbles collapsing near a free surface, as seen in figure 2.8 – visible in figure 2.8(b,c), and also in figure 2.8(d), although here the counter-jet does not appear above the torus but rather appears as a 'column' on the central axis of the torus. The phenomenon is therefore linked not to the presence of rigid boundaries but to the pressure field anisotropy of the aspherical collapse. The formation of the counter-jet has been suggested to be a result of the self-penetration of the 'jet torus shock waves', i.e. the shock waves emitted at the collapse of the main torus, which create a region of tension perpendicular to the torus ring at their confluence [47].

2.4.3 Strong jets ($\zeta > 0.1$)

The strong jet regime ($\zeta > 0.1$) is characterised by the jet piercing the bubble well before (more than 1%: cf. section 2.5.2) the collapse. Not only have strong jets mostly been observed near a rigid or a free surface [112, 124], but also gravity has been shown to produce jets in this regime [98].

The strong jet regime is peculiar in the sense that the complex collapse dynamics involved is highly sensitive to the origin of the pressure field anisotropy. For instance, there is a large variety in the shapes that the jet can take prior to piercing the bubble, from large and broad (such as in figure 3 in [98]) to thin, mushroom-capped jets [122] typically linked to a nearby free surface (such as in figure 2.9).

The collapse of a strongly jetting bubble follows a sequence of highly complex dynamics. Figure 2.9[2] shows an example of such a bubble collapsing near a free surface ($\zeta = 0.62$, i.e. $\gamma = 0.56$), the micro-jet being particularly thin compared to the bubble size. The interface of the bubble becomes opaque already prior to the collapse (frames 3-4) due to perturbations caused by the jet impact on the opposite side of the bubble [122]. Following the jet impact, the bubble breaks into two parts as a vapour pocket is entrained by the jet. Each part has its

---

[2] Reproduced from: O. Supponen, P. Kobel, D. Obreschkow and M. Farhat. *The inner world of a collapsing bubble.* Physics of Fluids **27**(9), 091113 (2015), with the permission of AIP Publishing.

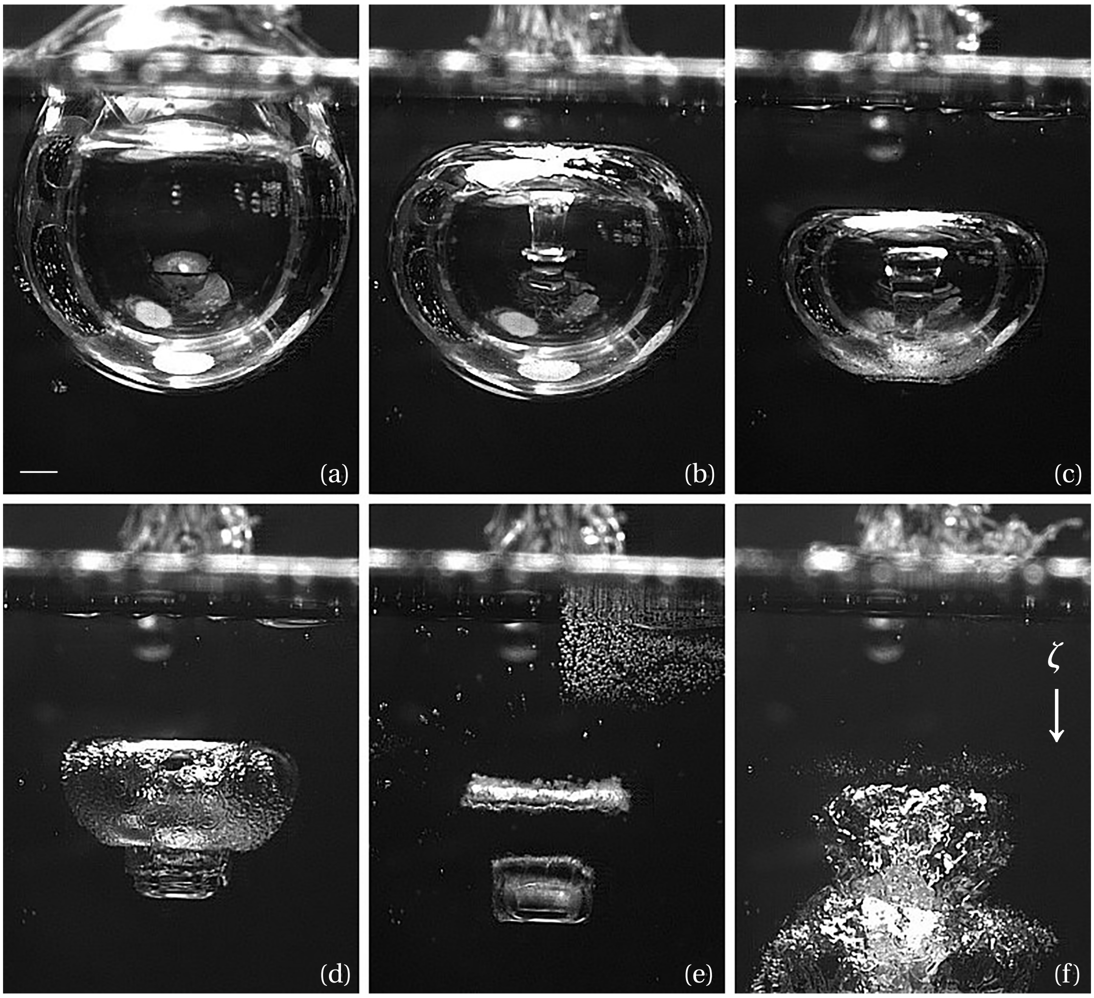

Figure 2.9: Selected images of a bubble with a strong jet driven by a nearby free surface (from [122]). The anisotropy parameter ζ equals 0.62, equivalent to a stand-off parameter $\gamma = 0.56$. The different instants are (a) $T = 0$ ms, (b) $T = 0.5$ ms, (c) $T = 0.9$ ms, (d) $T = 1.2$ ms, (e) $T = 1.4$ ms and (f) $T = 2.2$ ms. The white bar shows the 1 mm scale. The arrow on the right shows the direction of $\boldsymbol{\zeta}$. Video: APS-DFD (dx.doi.org/10.1103/APS.DFD.2014.GFM.V0084)

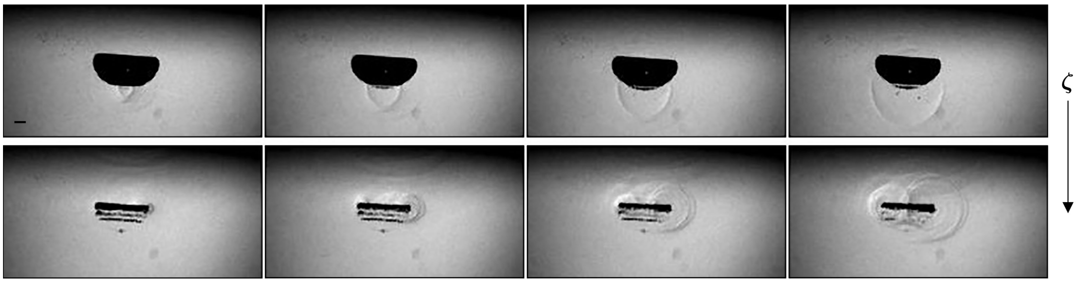

Figure 2.10: Shock wave emission at the collapse of a bubble with a free surface-driven strong jet, with the jet impact (upper) and toroidal collapse (lower) (from [122]). The interframe time is 300 ns, the exposure time is 60 ns. The black bar shows the 1 mm scale. The anisotropy parameter ζ equals 0.22, equivalent to a stand-off parameter $\gamma = 0.95$. The arrow on the right shows the direction of $\boldsymbol{\zeta}$. Video: APS-DFD (dx.doi.org/10.1103/APS.DFD.2014.GFM.V0084)

individual collapse. The rebounding bubble emerges as a chaotic bubble cloud (frame 6).

Figure 2.10 displays a shock-wave visualisation of another strongly jetting bubble collapsing near a free surface (at lower ζ). A first shock wave is emitted at the jet impact on the bubble wall (upper row), and a complex pattern of shock waves is generated as the bubble breaks down into different tori that each collapse individually [125, 122].

Important variations for different jet drivers (gravity versus rigid/free surfaces) are expected at these high pressure field anisotropies, as a direct consequence of the higher-order terms in eq. (2.1). These higher-order terms and their time dependence ensure that a bubble next to a rigid boundary ($\gamma < 1$) cannot cross that boundary and that a bubble next to a free surface ($\gamma < 0.5$) will burst that surface, while bubbles with a comparable Kelvin impulse generated by gravity simply travel large distances ($> R_0$; see section 2.5).

2.5 Quantitative analysis of jet dynamics

We now present different quantitative parameters describing micro-jets across all three jetting regimes of section 2.4. We complement our experimental results with selected data from the literature for the following jet types: gravity-induced, free surface-induced and rigid surface-induced micro-jets, as well as combinations thereof. These data also cover a large diversity of bubble types, including bubbles generated by pulsed lasers (with lens and mirror focus), sparks, underwater explosions and focused ultrasound.

The experimental data are compared against theoretical models based on potential flow theory. We start the section by presenting these numerical models, and subsequently discuss how the normalised jet impact timing, the jet speed, the bubble centroid displacement, the bubble volume at jet impact and the vapour-jet volume vary with the pressure field anisotropy, quantified by ζ.

2.5.1 Numerical simulation

We calculate the evolution of the bubble and the formation of the micro-jet in the standard model of an inviscid, incompressible fluid without surface tension. The bubble is assumed to contain fully condensable gas of constant pressure p_v. The pressure infinitely far away from the bubble, at the vertical level of the bubble centroid, is p_0. The evolution of this bubble is governed by the simplified Navier-Stokes equations

$$\begin{aligned} \frac{\mathrm{D}\mathbf{u}}{\mathrm{D}t} &= -\nabla p/\rho + \mathbf{g}, && (2.7) \\ \nabla\cdot\mathbf{u} &= 0, && (2.8) \end{aligned}$$

where $D\mathbf{u}/\mathrm{D}t \equiv \partial\mathbf{u}/\partial t + (\mathbf{u}\cdot\nabla)\mathbf{u}$ is the material derivative, i.e. the time derivative seen by a particle moving with the flow. Equations (2.7) and (2.8) represent the conservations of momentum and mass, respectively. These equations must be completed with suitable initial and boundary conditions that depend on the jet driver – e.g. rigid surface [70], free surface or gravity [71].

A straightforward, but numerically delicate, method for solving these equations is the 'pressure formulation', where eq. (2.8) is rewritten as a condition on the time-dependent pressure field p needed to evaluate ∇p in eq. (2.7). A more powerful and precise method, strongly advocated by Blake and collaborators [70, 71, 67], is the boundary integral method. This method relies on the flow being irrotational, $\nabla\times\mathbf{u} = 0$, such that the velocity field $\mathbf{u}$ derives from a potential ϕ, via $\mathbf{u} = \nabla\phi$. Green's integral formula [67] applied to eq. (2.8) then leads to

$$\phi(\mathbf{r}) = \frac{1}{2\pi}\left[\int_{\mathbf{r}'\in S}\mathrm{d}S\frac{\partial\phi(\mathbf{r}')}{\partial n}\frac{1}{|\mathbf{r}-\mathbf{r}'|} - \int_{\mathbf{r}'\in S}\mathrm{d}S\,\phi(\mathbf{r}')\frac{\partial}{\partial n}\left(\frac{1}{|\mathbf{r}-\mathbf{r}'|}\right)\right], \tag{2.9}$$

where S denotes the surface of the bubble and, if present, the free surface of the liquid, and $\partial/\partial n$ denotes the normal derivative on that surface away from the liquid.

The time evolution of the potential is given by Bernoulli's principle, which derives from eq. (2.7) [71, 70],

$$\frac{\mathrm{D}\phi}{\mathrm{D}t} = \frac{|\mathbf{u}|^2}{2} - gz + P \tag{2.10}$$

where z denotes the direction against the gravity vector $\mathbf{g}$, g is the norm of $\mathbf{g}$, and the pressure term is given by $P = \Delta p/\rho = (p_v - p_0)/\rho$ on the bubble surface and $P = 0$ on the free surface.

We discretise and numerically solve (2.9) and (2.10) using the scheme presented in [70]. This method discretises the boundary into linear elements in which case (2.9) can be rewritten as a linear system of equations. It should be noted that the model only computes the bubble evolution up to the moment of jet impact, i.e. when the bubble becomes toroidal.

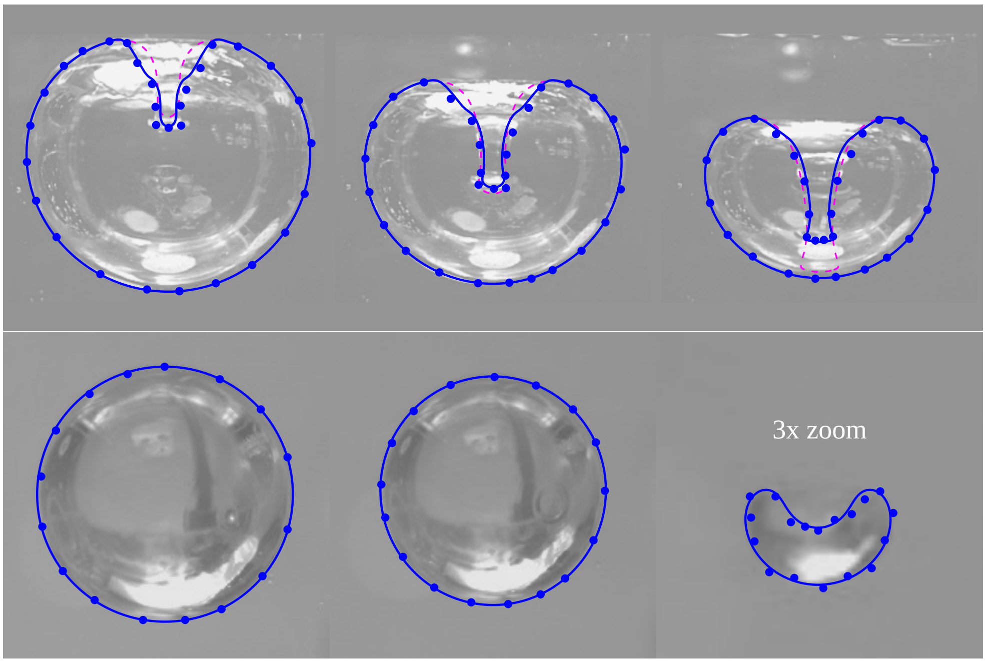

Figure 2.11: The numerical simulations superimposed with the experimental visualisations for a bubble collapsing near a free surface $\gamma = 0.56$ (top) and near a rigid surface $\gamma = 2.32$ (bottom). The blue points are extracted from the observed bubble shapes and the lines represent simulated data. In the case of the upper panel, the simulated bubble shape (dashed purple line) was corrected for optical refraction (solid blue line) by the outer bubble boundary, assuming a refraction by a sphere with equations analogous to those in [126] (with water and vacuum inverted).

A crucial feature of the model specified by equations (2.9) and (2.10) is that, upon normalising distances to the maximal bubble radius R_0 and normalising the time to $R_0(\rho/\Delta p)^{1/2}$, the evolution of the bubble exclusively depends on the anisotropy parameter ζ given in equation (2.6) and on the origin of ζ (e.g. gravity or nearby surfaces) via the boundary conditions. Moreover, since ζ is defined such that to first order the pressure field anisotropy does *not* depend on the origin, we expect the micro-jet to depend on the origin only for large values of ζ.

The bubble shapes calculated through the numerical simulation are superimposed on the corresponding experimental images in figure 2.11 with two distinct jet drivers. The simulated and observed shapes are in good agreement, justifying the use of the boundary integral method for the analysis of the individual micro-jet parameters. Interestingly, even the ‘mushroom cap’-shaped jet tip is reproduced for the bubble collapsing near a free surface (note the optical distortion of the jet tip in the final image).

The simulation neglects viscosity and surface tension, which could have an effect on the detailed jet shape. Nevertheless, these should have a minor role in the total Kelvin impulse, most of which is accumulated when the jet is in its early formation stage. We also note that the boundary integral method does not fully satisfy the no-slip condition, potentially important

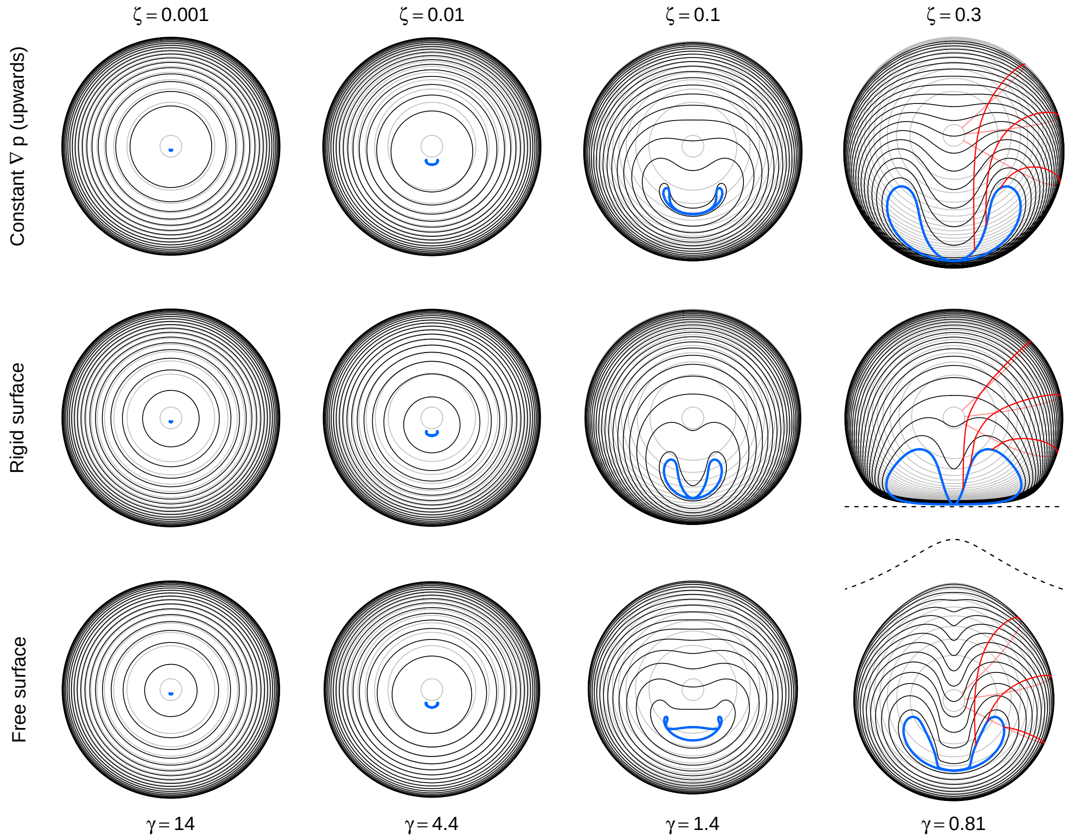

Figure 2.12: Calculated examples of bubbles collapsing in a constant pressure gradient (upper), near a rigid surface (middle) and near a free surface (lower) at corresponding pressure field anisotropy ζ and stand-off γ. The bubble shapes are shown during its growth (grey), collapse (black) and jet impact stage (blue). Surface particle trajectories are shown in red for the bubbles at $\zeta = 0.3$. The dashed lines represent the rigid/free surface.

when the bubble is very close to a rigid surface.

Figure 2.12 displays examples of calculated bubble shapes at different levels of ζ (and corresponding γ, related to ζ via (2.5)), across all regimes. (Here $\zeta = 0.001$ is the limit between weak and intermediate jet regimes, $\zeta = 0.01$ is in the intermediate jet regime, $\zeta = 0.1$ is the limit between intermediate and strong jet regimes, and $\zeta = 0.3$ is in the strong jet regime.) Figure 2.12 illustrates the differences of a bubble collapsing in a constant pressure gradient, near a rigid surface and near a free surface. The differences in the bubble shapes are significantly more pronounced in the strong jet regime compared to the weak and intermediate jet regimes. We show this explicitly by zooming into the bubble shapes at the instant of the jet impact in figure 2.13. One should therefore expect important differences in the quantitative properties of micro-jets in the strong jet regime. In turn, in the intermediate and weak jet regimes the micro-jets are well described by ζ, independently of the origin of the anisotropy. We will verify

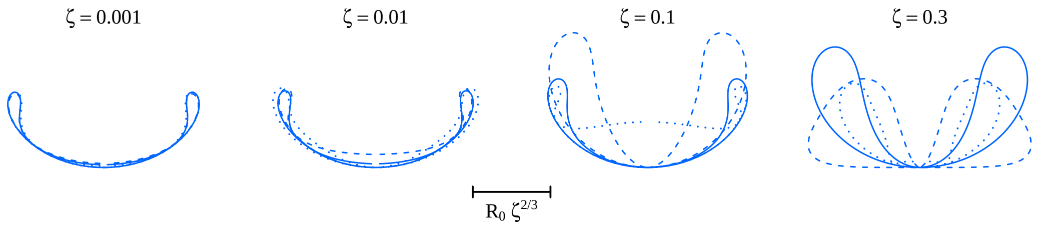

Figure 2.13: Zoomed bubble shapes at the jet impact from figure 2.12. The different jet drivers are indicated by solid (constant ∇p,) dashed (rigid surface) and dotted (free surface) lines. The scale bar shows the characteristic scale of the final bubble as explained in section 2.6.1.

this statement by looking at individual micro-jet parameters in the following sections.

The code used to solve equations (2.9) and (2.10) is available online at https://obreschkow.shinyapps.io/bubbles.

2.5.2 Jet impact time

An interesting parameter characterising a micro-jet is the moment at which the jet pierces the opposite bubble wall during the collapse. The normalised jet impact time is defined as $\Delta T_{\text{jet}}/T_{\text{collapse}}$, where ΔT_{jet} is the time interval from the jet impact to the collapse point (i.e. the minimal radius of the toroidal bubble), and T_{collapse} is the time interval from the maximal bubble volume to the collapse point. The timing of the jet impact is measured through high-speed visualisations either by observing the moment at which a shock wave is emitted due to the impact, such as in figures 2.7 and 2.10, or by looking at the bubble interior for the more obvious cases.

Figure 2.14 displays the normalised jet impact time as a function of ζ and γ. It is evident that the jet pierces the bubble at an earlier stage in the collapse with increasing ζ, i.e. as the bubble deformation becomes more pronounced. In the most deformed cases the jet can pierce the bubble as early as at half of the collapse time. On a linear scale, this parameter varies predominantly in the strong jet regime, but all jets that pierce the bubble (i.e. in strong and intermediate regimes) do so before the collapse. In the intermediate regime, however, the jet impact occurs very close to the collapse moment, i.e. $\Delta T_{\text{jet}}/T_{\text{collapse}} < 1\%$. This is, in fact, how we chose the dividing value $\zeta = 0.1$ between intermediate and strong jets. The offset between data and model around $\zeta = 0.01$ is probably attributed to difficulties of measuring normalised jet impact times below 10^{-4}, skewing the existing data points towards higher values.

In the simulation, we calculate the evolution of the surface of the simply connected bubble up to the moment of jet impact using the boundary integral method explained in section 2.5.1. Beyond this instant, the collapse time of the torus is calculated using the vortex ring model [127], where the complex shape of the vortex ring is approximated by a circular torus of identical

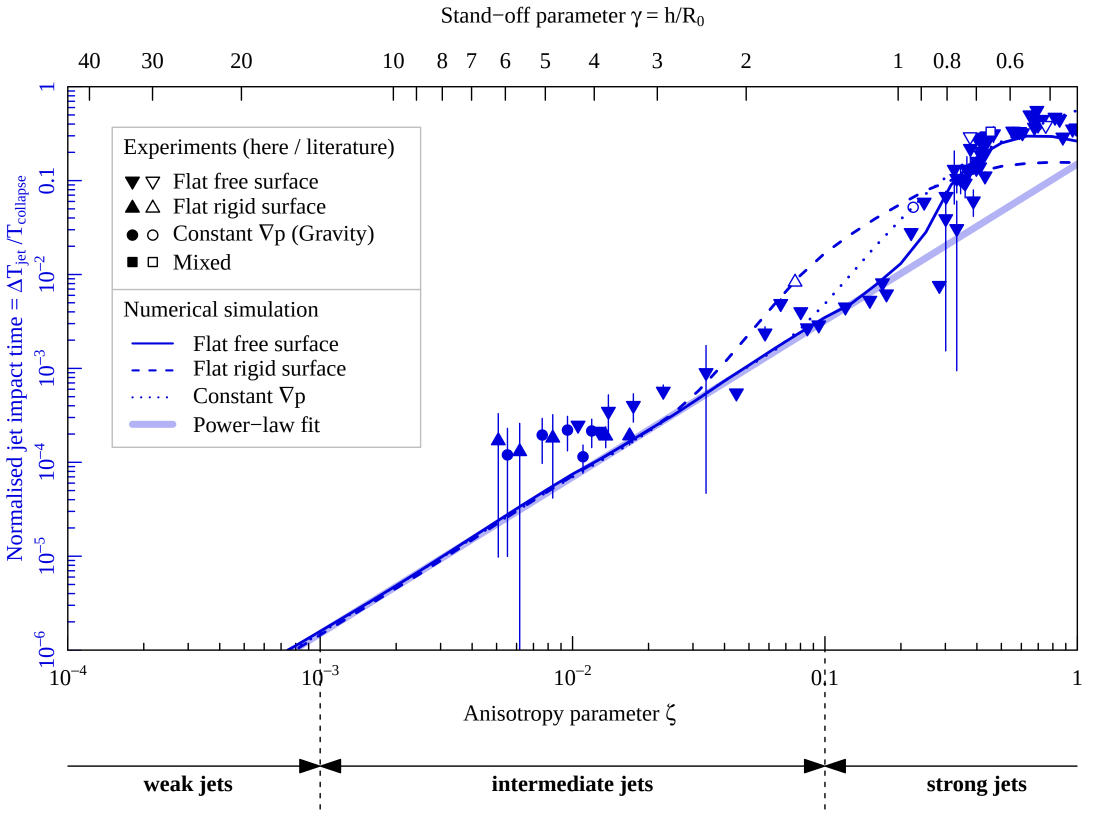

Figure 2.14: Normalised jet impact time as a function of the anisotropy parameter ζ and the stand-off parameter γ. Our experimental data (filled) are compared with literature data (empty): Spark-induced bubbles subject to buoyancy, $R_0 \sim 50$ mm [98], spark-induced bubbles near a free surface and a rigid surface, $R_0 \sim 10$ mm [124], lens-based laser-induced bubbles near a rigid surface, $R_0 = 1.45$ mm [112]. The dotted, dashed and solid lines are the numerical models with a constant pressure gradient, near a rigid surface and near a free surface respectively. The thick line is the power-law fit in equation (2.12), discussed in section 2.6.1.

volume, mean radius, circulation Γ and initial collapse speed. The collapse of this torus is computed using equation (8) in [128]. [3] The numerical calculations agree with the experimental results within their uncertainties. These models are almost identical for the different jet drivers up to approximately $\zeta = 0.03$, with major differences arising in the strong jet regime, in particular for the rigid surface. These discrepancies are probably attributed to the more pronounced differences in the bubble geometries between the different jet drivers, as seen in figure 2.13, for example, at $\zeta = 0.1$. As a consequence, whether the jet impacts on a single point (rigid surface) or on an annular ring (free surface) leads to a different volume of the remaining toroidal bubble, which in turn leads to a longer collapse time.

2.5.3 Jet speed

An important parameter that describes the micro-jet dynamics is the jet speed. Here we define it as the maximum jet speed before the impact on the opposite bubble wall, normalised by the characteristic speed $(\Delta p/\rho)^{1/2}$ [129]. The speed is measured from visualisations of the bubble interior, where the jet is visible inside the bubble prior to the impact (such as in figure 2.9).

Figure 2.15 displays our measurements of the normalised jet speed as a function of ζ and γ, together with selected data from the literature. They reveal a decrease of the normalised jet speed with increasing ζ. This is explained by the jet piercing the bubble earlier at high ζ (as seen in section 2.5.2), when the bubble interface speed is still relatively low. In fact, the jet speed tends to infinity as $\zeta \rightarrow 0$, i.e. as we approach the limit of spherical collapse in the Rayleigh theory. It should be noted that we are unable to measure jet velocities for $\zeta < 3 \cdot 10^{-3}$ with our temporal and spatial resolution.

The measurements for gravity- and free surface-driven jets are in good agreement with the numerical simulations. However, the data points drawn from the literature [112, 130] for jets induced by a rigid surface appear to deviate from the corresponding model at $\gamma > 2$ and $\gamma < 1$. The reasons for this deviation are not entirely clear, but we note that the value of the jet speed depends sensibly on when exactly the measurement is performed. Besides, extracting jet speeds from high-speed images is a challenge, as it requires a highly transparent bubble interface to see the bubble interior in addition to sufficient spatial and temporal resolutions. Another potential caveat with these observations is the optical refraction on the bubble surface. It should be noted that in reality jets are expected to stop accelerating once they approach the speed of sound of the liquid and the potential flow theory starts to fail. This is typically at $\zeta < 0.01$ in standard water conditions (where $(\Delta p/\rho)^{1/2} \approx 10\,\mathrm{m\,s^{-1}}$, hence $U_{\mathrm{jet}} \gtrsim 900\,\mathrm{m\,s^{-1}}$).

Interestingly, in the weak jet regime (where we only have model data) and in the intermediate jet regime up to $\zeta = 0.1$, the jet speed is entirely set by ζ with negligible dependence on the jet driver. Only for asymmetries larger than $\zeta = 0.1$ can we notice a significant deviation of jets associated with a rigid surface relative to those associated with a free surface and/or gravity.

---

[3] Note that the torus collapse time given in eq. (12) of this reference is not sufficient for this purpose, since it neglects the significant initial collapse speed and circularity of the torus.

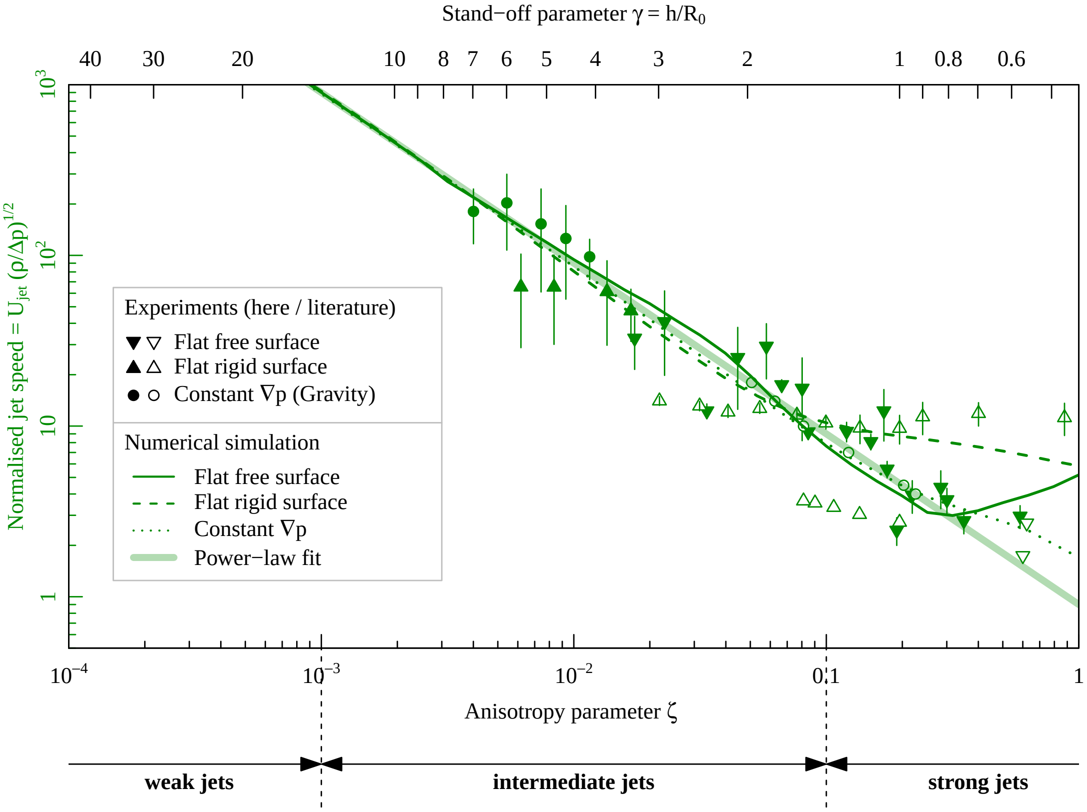

Figure 2.15: Normalised jet speed as a function of the anisotropy parameter ζ and the stand-off parameter γ. Our experimental data (filled) are compared with literature data (empty): Spark-induced bubbles subject to buoyancy, $R_0 \sim 50$ mm [98], spark-induced bubbles near a free surface and a rigid surface, $R_0 \sim 10$ mm [124], lens-based laser-induced bubbles near a rigid surface, $R_0 = 1.45$ mm [112], lens-based laser-induced bubbles near a free surface, $R_0 \sim 1.3$ mm [71], lens-based laser-induced bubbles near a rigid surface, $R_0 = 1.55$ mm [130], focused ultrasound-induced bubbles near a rigid surface, $R_0 = 200$ μm [92]. The dotted, dashed and solid lines are the numerical models with a constant pressure gradient, near a rigid surface and near a free surface respectively. The thick line is the power-law fit in equation (2.12), discussed in section 2.6.1.

2.5.4 Bubble displacement

Another jet parameter worth discussing is the bubble centroid displacement. While not strictly a micro-jet property, this displacement is the most straightforward way to detect a Kelvin impulse. The bubble displacement Δz is defined as the distance travelled by the bubble centroid between bubble generation and collapse, in the rest frame of the liquid. Special care is required when the bubble splits into multiple parts at higher pressure field anisotropies. Here we define the centroid position at the collapse as the position of the jet tip at its impact onto the opposite bubble wall. The experimental results for centroid displacement presented here are normalised by the bubble maximum radius, $\Delta z/R_0$. Note that some authors choose to normalise Δz by the distance h from the flat surface, but this normalisation would not be applicable to other causes of micro-jets such as gravity.

Our measurements of $\Delta z/R_0$ are shown in figure 2.16 as a function of ζ and γ, together with selected data from the literature. In general, we find good agreement between the data points from the different jet drivers, within the measurement uncertainties. Overall, we find an increase of the normalised centroid motion with increasing ζ. A particularly important finding is that, even in the weak jet regime, where the jet speed, impact time and volume (as we will see in section 2.5.6) become cumbersome parameters to measure experimentally, the displacement remains a significant and measurable quantity as evidenced in figure 2.16. The larger scatter of the literature data (empty symbols) might be attributed to the fact that the definition of ‘collapse position’ or ‘centre of minimum bubble volume’ is not always clear for a strongly deformed bubble and therefore the data extraction may not have been done in the same way in all experiments.

The numerical models agree well with the empirical data. In the weak and intermediate jet regimes up to approximately $\zeta = 0.1$, the simulated displacement shows little dependence on the jet driver and is thus almost entirely dictated by the value of ζ. For asymmetries larger than $\zeta = 0.1$, the displacement starts to depend significantly on whether the anisotropy is associated with a rigid surface, free surface or gravity.

2.5.5 Bubble volume at jet impact

The bubble volume V_{impact} at the jet impact is yet another interesting parameter characterising the jet formation. It is a more easily definable size parameter than the jet size itself. The normalised bubble volume at jet impact is defined as $V_{\text{impact}}/V_{\text{max}}$, where $V_{\text{max}} = (4\pi/3)R_0^3$. Experimentally, $V_{\text{impact}} = 2\pi x A$ is obtained from the high-speed visualisations by measuring the area A of the toroid cross-section (averaged between the two cross-sections seen on either side of the jet axis) and the distance x between the geometric centreline of the toroid and the jet axis.

Figure 2.17 shows the normalised bubble volume at jet impact as a function of ζ and γ. This parameter increases with ζ, which is explained by the jet piercing the bubble at an earlier stage

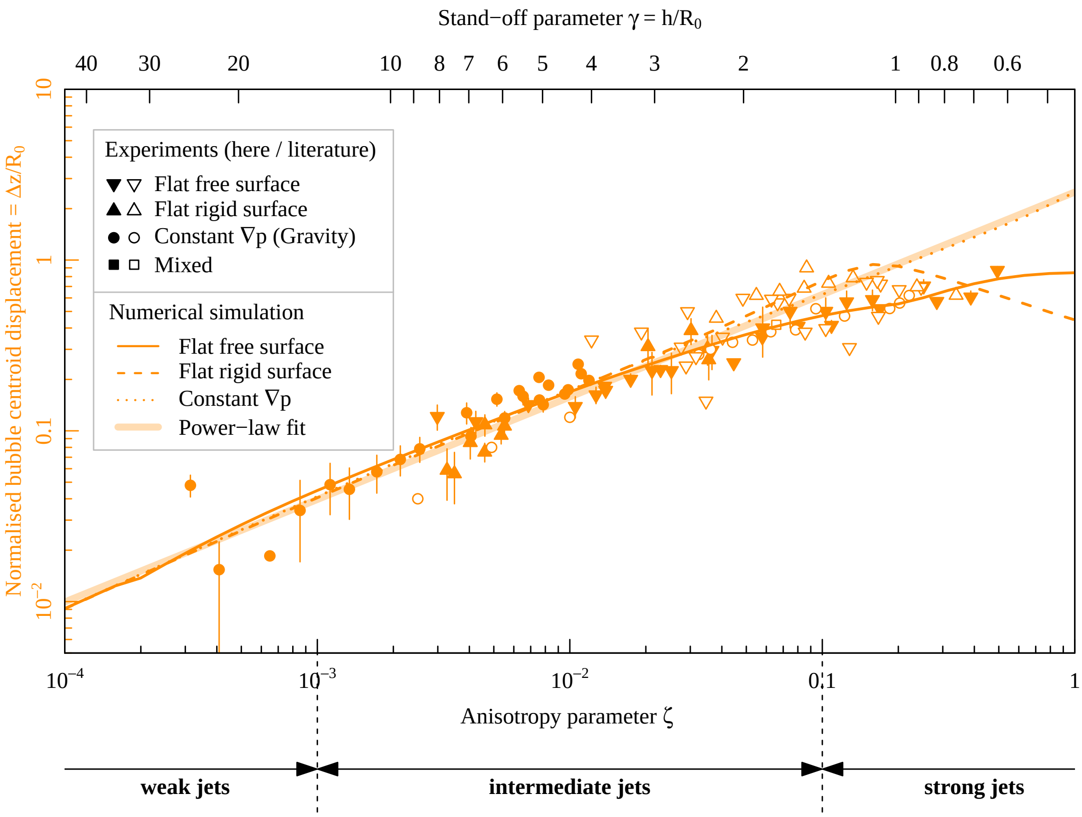

Figure 2.16: Normalised bubble centroid displacement from generation to collapse as a function of the anisotropy parameter ζ and the stand-off parameter γ. Our experimental data (filled) are compared with literature data (empty): Spark-induced bubbles subject to buoyancy, $R_0 \sim 50$ mm [98], spark-induced bubbles near a free surface and a rigid surface, $R_0 \sim 10$ mm [124], lens-based laser-induced bubbles near a rigid surface, $R_0 = 1.55$ mm [131], underwater explosion bubble subject to buoyancy $R_0 = 0.54$ m [132], underwater explosion bubble near a free surface $R_0 \sim 0.17$ m [101], lens-based laser-induced bubbles near a rigid surface, $R_0 = 0.65$ mm [72, 133], lens-based laser-induced bubbles near a rigid and a free surface, $R_0 \sim 1.5$ mm [134]. The dotted, dashed and solid lines are the numerical models with a constant pressure gradient, near a rigid surface and near a free surface respectively. The thick line is the power-law fit in equation (2.12), discussed in section 2.6.1.

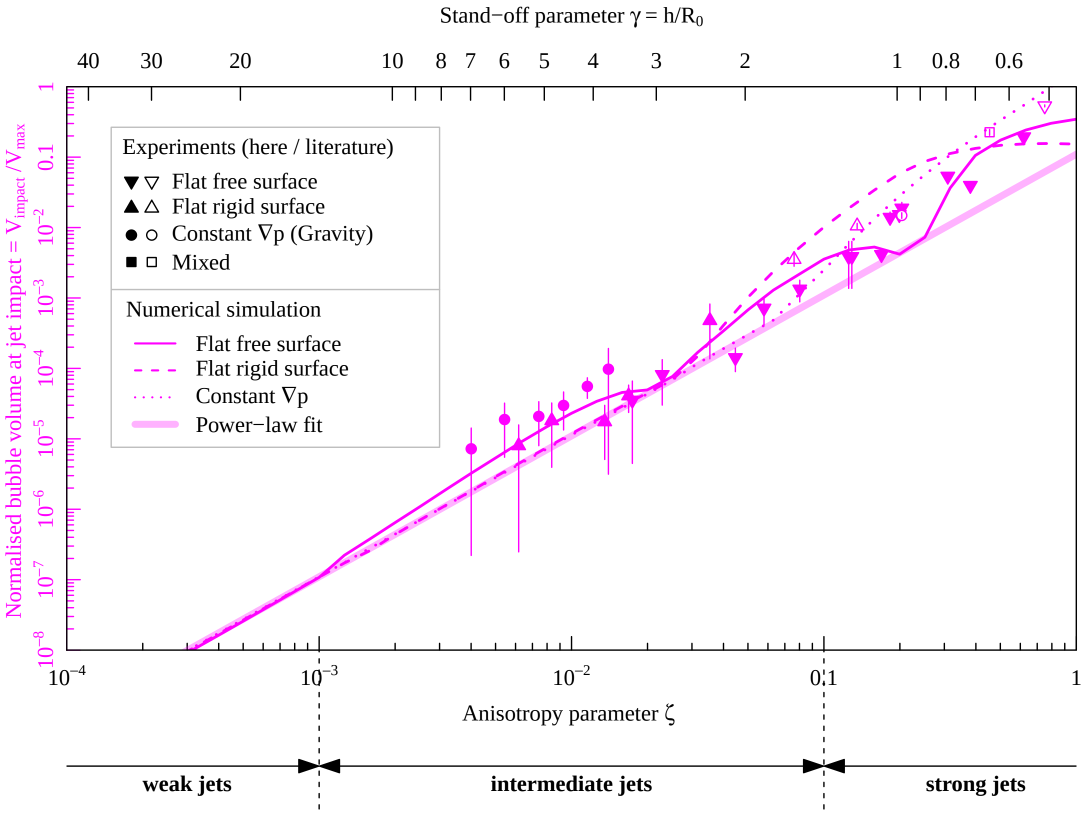

Figure 2.17: Normalised bubble volume at jet impact as a function of the anisotropy parameter ζ and the stand-off parameter γ. Our experimental data (filled) are compared with literature data (empty): Spark-induced bubbles subject to buoyancy, $R_0 \sim 45$ mm [98], spark-induced bubbles near a free surface and a rigid surface, $R_0 \sim 10$ mm [124], lens-based laser-induced bubbles near a rigid surface, $R_0 = 1.45$ mm [112]. The dotted, dashed and solid lines are the numerical models with a constant pressure gradient, near a rigid surface and near a free surface respectively. The thick solid line is the power-law fit in equation (2.12), discussed in section 2.6.1.

during the collapse at higher ζ, when the bubble is still large relative to its final collapse size. The jets from different drivers follow a similar trend.

The numerical calculations agree well with the empirical data within the uncertainties. The different jet drivers exhibit similar trends in the weak and intermediate jet regimes. The differences, especially in the high-intermediate and strong jet regimes, are explained by the different jet shapes (figure 2.12, at $\zeta = 0.1$–0.3). In particular, bubbles collapsing near a free surface produce broad jets that hit the opposite bubble wall on a ring rather than a single point. In this case, the jet separates the bubble into a smaller bubble *and* a torus, resulting in a more complex bubble shape than a simple torus, which therefore yields a different volume. This explains the undulations of the free surface model in figure 2.17 and makes the bubble volume at jet impact, together with the jet impact timing, the most sensitive parameter to jet drivers.

2.5.6 Vapour-jet volume

The final jet parameter discussed in this paper is the post-collapse vapour-jet volume. The scaling of the vapour-jet volume V_{jet} (figure 2.3b), normalised by the rebound volume V_{rebound}, as a function of ζ has been investigated in the intermediate jet regime in [46]. The data points from this reference are replotted in figure 2.18, along with new data for the free surface, as a function of ζ and γ. The empirical result was a linear relation (thick line in figure 2.18),

$$\frac{V_{\text{jet}}}{V_{\text{rebound}}} \approx 5.4\zeta, \tag{2.11}$$

valid across a large range of bubble sizes, liquid pressures and viscosities (varied by a factor 30 using glycerol additions). The authors justified the proportionality between $V_{\text{jet}}/V_{\text{rebound}}$ and ζ based on Kelvin impulse considerations. They also presented a critical value $\zeta_c \approx 4 \cdot 10^{-4}$, such that in situations with $\zeta < \zeta_c$, the micro-jet does not pierce the bubble wall and no vapour-jet emerges from the rebound bubble. This value is approximately consistent with our choice of $\zeta = 10^{-3}$ as the dividing value between the intermediate and weak jet regimes (section 2.4.1). For a more detailed discussion of the vapour-jet volume, we refer to the original work [46].

2.6 Discussion

2.6.1 Power-law approximations

The dimensionless jet parameters discussed in sections 2.5.2–2.5.6 mainly vary with the anisotropy parameter ζ. We also identified a secondary dependence on the jet driver (gravity versus surfaces). According to figures 2.14–2.18, this secondary dependence generally becomes negligible in the weak and intermediate jet regimes ($\zeta < 0.1$). Furthermore, in these regimes the unique relations between ζ and the jet parameters appear to be closely matched by power laws, in particular for the jet speed, the bubble displacement and the vapour-jet volume. A

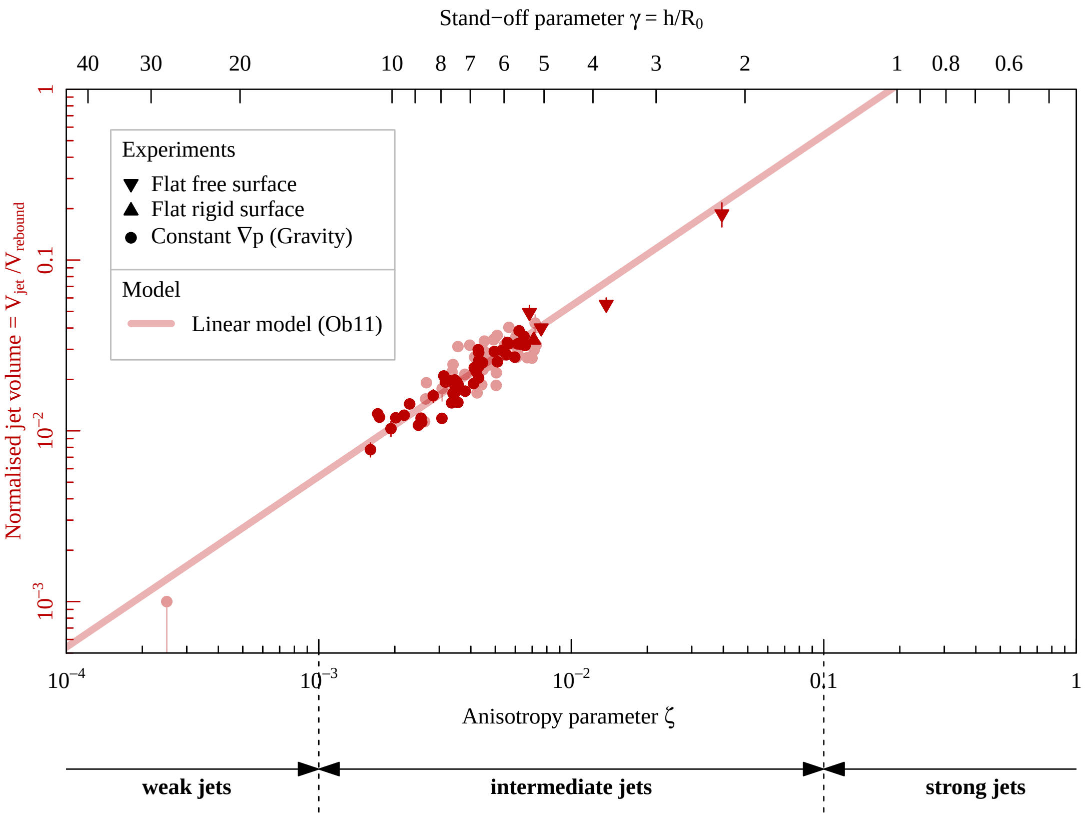

Figure 2.18: Scaling law for the post-collapse bubble vapour-jet volume. Light data points indicate results from variable gravity ($0g$, $1.2g$, $1.4g$, $1.6g$ and $1.8g$ where g=9.81 ms^{-2}) and dark points are from normal gravity ($1g$). Maximal bubble radius R_0 is varied in the range 1-7 mm, liquid pressure p_0 in the range 8-80 kPa and the dynamic viscosity η in the range 1-30 mPa s. The majority of the data points for the constant pressure gradient, and the theoretical model (solid line) in equation (2.11) are from [46].

chi-square fit to the simulated models over the range $\zeta = 10^{-4}$–0.1 with uniform weight in $\log(\zeta)$ yields

$$\left.\begin{array}{rcll} \Delta T_{\rm jet}/T_{\rm collapse} & = & 0.15\zeta^{5/3} & \text{(normalised jet impact time),} \\ U_{\rm jet}/(\Delta p/\rho)^{1/2} & = & 0.9\zeta^{-1} & \text{(normalised jet speed),} \\ \Delta z/R_0 & = & 2.5\zeta^{3/5} & \text{(normalised bubble displacement),} \\ V_{\rm impact}/V_{\rm max} & = & 0.11\zeta^2 & \text{(normalised bubble volume at jet impact),} \\ V_{\rm jet}/V_{\rm rebound} & = & 5.4\zeta & \text{(normalised volume of vapour-jet).} \end{array}\right\} \qquad (2.12)$$

The last relation is not a fit to numerical models, but the empirical equation (2.11), repeated for completeness. These power laws are represented by the thickest lines in figures 2.14–2.18 and are synthesised in figure 2.19 together with the range of numerical results spanned by various

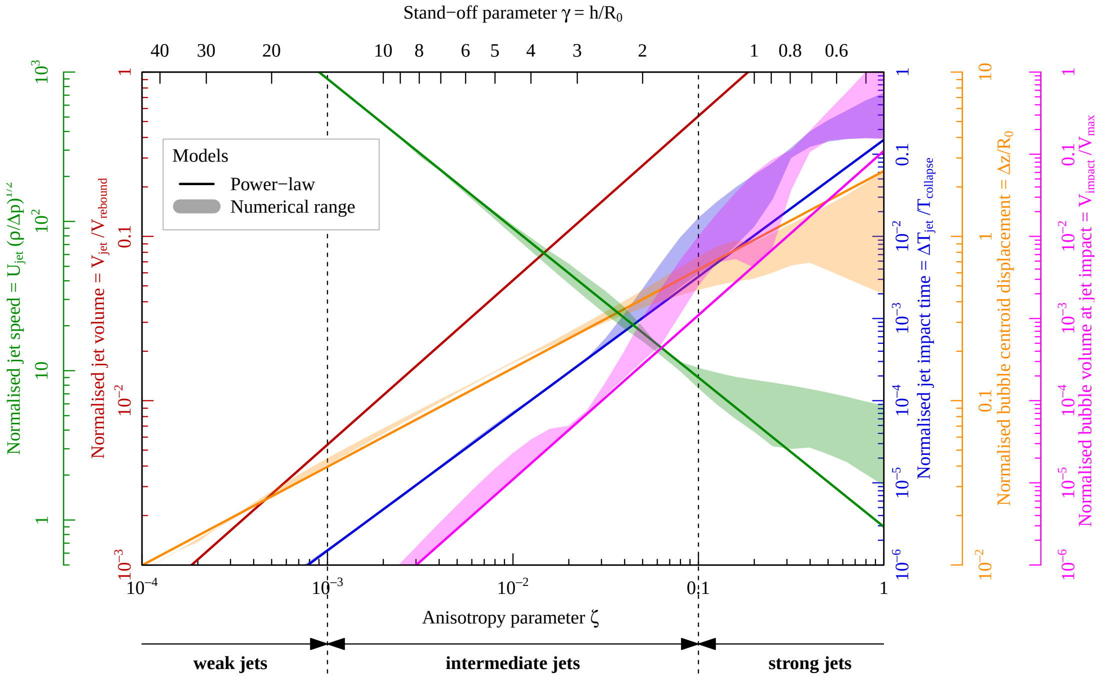

Figure 2.19: Summary of the micro-jet parameters across all regimes. The power-laws for the normalised jet impact time, jet speed, bubble centroid displacement, bubble volume at jet impact and vapour-jet volume [46] are plotted as a function of the anisotropy parameter ζ and the stand-off parameter γ. The shaded areas describe the range spanned by the different jet drivers, which is calculated numerically (see figures 2.14-2.17).

jet drivers (shaded regions). The power laws provide a simple tool to predict the dynamics of an aspherical bubble collapse in a large range of conditions, without the need for complex computations.

To understand the reasons for this power-law behaviour and explain the power-law exponents, we recall that power laws are generally an expression of scale-free behaviour. ‘Scale-free’ means that the physical system is geometrically similar, independently of its overall scale. Of course, the *whole evolution* of a jetting bubble is *not* scale-free across a range of ζ, because the maximum bubble radius is independent of ζ, while the jet parameters vary with ζ. Approximate scale-freeness can, however, be found at the *single instant* when the jet impacts on the opposite side of the bubble wall (blue lines in figure 2.12). For small values of ζ ($\zeta < 0.1$), the bubble at this instant has a universal bowl-like shape. Only the *size* varies with ζ, but the bubble *shape* is independent of the value and the origin of ζ.

Scale-freeness at the jet impact stage means that all lengths scale proportionally to the characteristic bubble radius $r \equiv R(t)/R_0$ at this stage. Corresponding volumes and masses scale as r^3. To find the characteristic scaling of velocities, we note that, for small ζ, the bubble deformation occurs very late in the collapse phase (i.e. $r \ll 1$). In this phase, the time evolution of the bubble radius satisfies $\dot{r} = r^{-3/2}$, which is the asymptotic behaviour of the Rayleigh equation as $r \to 0$ [55]. Given that masses scale as r^3 and velocities as $r^{-3/2}$, linear momentum (= product of mass and velocity) scales as $r^3\dot{r} = r^{3/2} = \dot{r}^{-1}$. Since the momentum of the bubble is proportional to ζ (see (2.3)), we find $r \sim \zeta^{2/3}$ (see figure 2.13) and $\dot{r} \sim \zeta^{-1}$. This explains the numerical scalings $V_{\text{impact}} \sim \zeta^2$ and $U_{\text{jet}} \sim \zeta^{-1}$.

The asymptotic equation of the spherical collapse $\dot{r} = r^{-3/2}$ solves to give $r \sim \tilde{t}^{2/5}$, where $\tilde{t} = 1 - t$ is the time backwards from the collapse point, normalised to the collapse time [55]. Thus, for small ζ, we expect $\Delta T_{\text{jet}} \sim r^{5/2} \sim (\zeta^{2/3})^{5/2} = \zeta^{5/3}$, as confirmed by the numerical simulation.

Our interpretation of the vapour-jet scaling is more speculative, since we did not simulate the formation of this jet. One might naively expect the volume of the vapour-jet V_{jet} to scale as $r^3 \sim \zeta^2$, just like V_{impact}. However, the vapour-jet is not a feature at the instant of the jet impact. Hence the arguments of scale-freeness of the previous paragraphs do not apply. The correct reasoning is that the volume of the vapour-jet is the part of the micro-jet that actually gets pushed through the bubble wall during the time interval of the rebound. The vapour-jet volume therefore depends both on the characteristic micro-jet volume and on the jet speed. Consequently, we expect $V_{\text{jet}} \sim r^3\dot{r} \sim \zeta^2\zeta^{-1} = \zeta$, in agreement with the experimental results. This explanation should be tested against more detailed modelling of the vapour-jet formation in future work.

Finally, the normalised displacement of the bubble centroid Δz is expected to scale as $\Delta z \sim r \sim \zeta^{2/3}$, if this displacement occurs uniquely at the final collapse stage, where the scale-free picture applies. The power-law exponent of $2/3 = 0.666\ldots$ is indeed the best fit to the simulations for very small values of ζ ($\zeta < 10^{-3}$), where almost all the bubble motion occurs just before and after the final collapse point. However, for larger values of ζ, a non-negligible fraction of the bubble motion occurs at larger bubble radii, where $|\dot{r}| < r^{-3/2}$ according to equation (7) in [55]. Hence, the power-law index between Δz and ζ must drop below 0.666. This prediction is consistent with our numerical finding that Δz scales approximately as $\Delta z \sim \zeta^{0.6} = \zeta^{3/5}$ over the range $\zeta < 0.1$.

2.6.2 Application of scaling relations

The power laws are a useful predictive tool of the micro-jet physics in known pressure field anisotropies $\zeta < 0.1$. In the strong jet regime ($\zeta > 0.1$) (and in the high-intermediate regime for the jet impact time and bubble volume at jet impact), more accurate, nonlinear scaling relations can be obtained numerically for specific jet drivers, as shown in figures 2.14–2.18 and tabulated in Appendix 2.8.2.

An interesting consequence of the jet scalings with ζ is that one may reciprocally use a known jet observable to estimate the pressure field anisotropy in which the bubble is collapsing. Consequently, the measurement of a single jet observable suffices to estimate the rest of

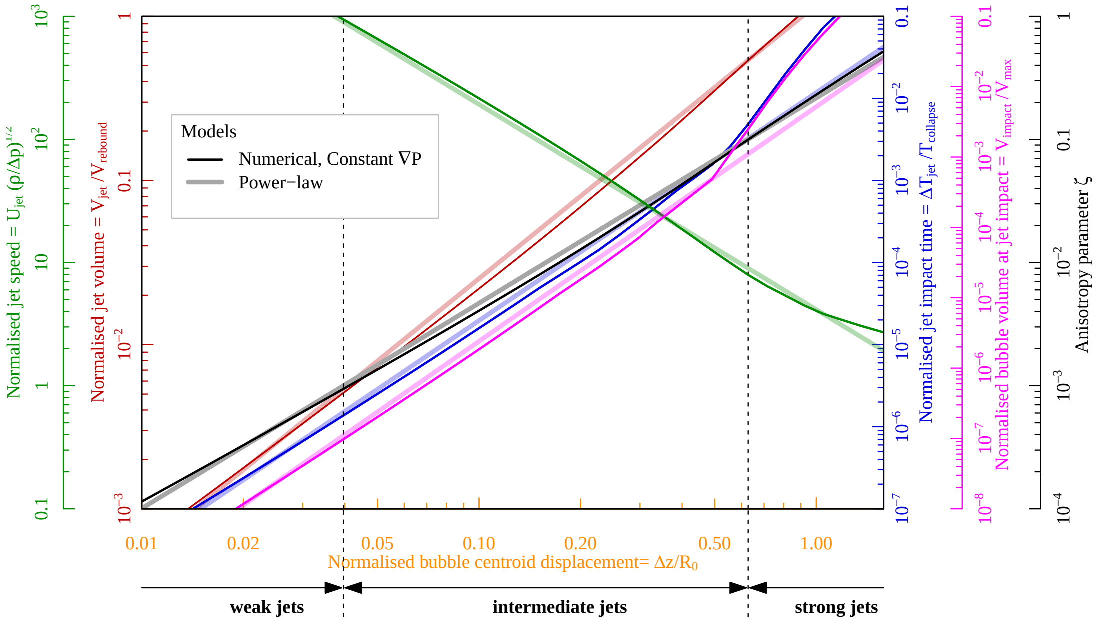

Figure 2.20: The pressure field anisotropy parameter ζ and the normalised jet impact time, the normalised jet speed, the normalised bubble volume at jet impact and the normalised jet volume [46] are plotted as a function of the normalised bubble centroid displacement for jets driven by a constant pressure gradient. The simulated models and the power-law fits are plotted with dark and light lines, respectively.

the parameters. The bubble centroid displacement, for instance, presents the advantage of being the easiest measurable quantity of an aspherical bubble collapse across a large range of pressure field anisotropies. It therefore serves as a simple and useful predictor of the full micro-jet physics. As an example, the particular case of jets driven by a constant pressure gradient ∇p is presented in figure 2.20, where the various jet parameters and the anisotropy parameter ζ are plotted as a function of the bubble displacement $\Delta z/R_0$. For reference, we also show the results corresponding to the simple power laws. Their similarity in the weak and intermediate regime ($\zeta < 0.1$) implies that figure 2.20 would look nearly the same for other jet drivers in this regime.

2.6.3 Limitations

Let us conclude this discussion by addressing a few limitations of the unified perspective offered by the single anisotropy parameter ζ. As mentioned before, the micro-jets in the strong jet regime, where more complex jet morphologies are produced, cannot be fully described by ζ independently of the jet drivers. At these high anisotropies, strong variations in the jet parameters for different jet origins occur as a direct consequence of the higher-order terms in equation (2.1), as discussed in section 2.4.3. Predictions in this regime should be made numerically for the specific jet drivers.

Combining the effect of multiple jet drivers generally produces jets that follow the same scaling laws as jets from a single driver in the weak and intermediate jet regimes. However, attention should be paid to situations where several strong jet drivers act simultaneously in opposite directions (e.g. gravity and rigid boundary in [98]), as they may yield a low resultant ζ although the higher-order terms in equation (2.1) remain significant. This can result in bubble splitting, producing, for example, the 'hourglass' bubble [67], the dynamics of which cannot be predicted by our approach.

So far, our investigations have mainly focused on flat rigid or free surfaces. Curved [72], flexible [95] and composite [133] surfaces would require specific corrections to $\boldsymbol{\zeta}$ in eq. (2.6), which would serve as an interesting addition to the diverse family of micro-jets. Furthermore, as a consequence of the assumption that viscosity and surface tension play a minor role in the micro-jet dynamics, our approach is limited to bubbles of a certain scale in water and we do not account for jets produced by capillary phenomena. Viscosity and surface tension, which become important in, for example, biomedical applications that deal with micrometre-sized bubbles in viscous liquids, break the scale-freeness and may change the trends with ζ. It would be an interesting opening for future work.

Finally, it should be noted that the lifetime of bubbles investigated in the present study includes the bubble growth, which strongly affects the subsequent motion (in particular for bubbles near a flat surface at $\gamma < 1$). Our numerical tool (see section 2.5.1) provides the option to exclude the growth phase and start with a perfectly spherical bubble at its maximal radius.

2.7 Conclusion

In this work, we conducted a qualitative and quantitative analysis of the micro-jet dynamics of a single cavitation bubble in a large range of conditions. By introducing a dimensionless anisotropy parameter ζ, we arrived at a unified framework describing micro-jets of virtually any strength, caused by various jet drivers, in particular gravity, free surfaces, rigid surfaces and combinations thereof. This successful unification of the micro-jet family through ζ, a normalised version of the Kelvin impulse, fosters Blake's view that the Kelvin impulse is a 'fundamental … enormously valuable concept' [69].

The main contribution of this work is the realisation that, in normalised coordinates, ζ fully defines the jet physics, once the jet driver (e.g. gravity or nearby boundaries) has been identified. Furthermore, for small Kelvin impulses ($|\mathbf{I}| < R_0^3\sqrt{\Delta p\rho}/2$, that is for $\zeta < 0.1$) the jet physics becomes virtually independent of the jet driver. This powerful aspect of the Kelvin impulse comes about despite – or rather because of – the concerns raised by [135] about this impulse being an integral value.

We have investigated, both experimentally and numerically, how different jet characteristics vary with ζ. The normalised jet impact time, the jet speed, the bubble centroid displacement, the bubble volume at jet impact and the vapour-jet volume can all be approximated by power laws of ζ up to $\zeta \approx 0.1$, independently of the jet drivers. A single observable may be used to predict another jet parameter or estimate the pressure field anisotropy, as shown in figure 2.20.

The micro-jets have been phenomenologically classified into three distinct regimes: weak, intermediate and strong jets. We showed that such a categorisation presents a useful thinking tool to distinguish visually very different jets, which nonetheless all fit in the unified framework of the ζ parameter. Weak jets ($\zeta < 10^{-3}$) hardly pierce the bubble, but remain within the bubble throughout the collapse and rebound. Intermediate jets ($10^{-3} < \zeta < 0.1$) pierce the opposite bubble wall very late in the collapse phase and clearly emerge during the rebound. Strong jets ($\zeta > 0.1$) pierce the bubble significantly before the moment of collapse and their dynamics is strongly dependent on the jet driver.

The presented results might serve as a step towards unifying the quickly diversifying research field of cavitation and towards reaching a unified framework for the energy distribution between all collapse-related phenomena. A precise control of the power of micro-jets would allow, for instance, the attenuation of detrimental jet-induced erosion as well as the targeting of cancerous cells or highly localised drug delivery. Such new research avenues may benefit from the framework and predictive tools presented here.

2.8 Appendix

2.8.1 Mathematical derivations

The evolution of a spherical bubble of radius R in a liquid of density ρ and constant overpressure Δp (relative to the bubble content) is governed by the Rayleigh equation [51]

$$\frac{3}{2}\left(\frac{\mathrm{d}R}{\mathrm{d}T}\right)^2 + \frac{\mathrm{d}^2R}{\mathrm{d}T^2}R = -\frac{\Delta p}{\rho}. \tag{2.13}$$

We can define the time T such that the bubble is at the maximal radius R_0 at $T = 0$. Equation (2.14) then implies that the radius vanishes at $T = \pm T_\mathrm{c}$, where $T_\mathrm{c} = \xi R_0(\rho/\Delta p)^{1/2}$ and ξ is a numerical constant, called the Rayleigh factor. Upon normalising the radius to $r \equiv R/R_0 \in [0,1]$ and the time to $t \equiv T/T_\mathrm{c} \in [-1,1]$, the Rayleigh equation can be simplified to a dimensionless first order differential equation [55],

$$\left(\frac{\mathrm{d}r}{\mathrm{d}t}\right)^2 = \frac{2}{3}\xi^2\left(r^{-3}-1\right). \tag{2.14}$$

Taking the square-root on both sides (with minus sign on the RHS), and integrating $t = 0...1$ and $r = 1...0$, this equation readily solves to

$$\int_0^1 f\,\mathrm{d}t = \sqrt{\frac{3}{2}}\xi^{-1}\int_0^1 \frac{f\,\mathrm{d}r}{\sqrt{r^{-3}-1}}, \tag{2.15}$$

for any time-dependent function f. Upon performing the substitution $s \equiv r^3$ (hence $\mathrm{d}r = \frac{1}{3}s^{-2/3}\mathrm{d}s$), we get

$$\int_0^1 f\,\mathrm{d}t = \frac{1}{\sqrt{6}\xi}\int_0^1 \frac{f\,\mathrm{d}s}{s^{1/6}\sqrt{1-s}}. \tag{2.16}$$

Equation (2.16) is the central equation, from which we can derive the collapse time and various instances of the Kelvin impulse.

Collapse time

To get the Rayleigh factor ξ, it suffices to set $f = 1$ in Equation (2.16). The LHS then becomes $\int_0^1 \mathrm{d}t = 1$, and hence

$$\xi = \frac{1}{\sqrt{6}}\int_0^1 \frac{\mathrm{d}s}{s^{1/6}\sqrt{1-s}} = \frac{1}{\sqrt{6}}B\left(\frac{5}{6},\frac{1}{2}\right) \approx 0.9146813565, \tag{2.17}$$

where $B(x,y) \equiv \int_0^1 t^{x-1}(1-t)^{y-1}\mathrm{d}t$ is the beta-function.

Kelvin impulse of a bubble in an external pressure gradient

Let us start with Blake's equation [69] for the momentum (Kelvin impulse) acquired by the liquid during the growth and collapse of a spherical bubble in a constant pressure gradient,

$$\mathbf{I} = \nabla p \int_{-T_c}^{T_c} V\,\mathrm{d}T, \tag{2.18}$$

where V is the volume of the bubble at time T. (Note that Blake presents this equation for the particular case of a gravity-driven gradient $|\nabla p| = \rho g$ and he uses the different convention that the bubble is generated at $T = 0$ and collapses at T_c.) Equation (2.18) can be rewritten as

$$\mathbf{I} = 2\nabla p \int_0^{T_c} V\,\mathrm{d}T = \frac{8\pi}{3}\nabla p \int_0^{T_c} R^3\mathrm{d}T = \frac{8\pi}{3}T_c R_0^3 \nabla p \int_0^1 r^3\mathrm{d}t = \frac{8\pi\xi}{3}R_0^3(\Delta p\rho)^{1/2}\boldsymbol{\zeta}\int_0^1 r^3\mathrm{d}t. \tag{2.19}$$

To evaluate the integral on the RHS we use equation (2.16) with $f = r^3 \equiv s$,

$$\int_0^1 r^3\mathrm{d}t = \frac{1}{\sqrt{6}\xi}\int_0^1 \frac{s\,\mathrm{d}s}{s^{1/6}\sqrt{1-s}} = \frac{B(11/6,1/2)}{B(5/6,1/2)} = \frac{5}{8}. \tag{2.20}$$

Hence,

$$\mathbf{I} = \frac{5\pi}{3\sqrt{6}} B\left(\frac{5}{6}, \frac{1}{2}\right) R_0^3 \sqrt{\Delta p \rho}\, \boldsymbol{\zeta} \approx 4.789 R_0^3 \sqrt{\Delta p \rho}\, \boldsymbol{\zeta}, \tag{2.21}$$

which concludes the derivation of equation (2.3). Note that $R_0^3 \sqrt{\Delta p \rho}$ has the dimension of momentum, as required.

Kelvin impulse of a bubble near a rigid/free surface

Blake [69] also derives the equation of the Kelvin impulse for a bubble near a rigid or free surface,

$$|\mathbf{I}_{\text{surface}}| = \frac{\rho}{16\pi h^2} \int_{-T_\text{c}}^{T_\text{c}} (4\pi R^2 \dot{R})^2 \mathrm{d}T, \tag{2.22}$$

where h is the distance to the rigid or free surface. This expression can be rewritten as

$$|\mathbf{I}_{\text{surface}}| = \frac{2\pi\rho}{h^2} \int_0^{T_\text{c}} R^4 \dot{R}^2 \mathrm{d}T = \frac{2\pi\rho}{h^2} T_\text{c}^{-1} R_0^6 \int_0^1 r^4 \dot{r}^2 \mathrm{d}t = \frac{2\pi}{\xi} (\Delta p \rho)^{1/2} R_0^3 \gamma^{-2} \int_0^1 r^4 \dot{r}^2 \mathrm{d}t. \tag{2.23}$$

To evaluate the integral we use equation (2.16) with $f = r^4 \dot{r}^2 = \frac{2}{3}\xi^2 s^{4/3}(s^{-1} - 1) = \frac{2}{3}\xi^2 s^{1/3}(1 - s)$,

$$\int_0^1 r^4 \dot{r}^2 \mathrm{d}t = \frac{2\xi}{3\sqrt{6}} \int_0^1 s^{1/6} (1 - s)^{1/2} \mathrm{d}s = \frac{1}{9} B\left(\frac{7}{6}, \frac{3}{2}\right) B\left(\frac{5}{6}, \frac{1}{2}\right). \tag{2.24}$$

Hence,

$$|\mathbf{I}_{\text{surface}}| = \frac{2\pi\sqrt{2}}{3\sqrt{3}} B\left(\frac{7}{6}, \frac{3}{2}\right) R_0^3 \sqrt{\Delta p \rho}\, \gamma^{-2} \approx 0.934 R_0^3 \sqrt{\Delta p \rho}\, \gamma^{-2} \tag{2.25}$$

which concludes the derivation of equation (2.4). Equating equations (2.21) and (2.25) yields

$$\zeta = \frac{4B(7/6, 3/2)}{5B(5/6, 1/2)} \gamma^{-2} \approx 0.195 \gamma^{-2}, \tag{2.26}$$

which is the exact expression of equation (2.5).

2.8.2 Numerical data

Data from the numerical calculations are listed in table 2.1.

$\log_{10}\zeta$	$\log_{10}(\Delta T_{\text{jet}}/T_{\text{collapse}})$			$\log_{10}(U_{\text{jet}}/(\Delta p/\rho)^{\frac{1}{2}})$			$\log_{10}(\Delta z/R_0)$			$\log_{10}(V_{\text{impact}}/V_{\text{max}})$		
	c.∇p	rigid	free	c.∇p	rigid	free	c.∇p	rigid	free	c.∇p	rigid	free
-4.0	-7.48	-7.45	-7.47	3.96	3.96	3.96	-2.04	-2.04	-2.04	-8.97	-8.97	-8.99
-3.9	-7.30	-7.30	-7.30	3.86	3.87	3.86	-1.97	-1.98	-1.97	-8.77	-8.77	-8.79
-3.8	-7.14	-7.15	-7.15	3.76	3.77	3.76	-1.91	-1.91	-1.91	-8.57	-8.57	-8.60
-3.7	-6.98	-6.99	-6.98	3.66	3.67	3.66	-1.84	-1.84	-1.86	-8.37	-8.37	-8.40
-3.6	-6.82	-6.83	-6.81	3.56	3.56	3.56	-1.78	-1.78	-1.78	-8.17	-8.17	-8.20
-3.5	-6.65	-6.66	-6.64	3.45	3.46	3.46	-1.71	-1.71	-1.70	-7.96	-7.97	-8.00
-3.4	-6.49	-6.50	-6.46	3.35	3.36	3.36	-1.64	-1.65	-1.62	-7.76	-7.77	-7.79
-3.3	-6.32	-6.33	-6.29	3.25	3.26	3.26	-1.58	-1.58	-1.55	-7.56	-7.57	-7.59
-3.2	-6.15	-6.17	-6.11	3.15	3.16	3.16	-1.51	-1.52	-1.48	-7.36	-7.37	-7.38
-3.1	-5.99	-6.00	-5.96	3.05	3.06	3.06	-1.45	-1.46	-1.41	-7.16	-7.17	-7.17
-3.0	-5.82	-5.84	-5.80	2.95	2.96	2.95	-1.39	-1.39	-1.35	-6.96	-6.96	-6.97
-2.9	-5.65	-5.67	-5.64	2.85	2.86	2.85	-1.32	-1.33	-1.29	-6.76	-6.76	-6.65
-2.8	-5.48	-5.51	-5.48	2.75	2.76	2.75	-1.26	-1.27	-1.23	-6.56	-6.59	-6.42
-2.7	-5.32	-5.34	-5.32	2.65	2.66	2.65	-1.19	-1.20	-1.17	-6.36	-6.36	-6.19
-2.6	-5.15	-5.18	-5.15	2.54	2.55	2.55	-1.13	-1.14	-1.11	-6.15	-6.15	-5.96
-2.5	-4.98	-5.01	-4.98	2.44	2.45	2.43	-1.07	-1.08	-1.05	-5.95	-5.95	-5.73
-2.4	-4.81	-4.83	-4.80	2.34	2.34	2.34	-1.01	-1.01	-1.00	-5.75	-5.75	-5.49
-2.3	-4.65	-4.66	-4.63	2.24	2.23	2.25	-0.94	-0.95	-0.94	-5.55	-5.54	-5.27
-2.2	-4.48	-4.48	-4.46	2.14	2.13	2.16	-0.88	-0.89	-0.88	-5.35	-5.33	-5.04
-2.1	-4.31	-4.31	-4.29	2.04	2.02	2.07	-0.82	-0.83	-0.83	-5.15	-5.13	-4.83
-2.0	-4.16	-4.14	-4.13	1.93	1.91	1.98	-0.76	-0.77	-0.77	-4.94	-4.93	-4.64
-1.9	-4.00	-3.98	-3.98	1.83	1.80	1.89	-0.70	-0.71	-0.72	-4.75	-4.73	-4.47
-1.8	-3.85	-3.82	-3.82	1.73	1.69	1.80	-0.64	-0.64	-0.67	-4.56	-4.54	-4.34
-1.7	-3.67	-3.66	-3.66	1.63	1.58	1.72	-0.59	-0.58	-0.62	-4.36	-4.35	-4.31
-1.6	-3.50	-3.48	-3.50	1.52	1.48	1.62	-0.53	-0.52	-0.57	-4.16	-4.16	-4.11
-1.5	-3.32	-3.24	-3.32	1.41	1.38	1.53	-0.47	-0.46	-0.52	-3.93	-3.83	-3.77
-1.4	-3.13	-2.94	-3.14	1.31	1.28	1.43	-0.42	-0.39	-0.48	-3.72	-3.40	-3.47
-1.3	-2.97	-2.63	-2.96	1.20	1.20	1.29	-0.36	-0.33	-0.44	-3.52	-2.99	-3.17
-1.2	-2.81	-2.32	-2.79	1.10	1.12	1.15	-0.31	-0.26	-0.40	-3.31	-2.62	-2.89
-1.1	-2.59	-2.02	-2.62	1.00	1.06	1.01	-0.26	-0.19	-0.36	-2.96	-2.29	-2.67
-1.0	-2.31	-1.77	-2.46	0.90	1.02	0.88	-0.20	-0.12	-0.33	-2.60	-1.99	-2.45
-0.9	-2.01	-1.58	-2.32	0.81	0.99	0.77	-0.15	-0.06	-0.30	-2.23	-1.72	-2.32
-0.8	-1.70	-1.40	-2.11	0.73	0.96	0.68	-0.09	-0.03	-0.28	-1.88	-1.47	-2.28
-0.7	-1.41	-1.25	-1.88	0.65	0.94	0.59	-0.04	-0.04	-0.26	-1.55	-1.23	-2.38
-0.6	-1.14	-1.10	-1.55	0.58	0.92	0.49	0.02	-0.07	-0.22	-1.25	-1.06	-2.14
-0.5	-0.92	-1.00	-1.04	0.53	0.90	0.48	0.08	-0.11	-0.18	-0.97	-0.95	-1.44
-0.4	-0.72	-0.91	-0.75	0.49	0.88	0.50	0.13	-0.16	-0.14	-0.71	-0.88	-0.98
-0.3	-0.58	-0.85	-0.69	0.44	0.85	0.55	0.19	-0.21	-0.11	-0.48	-0.83	-0.76
-0.2	-0.47	-0.82	-0.53	0.39	0.83	0.59	0.25	-0.26	-0.09	-0.24	-0.81	-0.62
-0.1	-0.35	-0.80	-0.53	0.31	0.79	0.65	0.32	-0.31	-0.08	0.00	-0.81	-0.52
0.0	-0.25	-0.81	-0.58	0.23	0.77	0.71	0.40	-0.35	-0.07	0.23	-0.82	-0.46

Table 2.1: Data from the numerical calculations explained in section 2.5.1 and presented in figures 2.14-2.17 for the normalised jet impact time, normalised jet speed, normalised bubble centroid displacement and normalised bubble volume at jet impact as a function of the anisotropy parameter ζ. The data are given for three different jet drivers: constant pressure gradient (c.∇p), rigid surface and free surface.

3 Shock waves

Shock waves from nonspherical cavitation bubbles

Reproduced version of

Outi Supponen, Danail Obreschkow, Philippe Kobel, Marc Tinguely, Nicolas Dorsaz and Mohamed Farhat. *Shock waves from nonspherical cavitation bubbles.* Physical Review Fluids **2**(9) 093601 (2017). DOI: 10.1103/PhysRevFluids.2.093601,

with the permission of American Physical Society.[1]

The author's contribution:
The author made the major part of the experiments and the analysis. She was responsible for building the experiment to fulfill to the requirements of the parabolic flights (62nd ESA parabolic flight campaign and 1st Swiss parabolic flight), and coordinated the team for these flights. She was the first author of this publication.

Abstract

We present detailed observations of the shock waves emitted at the collapse of single cavitation bubbles using simultaneous time-resolved shadowgraphy and hydrophone pressure measurements. The geometry of the bubbles is systematically varied from spherical to very nonspherical by decreasing their distance to a free or rigid surface or by modulating the gravity-induced pressure gradient aboard parabolic flights. The nonspherical collapse produces multiple shocks that are clearly associated with different processes, such as the jet impact and the individual collapses of the distinct bubble segments. For bubbles collapsing near a free surface, the energy and timing of each shock are measured separately as a function of the anisotropy parameter ζ, which represents the dimensionless equivalent of the Kelvin impulse. For a given source of bubble deformation (free surface, rigid surface, or gravity), the normalized shock energy depends only on ζ, irrespective of the bubble radius R_0 and driving pressure Δp. Based on this finding, we develop a predictive framework for the peak pressure and energy of shock waves from nonspherical bubble collapses. Combining statistical analysis

---

[1] Supplementary movies may be found at https://doi.org/10.1103/PhysRevFluids.2.093601

of the experimental data with theoretical derivations, we find that the shock peak pressures can be estimated as jet impact-induced hammer pressures, expressed as $p_h = 0.45\left(\rho c^2 \Delta p\right)^{1/2} \zeta^{-1}$ at $\zeta > 10^{-3}$. The same approach is found to explain the shock energy decreasing as a function of $\zeta^{-2/3}$.

3.1 Introduction

Shock waves are one of the most destructive phenomena occurring during the collapse of cavitation bubbles and therefore a topic of long-standing interest. The associated pressures, reaching values on the order of GPa [40, 41], are able to wear metallic surfaces, which is a classic concern for ship propellers and hydraulic turbines [109, 111, 5]. Further victims of cavitation-induced damage are, for example, artificial heart valves [7], liquid-propelled rocket engines [10] and the prey of a mantis shrimp [14]. The damaging power can also be exploited for beneficial uses such as in medical [25] (e.g., shock wave lithotripsy [136, 15] and cancer therapy [20, 25]) and cleaning [27] applications. However, predictive tools to characterize the key properties of cavitation-driven shocks are limited. In the quest of mitigating the harm they may cause or maximizing their benefit, we here make detailed observations of shocks of single cavitation bubbles and propose a framework to predict their strengths.

Much progress has been made in the prediction of the damage potential of shock waves emitted by spherically collapsing bubbles [137, 138, 41, 139, 140]. However, doing so for non-spherically collapsing bubbles is still an open problem. Bubbles may deform under the effect of, for example, nearby surfaces, inertial forces such as gravity, or passing shock waves. The collapse shock wave strengths have been shown, both experimentally and numerically, to vary with the bubble sphericity for bubbles collapsing near a rigid wall [94, 113, 82, 141]. Shocks from bubbles collapsing under the effect of a passing shock wave have been shown to be sensitive to the latter's timing and strength [116]. The shocks emitted at the collapse of an individual bubble are often referred to as a single event, yet it is known that deformed bubbles that are pierced by high-speed microjets produce several shock waves from multiple locations upon collapse [113, 47, 122]. However, understanding the contribution of each shock emission mechanism to the final damage characteristics and a systematic study on the influence of the bubble deformation on them are still lacking, as recently pointed out by Lauterborn and Vogel [142]. Although numerical simulations offer an excellent means to reproduce complex shock wave scenarios associated with nonspherical collapses [79, 83, 84, 85], observations for their validation are limited. Furthermore, we still lack an understanding of how the shocks from bubbles deformed by distinct sources differ.

In this work, shock wave energies and pressures are systematically measured as a function of the various bubble parameters and asymmetries. The objective is to understand how the deformation of bubbles affects their detailed collapse shock wave emission. In particular, we aim to estimate, through visualizations and pressure measurements, the strengths and the timings of the distinct shock waves produced at the collapse of bubbles with geometries varying from highly spherical to strongly deformed by a nearby free surface. These data are then compared to bubbles deformed by a nearby rigid surface and by the hydrostatic pressure gradient, which is modulated in variable gravity aboard parabolic flights (60th and 62nd European Space Agency parabolic flight campaigns and the first Swiss parabolic flight). The advantage of a gravity-induced pressure gradient to deform bubbles is its uniformity in time and space that leads to similar bubble collapse shapes across a wide range of bubble asymmetries [143]. Furthermore, any smooth pressure field can be approximated to first order by such a uniform pressure gradient. We exploit the large number of data and a broad parameter space to reach an empirical model for predicting the shock strengths for nonspherical bubbles, which is backed up by theoretical arguments. This model applies the scaling laws for microjets, which we have recently developed in detail [143], to the shock wave emission of deformed cavitation bubbles.

The deformation of bubbles collapsing near surfaces is usually quantified by the standoff parameter $\gamma = h/R_0$, where h is the distance between the bubble center and the surface and R_0 is the maximum bubble radius. Deformations caused by near surfaces and gravity can be compared by using the vector parameter $\boldsymbol{\zeta}$ [143, 46]:

$$\boldsymbol{\zeta} = \begin{cases} -\rho \mathbf{g} R_0 \Delta p^{-1} & \text{(gravitational field)} \\ +0.195\gamma^{-2}\mathbf{n} & \text{(flat free surface)} \\ -0.195\gamma^{-2}\mathbf{n} & \text{(flat rigid surface)} \end{cases} \tag{3.1}$$

where ρ is the liquid density, $\mathbf{g}$ is the gravitational acceleration, $\Delta p = p_0 - p_v$ is the driving pressure (where p_0 is the static pressure of the unperturbed liquid at the location of the bubble and p_v is the vapor pressure), and $\mathbf{n}$ is the unit vector normal to the surface, in the direction from the surface to the bubble. Here $\boldsymbol{\zeta}$ is essentially the dimensionless equivalent of the Kelvin impulse, which is the linear momentum acquired by the liquid during the growth and the collapse of the bubble [68]. A higher $\zeta \equiv |\boldsymbol{\zeta}|$ causes a more pronounced bubble deformation and delineates key parameters of the microjet, such as the jet speed or the jet impact timing, almost irrespective of the source of deformation for $\zeta < 0.1$ [143]. We henceforth primarily use ζ to quantify bubble deformation, but also display the equivalent γ for convenience.

This paper is structured as follows. Section 3.2 presents the experimental methods, describing the setup and the relevant calibrations. Section 3.3 shows detailed observations of single and multiple shock waves emitted by bubbles near a free surface. A framework for predicting shock peak pressures and energies is then proposed in Sec. 3.4, along with comparisons between shocks from bubbles deformed by different sources (free and rigid surfaces and gravity). Finally, the results are discussed in Sec. 3.5.

3.2 Experimental methods

The central components of our experimental setup are shown in Fig. 3.1. A pulsed laser is expanded and focused in demineralized water by an immersed parabolic mirror, which

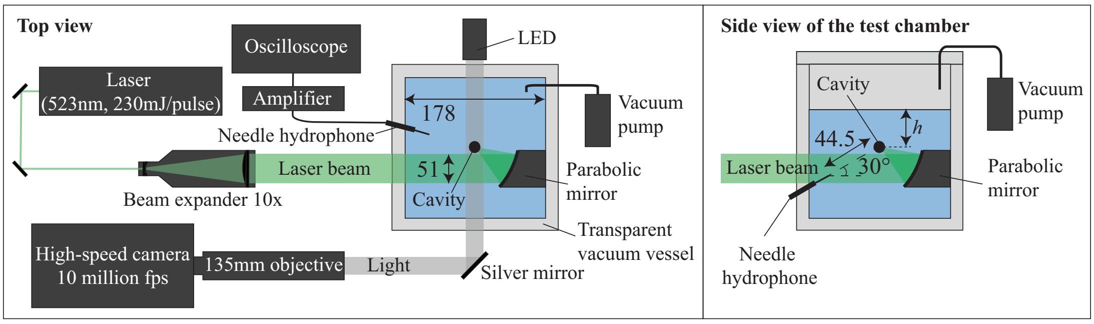
Top view
Oscilloscope
LED
Laser
(523nm, 230mJ/pulse)
Amplifier
178
Vacuum
pump
Needle hydrophone
Laser beam
51
Parabolic
mirror
Cavity
Beam expander 10x
Transparent
vacuum vessel
High-speed camera
10 million fps
135mm objective
Light
Silver mirror
Side view of the test chamber
Cavity
Vacuum
pump
44.5
h
Laser beam
30°
Parabolic
mirror
Needle
hydrophone

Figure 3.1: Top and side view schematics of the experimental setup. The dimensions are given in mm.

produces a pointlike plasma and thereby an initially highly spherical bubble [97] that grows and subsequently collapses. The bubble and the associated shock waves are visualized using shadowgraphy with an ultrahigh-speed camera (Shimadzu HPV-X2) reaching filming speeds up to 10×10^6 frames/s (fps) with a 50-ns exposure time and a collimated backlight beam from a light-emitting diode. The driving pressure Δp can be adjusted by varying the static pressure p_0 in the test chamber between 0.08 and 1 bar with a vacuum pump. Tuning the laser power generates bubbles of energies $E_0 = (4\pi/3)R_0^3\Delta p$ ranging from 0.1 to 28 mJ. This parameter space leads to a wide range of maximum bubble radii $R_0 = 1$–10 mm, which are large enough for viscosity and surface tension to have a negligible effect on the bubble dynamics [119].

To modulate the bubble deformation, we vary the bubble's distance to a surface ($h \sim 3$–30 mm) and/or the perceived gravity ($|\mathbf{g}| \sim 0$–$2\,g$, where $g = 9.81$ ms^{-2}), in addition to varying R_0 and Δp. The maximum radii are obtained from the recorded collapse time T_c (i.e., half oscillation time) of the bubble as $R_0 = 1.093\,T_c(\Delta p/\rho)^{1/2}\kappa^{-1}$ [51], where κ is a factor depending on the source and level of deformation. For bubbles collapsing near a free surface, κ is a lifetime-shortening factor that can be approximated as $\kappa \approx 1 - 0.102\gamma^{-1}$ [134]. The bubbles deformed by gravity or a nearby rigid surface in this work are at $\zeta < 10^{-2}$ and therefore the deformations are weak enough for them to justify the assumption $\kappa \approx 1$. All measurements are made at room temperature. Additional details on our experimental setup and the parabolic flights may be found in Ref. [97].

A needle hydrophone (75 μm sensor, manufactured by Precision Acoustics) is used to record the pressure of the shock waves. The bandwidth of this hydrophone is guaranteed to extend above 30 MHz and is thus capable of a detailed sampling of the shock waveform and of disentangling multiple fronts. The rise time upper bound is found to be approximately 15 ns, estimated from the time it takes for the pressure signal of the steep shock wave produced at the explosive bubble generation (Fig. 3.2) to rise from 10% to 90% of its maximum amplitude. The actual rise time of the shock wave is likely to be even shorter [144]. The pressure signal, represented by an electrical voltage, is amplified and recorded at a 100-MHz sampling frequency by an oscilloscope. The hydrophone sensor is located at a distance of $d = 44.5$ mm from the bubble center at an angle of 30° below the horizontal plane with a planar incidence

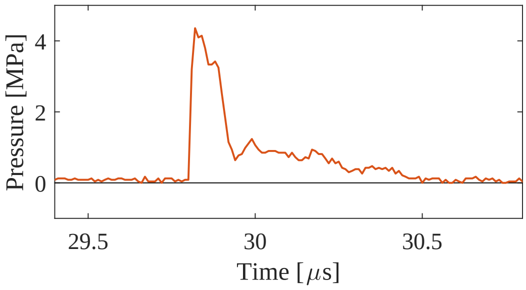

Figure 3.2: Typical hydrophone pressure signal of the shock wave emitted at the bubble generation. Here $t = 0$ μs corresponds to the time instant of bubble generation.

of the shock wave onto the sensor. The shock waves take approximately 30 μs to reach the hydrophone after being generated. Being thin (needle thickness is 0.3 mm) and located far relative to the bubble size, the presence of the hydrophone needle is assumed to have a negligible effect on the bubble dynamics.

We assume spherical propagation of the shock waves and estimate their energies as

$$E_S = aU_{\max}^b \int U(t)^2 \mathrm{d}t \tag{3.2}$$

where $U(t)$ (V) is the hydrophone voltage signal (containing the full shock wave scenario in the case of multiple collapse shocks, but excluding any reflections from boundaries), $U_{\max}$ is the maximum value of $U(t)$, and a and b are calibration constants. If the shock propagated with no energy dissipation, then $a = 4\pi d^2 \left(\rho c\right)^{-1} G^{-2}$ [94] (where c is the sound speed in the liquid and G is the gain in units of V/Pa) and $b = 0$. An exponent $b > 0$ is used to approximately compensate for nonlinear dissipation (e.g., due to inelastic heating, induced microcavitation, etc.), whose relative effect increases with pressure. As the precise gain G is unknown in our current setup and nonlinear dissipation is expected, we treat a and b as positive free parameters. We fit these parameters to simultaneously satisfy two conditions: (i) the energy of the laser-induced shock at the bubble generation $E_{\mathrm{S,gen}}$ scales linearly with the bubble energy E_0 [94] and (ii) the total energy of the shock(s) emitted at the bubble collapse $E_{\mathrm{S,coll}}$ is bounded by the difference between the bubble energy E_0 and the rebound energy E_{reb}. For bubbles that collapse spherically ($\zeta < 10^{-3}$) and produce no jets, we assume $E_{\mathrm{S,coll}} \approx E_0 - E_{\mathrm{reb}}$ [48]. We find that a is such that $E_{\mathrm{S,gen}}/E_0 \approx 0.75$ (i.e., 43% of the absorbed laser energy goes into the generation shock and 57% goes into the bubble) and $b \approx 0.45$, indicating slight nonlinear dissipation. Figure 3.3 displays the calibrated energies for both bubble generation and collapse shock waves for various E_0 and ζ, clearly showing the linear relationship between $E_{\mathrm{S,gen}}$ and E_0 and that the collapse shock energies tend to be lower for increasing ζ. Pressures are then computed from the calibrated energies as $p(t) = U(t)/G$, where the gain G is determined for each individual bubble separately as $G^2 = 4\pi d^2 \left(\rho c\right)^{-1} \int U(t)^2 \mathrm{d}t / E_S$. Using a variable G allows for the comparison of the signals obtained in different conditions, for which the recorded pressures are differently affected by the shock's nonlinear dissipation.

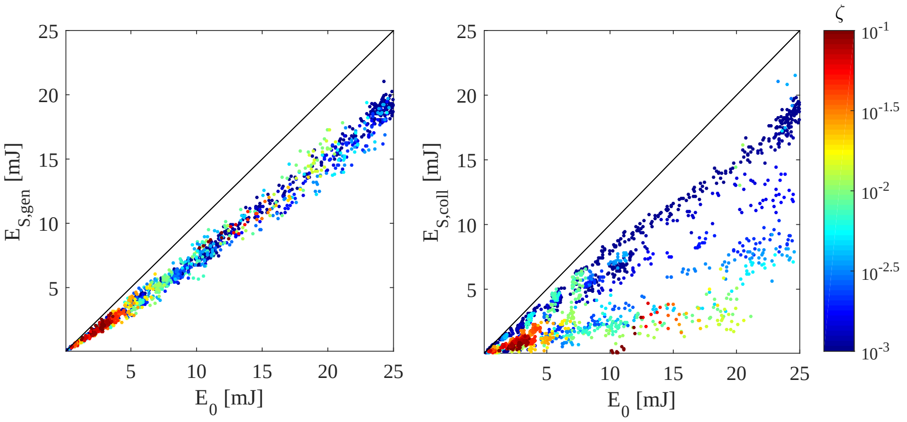

Figure 3.3: Energies of shock waves emitted at bubble generation (left) and collapse (right) for various bubble energies E_0. The colors indicate the level of ζ. The solid lines show $E_S = E_0$.

3.3 Detailed observations

3.3.1 Spherical collapse

A spherical bubble collapse emits a single shock front that is spherically symmetrical, as visualized in Fig. 3.4a. This shock is well studied and arises from the compression of the incondensable gases inside the bubble overcoming the high pressures in the liquid around the bubble in the final collapse stage, which makes the liquid rapidly invert its motion as the bubble rebounds [137]. The gases inside the bubble are compressed so violently that they heat up to temperatures reaching levels of visible light emission, a phenomenon known as luminescence, which is visible in frame 5 of Fig. 3.4a and implies that the bubble reaches its minimum size during the 50-ns exposure time of this image. The rebound bubble then forms a compression wave that propagates outward and quickly steepens to form a shock front, as can be seen in frames 6–8. The corresponding hydrophone measurement of the shock wave is shown in Fig. 3.4b. Assuming $1/r$ spreading of the spherical wave and the luminescence spot in Fig. 3.4a as the minimum bubble size ($R_{\min} \approx 100\ \mu$m), the lower bound for the peak pressure at the bubble wall at minimum bubble radius is estimated as 2 GPa, which is in agreement with previously estimated values [142]. The actual value is likely much higher, because we overestimate the minimum bubble radius that our apparatus is not able to capture due to the luminescence and the dark region around the bubble hiding this information. When using the Keller-Miksis model [61], where we adjust the initial gas pressure by numerically fitting the model to the observed radial evolution of the bubble (first and second oscillations), we would expect a minimum bubble radius of $R_{\min} \approx 15\ \mu$m and thereby a peak pressure of 12 GPa.

In agreement with previous research, we find that the most energetic shock waves are emitted by highly spherical collapses, reaching up to about 90% of the initial bubble energy. The bubbles here are found to emit a single shock front at anisotropies up to $\zeta \approx 10^{-3}$ (equivalent

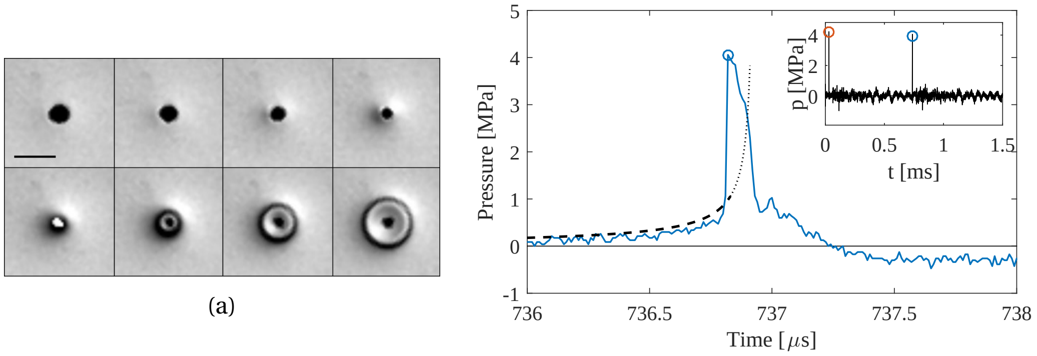

(a)

(b)

Figure 3.4: Cavity of $R_0 = 3.8$ mm collapsing spherically at $\zeta < 10^{-3}$ and emitting a single shock wave: (a) High-speed shadowgraph visualization. The interframe time is 100 ns and the black bar shows the 1 mm scale. (See supplementary movie.) (b) Pressure recorded by the hydrophone. The inset shows the whole bubble oscillation, where the orange and blue circles refer to generation and collapse shock wave peaks pressures, respectively. The dashed line shows $p(t) - p_0$, where $p(t)$ is the Rayleigh pressure model computed from Eq. (3.3) up to the shock peak, and the dotted line extends the curve to the time at which the bubble is estimated to reach a radius of $R = 100$ μm.

to $\gamma \approx 14$), which is also the approximate limit for the appearance of a microjet piercing the bubble in our setup [143].

In the last stages of the collapse, the pressure in the liquid near the bubble wall increases to values so high that it deflects light, producing the shaded ring around the bubble in Fig. 3.4a (frames 2–4). This pressure has previously been predicted to reach thousands of bars [51, 137] and experimentally detected using Mach-Zehnder interferometry [145] or elevated ambient pressures [146]. However, it is interesting that our setup is able to visualize it using simple shadowgraphy at atmospheric pressure. This is due to the bubble's high initial sphericity allowing it to reach very small radii upon its exceptionally spherical collapse.

The incompressible model for the pressure distribution around the bubble, developed by Rayleigh a century ago, is given as follows [51]:

$$\frac{p}{p_0} = 1 + \frac{R}{3r}\left(\frac{R_0^3}{R^3} - 4\right) - \frac{R^4}{3r^4}\left(\frac{R_0^3}{R^3} - 1\right) \tag{3.3}$$

where r is the radial distance from the bubble center. Considering the lower bound for the compression ratio of the bubble in Fig. 3.4a ($R_0/R_{\mathrm{min}} > 40$), we expect the maximum peak pressure to be on the order of GPa in the incompressible framework. The pressure buildup is visible in the hydrophone signal in Fig. 3.4b as a relatively slow rise preceding the peak pressure of the shock. We may compute the pressure evolution in time from Eq. (3.3) at the radial distance where the hydrophone is located ($r = 44.5$ mm), assuming the time

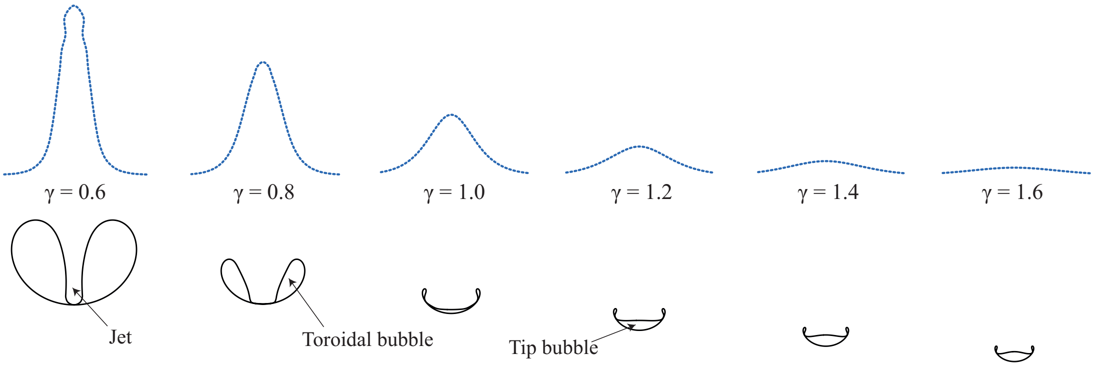

Figure 3.5: Illustration of the bubble shapes at jet impact for different standoff distances γ from the free surface. The corresponding values for ζ from left to right are $\zeta = 0.54$, 0.30, 0.20, 0.14, 0.10, and 0.076. The shapes of the free surface are shown as a dotted line. The shapes have been obtained numerically using potential flow theory.

evolution of the bubble radius to follow the analytical approximation $R(t) \approx R_0\left(1-t^2\right)^{2/5}$ [55] (where t is the time normalized to collapse time T_c), down to $R_{\min} \approx 100\ \mu$m. The computed pressures from Eq. (3.3) can be roughly compared with the hydrophone signal if the delay in the far field caused by the finite sound speed is accounted for. Furthermore, the shock pressure peak is assumed to represent a time approximately 100 ns preceding the final collapse instant, for the shock wave is expected to propagate the first ~ 300 μm with supersonic speeds [144]. The average shock speed during the exposure of the first frame after the collapse is estimated approximately as 3000 ms^{-1} from Fig. 3.4a and therefore the shock wave is indeed estimated to reach the hydrophone $\Delta t \approx 102$ ns earlier than the pressure buildup, of which the information is assumed to propagate at the sound speed. As can be seen in Fig. 3.4b, the computed (dashed line) and measured (solid line) pressure evolutions almost up to the signal peak are surprisingly similar. The good agreement is remarkable considering our unconventional pressure calibration. The model is not able to reproduce the shock wave because it is incompressible (dotted line), and when the bubble reaches a radius of $R = 100\ \mu$m, the predicted pressure at the hydrophone location is $p - p_0 = 3.8$ MPa, which is close to the measured peak pressure very likely by coincidence. The pressure rise, in addition to the tensile part of the shock wave tail, is the clearest difference between the measured waveform from a spherical collapse and that of the bubble generation (Fig. 3.2).

3.3.2 Non-spherical collapse: Bubbles near a free surface

The dynamics of bubbles near free surfaces has been extensively studied in the past experimentally, theoretically, and numerically [147, 148, 67, 149, 71, 150, 99, 84], yet no study to date has focused specifically on their shock wave emission. The advantage of studying bubbles near a free surface is the contact avoidance between the bubble and the surface, allowing thus free collapse and rebound dynamics, as the bubble migration and the microjet are directed

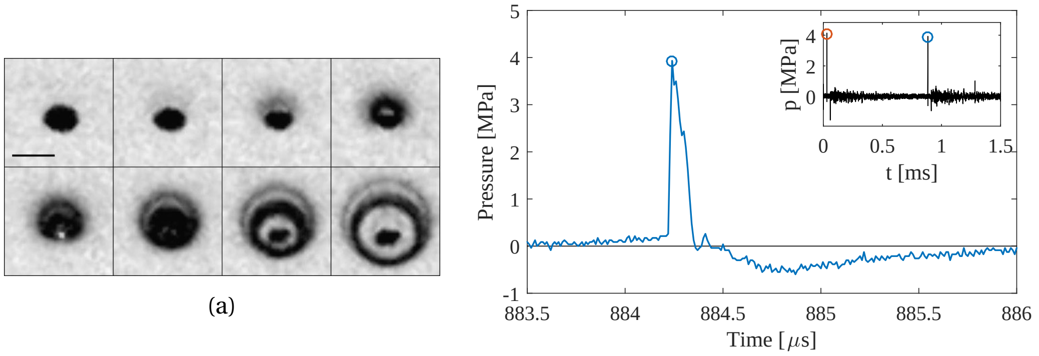

(a)

(b)

Figure 3.6: Cavity of $R_0 = 4.1$ mm at $\zeta = 3.8 \times 10^{-3}$ ($\gamma = 7.2$). (a) High-speed shadowgraph visualization. The interframe time is 100 ns and the black bar shows the 1-mm scale. (See supplementary movie.) (b) Pressure recorded by the hydrophone. The inset shows the whole bubble oscillation, where the orange and blue circles refer to generation and collapse shock wave peak pressures, respectively.

away from the surface (contrary to a rigid surface). While bubbles near a free surface form microjets that have characteristics similar to bubbles deformed by a rigid surface [143], their shapes at the final collapse stages have significant differences, which may give us some further insight into the distinct shock wave emission mechanisms. In particular, for $\gamma = 1$–3, the micro-jet formed during the collapse is broad and impacts the opposite bubble wall on a ring rather than a single point, some examples being illustrated in Fig. 3.5. At lower values of γ, the microjet becomes narrow and the spike formed on the free surface increases in height. The shapes in Fig. 3.5 were obtained numerically using potential flow theory (boundary integral method [143, 70, 67, 71][2]) and have previously been validated by their good agreement with experiments [143].

We now present observations of shock waves from bubbles collapsing near a free surface at different levels of ζ. Nonspherically collapsing bubbles that produce microjets generate multiple shock waves, which are clearly observed on the shadowgraph images at $\zeta > 10^{-3}$. However, they only become clearly distinct events on the hydrophone signal beyond $\zeta \sim 8 \times 10^{-3}$ ($\gamma \sim 5$).

Figure 3.6 shows selected shadowgraph images and the corresponding hydrophone pressures for a bubble collapsing at $\zeta = 3.8 \times 10^{-3}$. The first sign of asymmetry in the bubble collapse, together with the bubble's displacement, is the shaded region appearing near the upper bubble wall where the downward microjet is forming [starting from frame 2 in Fig. 3.6a]. It is similar to the gradual pressure buildup observed for the spherical collapse in Fig. 3.4a, but not spherically symmetric. It is also in agreement with reported numerical simulations of jetting bubbles, finding higher pressures at the root of the jet relative to the rest of the pressure field [83, 84, 85, 89]. The shaded region eventually surrounds most of the bubble in frame 5 and two clear shock fronts are visible in frame 6 following the collapse. We observe luminescence at the tip of the bubble in frame 5, which also appears to be the center of the most pronounced shock wave visible in the subsequent images. Although it is much weaker compared to the light emitted in the spherical case, the observed flash suggests a high gas compression between the jet and the opposite bubble wall. Interestingly, the first shock front in Fig. 3.6a is produced on the side of the bubble where the initial pressure rise in the liquid occurred. The hydrophone is unable to distinguish the first shock wave from the rest due to its location and temporal resolution, but it records the gradual pressure rise occurring on the sides of the bubble preceding the main shock wave [Fig. 3.6b].

---

[2] The code for the numerical simulations is available online at https://obreschkow.shinyapps.io/bubbles [143].

Figures 3.7a–3.7h show images and the corresponding measured shock pressures for more deformed bubbles, collapsing at different distances from the free surface at $\zeta = 2.9 \times 10^{-2}$, 4.6×10^{-2}, 0.19, and 0.33. The recorded peak pressures are significantly lower compared to the more spherical cases and many distinct shock wave events are observed. The first pressure peak in all cases corresponds to the water hammer induced by the jet impact. Such a shock has been observed in the past for nonspherically collapsing bubbles both experimentally [113, 47, 122] and numerically [79, 84]. It produces a toruslike shock wave due its contact on the opposite bubble wall not being a single point but a circular line (see Fig. 3.5), clearly visible on the images as two shock source points on the sides of the bubble. If the jet is broad enough, the hydrophone may detect two individual pressure peaks, such as in Fig. 3.7f, owing to such toruslike shock having two fronts on the hydrophone axis that reach the sensor. Subsequently, the jet separates a part of the vapor at the tip from the rest of the bubble, with this separation being particularly clear in Figs. 3.7c and 3.7e as a horizontal line that cuts the bubble and implies that the vapor in that zone has disappeared. It is difficult to tell with certainty that the first shock wave results from a jet impact in Fig. 3.7a due to the short time intervals between the distinct events. However, observing several bubbles between $\zeta = 2.9 \times 10^{-2}$ and 4.6×10^{-2} (of which the results are summarized later in Sec. 3.3.3), a systematic variation of the shock timings and strengths with ζ was noted. The identification of each peak in Fig. 3.7b was therefore done accordingly. The peak pressure associated with the jet impact decreases with an increasing ζ and is barely detected at $\zeta = 0.33$. At $\zeta = 2.9 \times 10^{-2}$ and 4.6×10^{-2} [Figures 3.7a–3.7d], the jet impact is followed by the collapse of the toroidal bubble. The associated shocks are toruslike and meet in the jet axis in the middle of the bubble, which is known to sometimes produce a counterjet, a vertical columnlike cluster of microcavities [47, 143]. The torus collapse shock may also yield two individual peaks in the pressure signal, such as in Figs. 3.7d and 3.7f. The peak pressure of the torus collapse shock first decreases with increasing ζ [Figs 3.7b and 3.7d], and then increases again slightly [Figs. 3.7f and 3.7h]. The next pressure peak in Figs. 3.7b and 3.7d corresponds to the tip bubble collapse. It appears to be the dominant shock in the collapse scenario at these ζ. The tip bubble collapse shock triggers a second collapse of the rebounding toroidal bubble, which emits a further shock wave manifested as the fourth pressure peak in the signal. The second torus collapse pressure peak

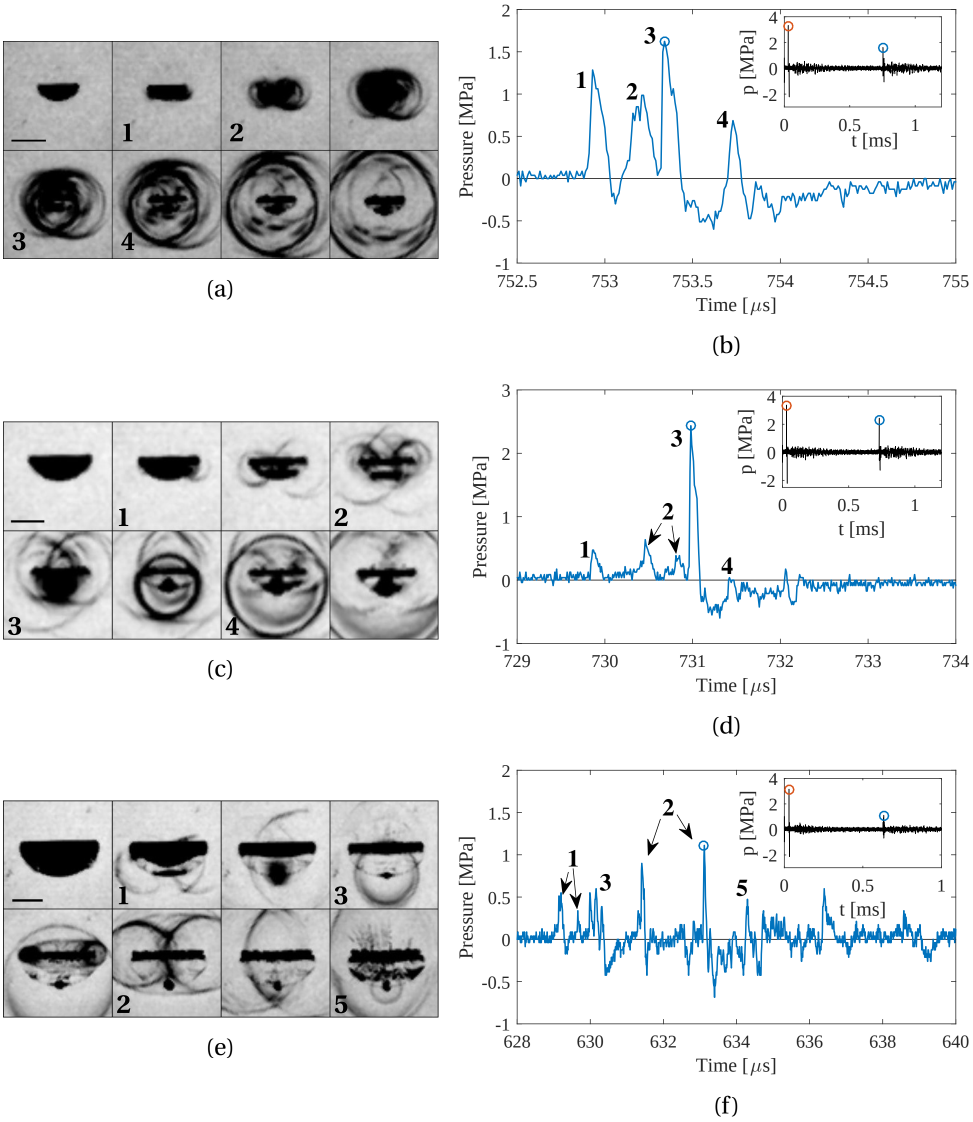

Figure 3.7: Caption on next page

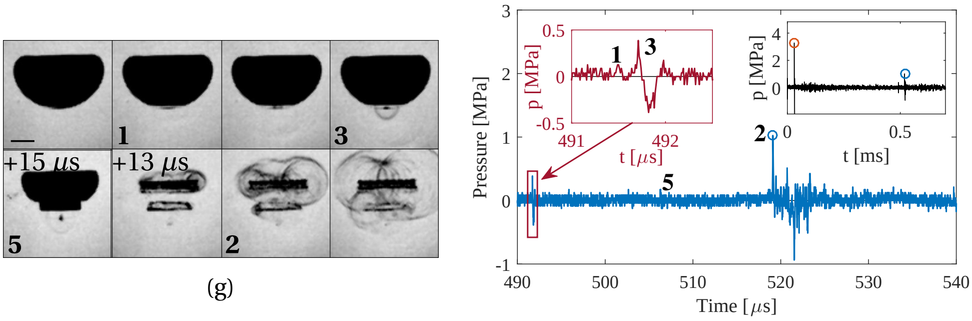

(g)

(h)

Figure 3.7: (Continued) Selected images (left) and hydrophone signal (right) for cavities of (a) and (b) $R_0 = 3.6$ mm at $\zeta = 2.9 \times 10^{-2}$ ($\gamma = 2.6$), (c) and (d) $R_0 = 3.6$ mm at 4.6×10^{-2} ($\gamma = 2.1$), (e) and (f) $R_0 = 3.2$ mm at $\zeta = 0.19$ ($\gamma = 1$), and (g) and (h) $R_0 = 3.0$ mm at $\zeta = 0.33$ ($\gamma = 0.77$) for an interframe time of (a) 200 ns, (c) 300 ns, (e) 600 ns, and (g) 400 ns unless otherwise indicated. The shock waves are denoted by 1, jet impac;, 2, torus collapse; 3, tip bubble collapse; 4, second torus collapse; and 5, second tip bubble collapse shock waves. The black bars show the 1-mm scale. The insets show the whole bubble oscillation, where the orange and blue circles refer to generation and collapse shock wave peak pressures, respectively. [See supplementary movies. For the bubble at $\zeta = 0.33$, the movie combines films made of two separate bubbles due to the long duration of the events and the limited number of frames captured by the camera. The events are highly repetitive.]

is considerable at $\zeta = 2.9 \times 10^{-2}$ but barely detected by the hydrophone at $\zeta = 4.6 \times 10^{-2}$. As can be seen in Figs. 3.7e and 3.7g, at a higher ζ the tip bubble collapse and the torus collapse change order. In Fig. 3.7g the tip bubble is very small and its collapse follows the jet impact so closely that it is difficult to distinguish the shocks they emit. At $\zeta = 0.19$ it is the torus collapse that triggers a second collapse of the tip bubble, while at $\zeta = 0.33$ the tip bubble is able to collapse naturally a second time long before the torus collapse. In Fig. 3.7g the compression of the toroidal bubble is highly nonuniform, yielding multiple peaks that generate a noisy hydrophone signal [Fig. 3.7h].

The shock wave strengths are also visible as the darkness levels of the corresponding image pixels owing to their ability to deflect light, which can be seen, for example, in Fig. 3.7c where the tip bubble shock wave is clearly the most pronounced of all the events. The time intervals between each event substantially increase with ζ. When the bubble collapses very close to the free surface, the hydrophone also detects the reflected rarefaction waves following closely the original shocks and contributing to the noise in the signal of Fig. 3.7h. These waves are visible in all movies of Fig. 3.7 and, due to their negative pressure resulting from the reflection at the free surface, they generate secondary cavitation in the bubble's neighborhood, as shown in Fig. 3.8. The secondary cavities are visible as clusters of microbubbles most prominently in the path of the focused laser, where the liquid is preheated and thereby the nucleation of cavities is facilitated, and between the bubble and the free surface [Fig. 3.8b]. Interestingly, some of these

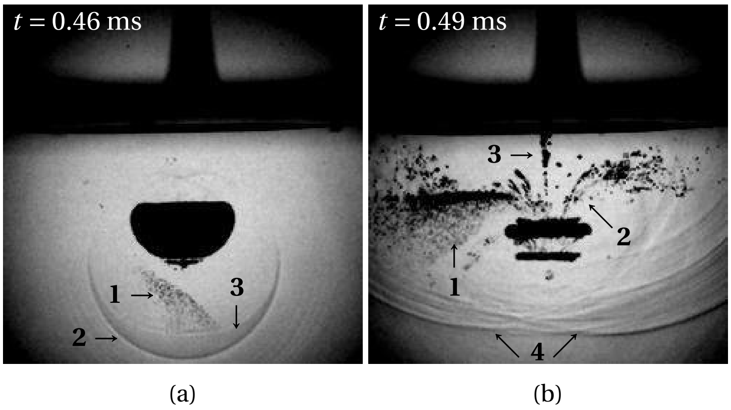

Figure 3.8: Visualization of secondary cavitation resulting from the passage of rarefaction waves for the same bubble as in Fig. 3.7g at two different instants: (a) secondary cavitation (1) below the bubble, generated by the tip bubble collapse shock wave, (2) turned into a rarefaction wave, and (3) after reflecting at the bubble's interface, and (b) secondary cavitation visible (1) in the pre-heated cone-shaped zone in the laser path, (2) as streamers along the microjet flow and (3) as a vertical column, and (4) generated by the rarefaction waves caused by the reflection of torus collapse shock waves at the free surface. (See supplementary movie.)

clusters, arranged in streamers towards the central axis of the toroidal bubble, delineate the flow induced by the formation of the microjet. The vertical column of microbubbles between the toroidal bubble and the free surface in Fig. 3.8b appears to result from the confluence of the rarefaction waves that are the reflections of the shocks initially emitted by the torus collapse. For the same bubble, secondary cavitation resulting from the shock emitted at the first tip bubble collapse is also observed below the bubble, right after the jet impact, as can be seen in Fig. 3.8a. Here the negative pressure results from the reflection at the bubble interface, and the rarefaction wave follows closely the original shock wave, which explains the significant tensile tail of the tip bubble collapse peak captured by the hydrophone in Fig. 3.7h.

3.3.3 Energy distribution and event timings

The observations of the distinct shock wave events and their corresponding pressures show important variations with different bubble asymmetries. The energy of the observed shock waves can be estimated from the hydrophone pressure signal via Eq. (3.2), where the integration range is selected by identifying the pressures associated with each individual event from the high-speed visualizations. It should be noted that this method assumes spherically symmetric propagation of the shock wave. Some shocks, especially the jet impact shock, might have some directionality, biasing their energy measurement. Indeed, it has been shown numerically that jet impact-induced shocks are dependent on the orientation with respect to the jet close to the bubble [79, 82]. However, the symmetric shock shadings seen in the high-speed visualizations far from the bubble center (not shown in figures) suggest that this directionality

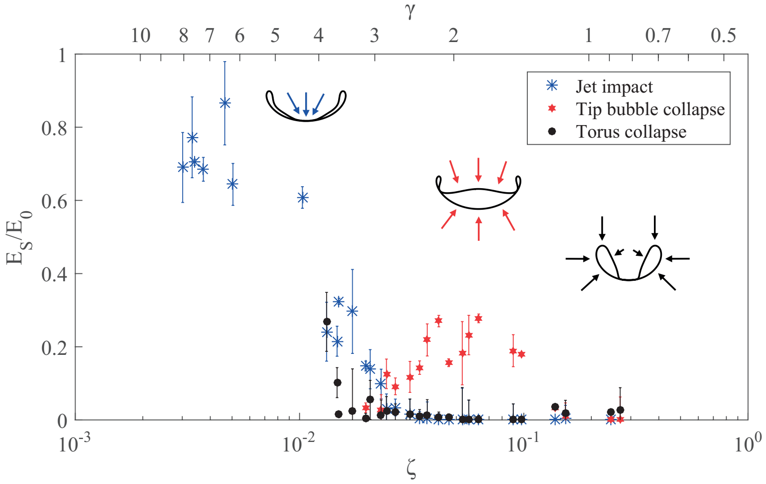

Figure 3.9: Normalized shock wave energy for each shock emission mechanism from bubbles deformed by a near free surface, as a function of ζ (and corresponding γ, top axis). Numerically calculated bubble shapes at jet impact are shown for $\zeta = 10^{-2}$, 6×10^{-2}, and 0.3.

must be subdominant. The shock pressure dependence on orientation likely reduces as the wave propagates and decreases in amplitude. We nonetheless caution that directionality is a potential source of systematic error, which might be reduced in future experiments by using multiple hydrophones in different directions.

The fraction of the bubble's initial energy E_0 distributed to the distinct shock waves for bubbles collapsing near a free surface is shown in Fig. 3.9 as a function of the anisotropy parameter ζ (and the equivalent γ). We only measured bubbles up to $\zeta \sim 0.3$ ($\gamma \sim 0.8$), beyond which the free surface resulted in severe perturbations in the hydrophone signal due to the reflected rarefaction waves. The driving pressure was kept at $\Delta p > 75$ kPa in order to avoid simultaneous deformations by the free surface and gravity, which could lead to more complex shapes at the bubble collapse (e.g., bubble splitting or annular jets [102]). The energy of each of the three main shock waves, i.e., jet impact, tip bubble collapse, and torus collapse, vary as functions of ζ. Interestingly, each of them dominates a certain range of ζ, as can be seen in Fig. 3.9. For bubbles that produce jets, the jet impact shock appears to dominate up to $\zeta \sim 2 \times 10^{-2}$. The tip bubble shock wave has a clear domination in the range $2 \times 10^{-2} < \zeta < 0.15$. Beyond $\zeta \sim 0.15$, the torus collapse shock wave is the most energetic, yet weak in relative terms with less than 10% of the initial bubble energy. The torus collapse energy is particularly low in the range $2 \times 10^{-2} < \zeta < 0.1$, coinciding with the domination of the tip bubble. The second torus collapse and the second tip bubble collapse emit shock waves with a negligible energy compared to the others, which is why they have been excluded from the figures.

The domination of the tip bubble in the range $2 \times 10^{-2} < \zeta < 0.15$ is explained through its large volume relative to the rest of the bubble at the moment of the jet impact, its spherical topology that allows an effective gas compression during its collapse, and/or the further compression

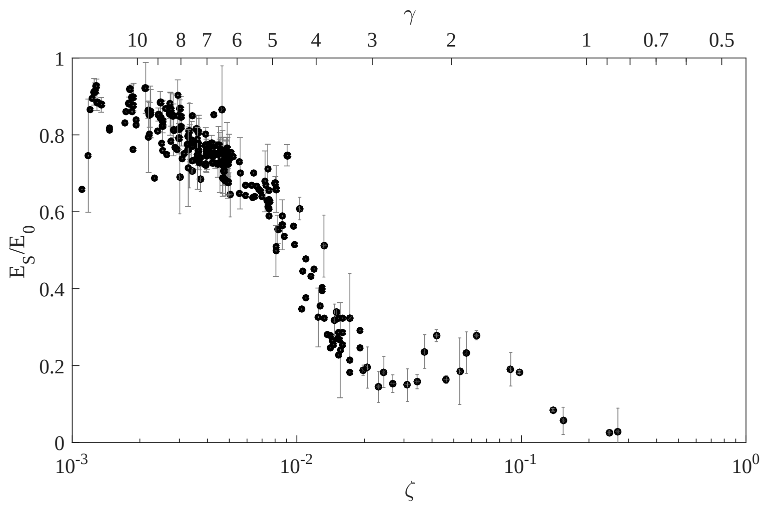

Figure 3.10: Normalized total collapse shock wave energy E_S/E_0 for bubbles deformed by a near free surface, as a function of ζ (and γ, top axis).

provided by the pushing jet. The large volume of the tip bubble and the small volume of the torus in this range result from the characteristic shape the jet assumes for bubbles collapsing near a free surface (see Fig. 3.5). Beyond $\zeta \sim 0.1$ however, the torus becomes relatively larger again at the moment of jet impact, as the bubble shape at $\zeta = 0.3$ in Fig. 3.9 suggests, and the torus is able to compress the gases it contains more effectively. This explains the slight rise of the torus collapse shock energy for $\zeta > 0.1$.

When the energies of the different collapse shock waves are summed, an overall decrease of the total shock energy is observed, as can be seen in Fig. 3.10. Here data for lower ζ have been added, including energies from pressure measurements for which it was not possible to distinguish the different shock wave events. Interestingly, the total shock energy varies as a function of ζ independently of the bubble maximum radius and driving pressure within the ranges covered here (R_0 = 1–4 mm and Δp = 0.75–1 bar). A major part of the collapse shock energy decrease occurs within the range $10^{-3} < \zeta < 2 \times 10^{-2}$, where the jet impact hammer shock is expected to dominate. As the bubble deforms, the liquid inflow towards the bubble center becomes anisotropic and as a result, the level of compression of the bubble's enclosed gases reduces yielding weaker shock wave emission. As less energy is radiated away by the shock waves for increasing ζ, more energy is distributed to the motion of the liquid forming the micro-jet and to the rebound bubble, both of which are observed to grow with ζ.

The timing of the distinct events in the shock wave scenario also appears to vary with the level of deformation of the bubble. Figure 3.11 displays the time difference ΔT between the jet impact, which generally emits the first shock wave, and the other observed events, normalized to the bubble collapse time T_c. The experiments are displayed together with our previously established model estimating the normalized time between the jet impact and

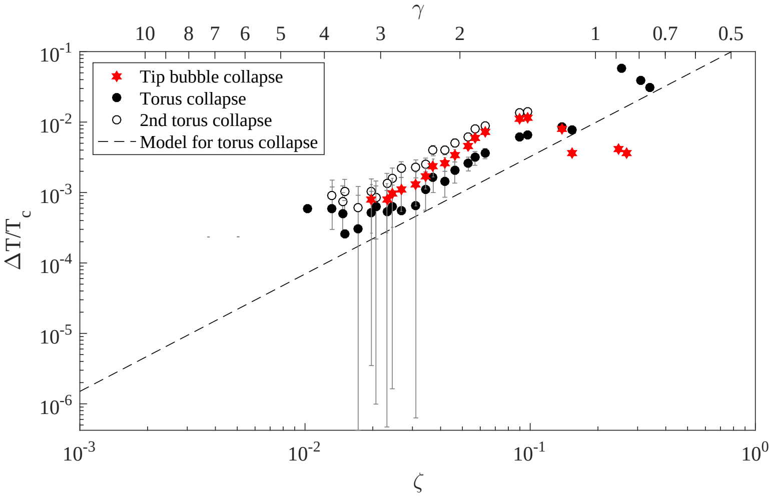

Figure 3.11: Time differences between the jet impact and the tip bubble collapse, torus collapse and the second torus collapse as a function of ζ (and γ, top axis), normalized with bubble collapse time T_c. The time between jet impact and torus collapse is modeled as $\Delta T/T_c = 0.15\zeta^{5/3}$ [143].

torus collapse $\Delta T/T_c = 0.15\zeta^{5/3}$ [143]. Only data for $\zeta > 10^{-2}$ are displayed as the temporal resolution of our apparatus is not sufficient for identifying the exact shock timings of more spherical bubbles. The jet impact occurs within the last 1% of the bubble's collapse time up to $\zeta \approx 0.2$, followed very closely by the other events. The torus collapse precedes the tip bubble collapse up to $\zeta \approx 0.14$, beyond which they change order. The second torus collapse occurs right after the tip bubble collapse up to this limit, as the rebounding torus compresses under the effect of the shock wave produced by the latter, which is seen as an almost constant time difference between the two events in Fig. 3.11. The normalized timings of each shock wave are independent of the maximum bubble radii and driving pressures covered here.

3.4 Models for shock energy and pressure

We now investigate shock waves from nonspherically collapsing bubbles at a more general level with the aim of developing a semiempirical model to predict their strengths. For this purpose, we look at shock waves from bubbles deformed by different sources, in particular by the gravity-induced uniform pressure gradient. Examples of measured shock waves from bubbles deformed by gravity are shown in Fig. 3.12. A spherical collapse [Fig. 3.12(a)] produces a single shock, as observed previously in Sec. 3.3.1. Nonspherical collapses [Figs. 3.12(b) and 3.12(c)] generate multiple shocks and the associated peak pressures clearly decrease with increasing bubble deformation, similarly to bubbles deformed by a free surface. However, the characteristic shape of bubbles collapsing in uniform pressure gradients is such that the radii of curvature of the jet tip and the opposite bubble wall at their impact are very similar for a wide range of ζ according to potential flow theory [143], as illustrated in Fig. 3.13 for $\zeta = 10^{-2}$.

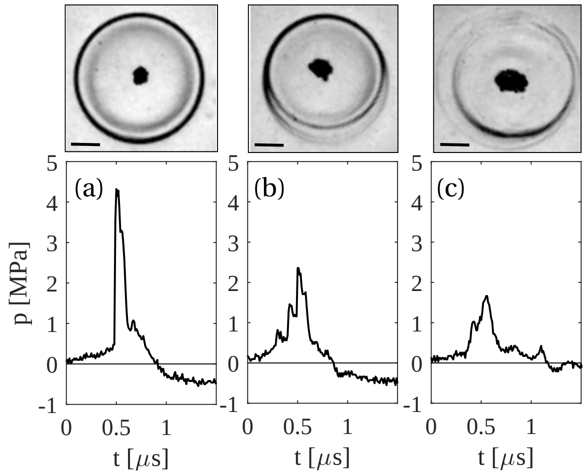

Figure 3.12: Examples of hydrophone pressure signals of shock waves measured at the collapse of bubbles deformed by gravity at (a) $\zeta < 10^{-3}$, (b) $\zeta = 3.8 \times 10^{-3}$, and (c) $\zeta = 10^{-2}$. The corresponding shadowgraph images with an exposure of 50 ns are shown on top. The black bars show the 1-mm scale.

As a consequence, the volumes of the tip bubble and the toroidal bubble remain relatively small and the associated shocks are barely distinguishable. We therefore analyze the collapse shock as one event, expected to be dominated by the jet impact (as suggested by Fig. 3.9 for bubbles near a free surface at $\zeta < 10^{-2}$), without resolving its substructure in the following analyses.

We first consider the variation of the peak pressures $p_{\max}$ measured by the hydrophone as a function of ζ. Figure 3.14 shows this function for bubbles deformed by the gravity-induced pressure gradient (varied parameters R_0 = 1.5–10 mm, Δp = 6–98 kPa, at normal gravity). Clearly, the relation between $p_{\max}$ and ζ depends on Δp. We can build a model for the relationship between $p_{\max}$, Δp, and ζ, based on the simplistic assumptions of scale-free microjets and shocks resulting from a water hammer pressure caused by the jet impact [136, 79]:

$$p_h = \frac{1}{2}\rho c U_{\text{jet}} = 0.45\left(\rho c^2 \Delta p\right)^{1/2} \zeta^{-1} \tag{3.4}$$

where U_{jet} is the microjet speed at its impact on the opposite bubble wall. The scaling model for the microjet speed $U_{\text{jet}} = 0.9\left(\Delta p/\rho\right)^{1/2}\zeta^{-1}$ has previously been established by combining numerical simulations and analytical arguments with experimental observations and is a valid approximation for jets driven by gravity and near surfaces at $\zeta < 0.1$ [143]. We can therefore expect also the resulting hammer pressures to be similar for these different sources of bubble deformation and to decrease with ζ for a given Δp (with constant ρ and c). The scaling factor in Eq. (3.4) could be different if the jet impact is not the dominant shock mechanism, but this is irrelevant in the following derivation because of the free parameter α discussed hereafter.

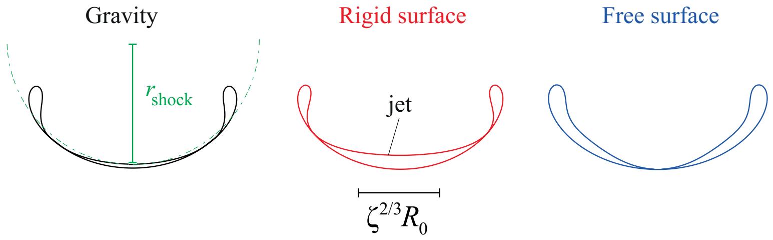

Figure 3.13: Bubble shapes at jet impact for bubbles deformed by a uniform pressure gradient, a near rigid surface, and a near free surface, predicted by potential flow theory [143] for $\zeta = 10^{-2}$. Here $\boldsymbol{\zeta}$ is directed downward.

The equivalent observational proxy for p_h is expressed as

$$p_h = p_{\max}\left(\frac{d}{r_{\text{shock}}}\right)^{\beta} = \alpha\, p_{\max}\left(\frac{d}{R_0}\right)^{\beta}\zeta^{-2\beta/3}, \tag{3.5}$$

where $p_{\max}$ is the peak pressure measured by the hydrophone, d is the distance between the bubble center and the hydrophone sensor, r_{shock} is the shock emitting radius, assumed to scale as the radius of the jet tip (see schematic in Fig. 3.13) and thereby as the bubble's characteristic length at jet impact $s \propto \zeta^{2/3}R_0$ as predicted by potential flow theory for $\zeta \ll 1$ [143], and α and β are free parameters. Here α represents the unknown scaling of $r_{\text{shock}} \propto \zeta^{2/3}R_0$. In addition, β would equal 1 for negligible shock dissipation and spreading of the shock width, yet in reality nonlinearities are present and result in a higher exponent, typically about 2 in the near field and ~ 1.1 in the far field of the emission center [151, 152, 144, 40]. Equating Eqs. (3.4) and (3.5) gives

$$p_{\max} = \frac{0.45}{\alpha}\left(\rho c^2 \Delta p\right)^{1/2}\left(\frac{R_0}{d}\right)^{\beta}\zeta^{2\beta/3-1}. \tag{3.6}$$

We fit α and β simultaneously to a sample of 931 bubbles deformed by gravity to minimize the χ^2 deviation between the left- and right-hand sides of Eq. (3.6) [3]. The resulting fitted parameters are $\alpha = 0.277 \pm 0.006$ and $\beta = 1.249 \pm 0.003$ and the corresponding determination coefficient is $R^2 = 0.93$. As expected, β lies between 1 and 2. In the case of bubbles deformed by gravity, there is a unique relation between R_0, Δp, and ζ as shown by Eq. (3.1). Substituting R_0 from this relation into Eq. (3.6) makes $p_{\max}$ a function of only Δp and ζ. These relations are plotted as dashed lines in Fig. 3.14 and show excellent agreement with the measurements.

The lines in Fig. 3.14 can be collapsed to a single relationship by plotting the measured peak pressures $p_{\max}$ directly against the model in Eq. (3.6), which is shown in Fig. 3.15. We now also apply this simple model to predict the shock pressures of nonspherical bubbles with different sources of deformation (free and rigid surfaces), where the unique relationship between R_0, Δp, and ζ no longer holds because of the additional dependence on the distance h to the surface, as shown by Eq. (3.1). These data also coincide with the model, as can be seen in

---

[3] A fit with the exponent of $\rho c^2 \Delta p$ as a free parameter was also performed, which consistently gave 0.506 ± 0.006.

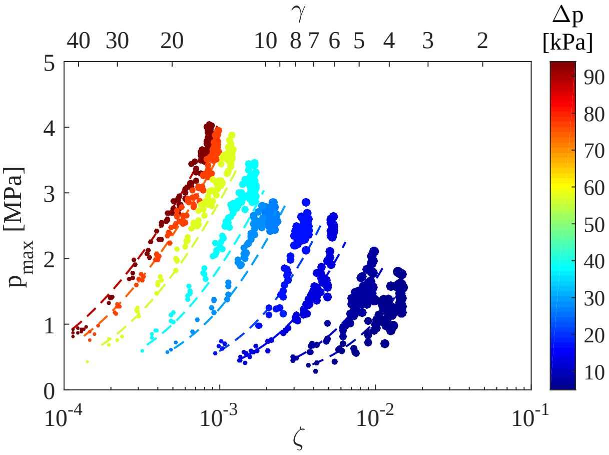

Figure 3.14: Measured shock peak pressures as a function of ζ (and γ, top axis) for bubbles deformed by gravity. The dashed lines represent the model in Eq. (3.6). The colors indicate different driving pressures Δp. The symbol sizes portray the different maximum bubble radii.

Fig. 3.15, confirming that the hammer pressure model can be used to estimate shock pressures produced by a nonsspherical bubble collapse. The pressures p_h at the source, estimated using Eqs. (3.4) and (3.5), range from 100 MPa to 10 GPa at $\zeta > 10^{-3}$.

Figure 3.16 displays the normalized collapse shock wave energy for bubbles deformed by gravity, a nearby rigid surface, and a free surface as a function of ζ. All the measured shock energies generally decrease with increasing ζ independently of R_0 and Δp. For gravity-deformed bubbles, most of the decrease happens in the range $10^{-3} < \zeta < 10^{-2}$, reaching values down to about 10% of initial bubble energy E_0 at $\zeta \sim 10^{-2}$. These values differ significantly from bubbles deformed by a rigid and a free surface that respectively have shock energies as high as 30% and 40% of the initial bubble energy E_0 at $\zeta \sim 10^{-2}$ ($\gamma \sim 4.4$). Shocks from bubbles deformed by a near rigid and a free surface experience a decrease in energy with ζ that is similar to the gravity-deformed cases, but which occurs at a higher ζ.

It should be noted that the expression of ζ for gravity-induced bubble deformations [Eq. (3.1)] includes Δp, making Δp correlate with ζ in our data obtained on ground (see the gray scale in Fig. 3.16). However, the data in microgravity ($0\pm0.02\,g$), which were obtained aboard European Space Agency parabolic flights, confirm that the bubble deformation is the main cause of the observed shock energy variations, rather than Δp. For example, bubbles collapsing at $\Delta p \approx 20$ kPa in our experiment on ground emit low-energy shocks ($E_S/E_0 < 30\%$), yet in microgravity at the same driving pressure $E_S/E_0 > 75\%$ [4]. Some data for bubbles collapsing at higher gravity levels ($1.66 \pm 0.093g$) are also displayed in Fig. 3.16, showing reasonable agreement with the general shock energy trend with ζ.

---

[4] The presence of the closest surface to the bubble, i.e. the parabolic mirror, is accounted for when determining ζ for bubbles collapsing in micro-gravity.

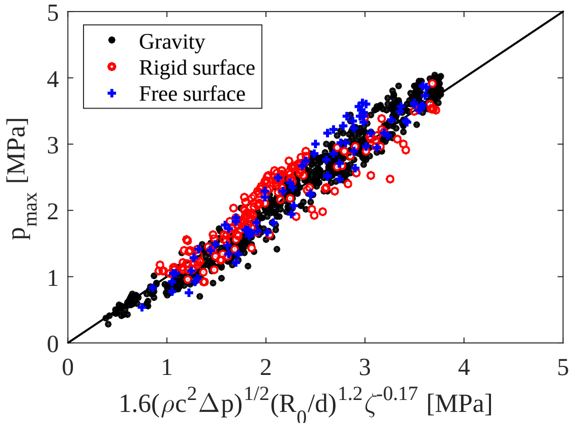

Figure 3.15: Measured shock wave peak pressures as a function of the model given in Eq. (3.6) for bubbles deformed by gravity, a rigid surface, and a free surface.

Since the measured peak pressures for deformed bubbles are well approximated with the hammer pressure model, we aim at estimating their shock energies using the same approach. We recall that the shock energy $E_S = (4\pi d^2\rho^{-1}c^{-1})\int p^2 \mathrm{d}t$ from Ref. [94], as for Eq. (3.2). If the pressure profile in time is represented with a hammer pressure p_h being applied for a time $\Delta t = \Delta d c^{-1}$, where Δd denotes the thickness of the shock, the energy reads $E_S = (4\pi d^2\rho^{-1}c^{-1})p_h^2\Delta t$. The shock wave energy is therefore alternatively expressed as

$$E_S = \frac{\Delta V p_h^2}{\rho c^2}, \tag{3.7}$$

where $\Delta V = 4\pi d^2\Delta d$ is the volume of the compressed liquid. As mentioned before, the characteristic length of the bubble at the jet impact scales as $s/R_0 \propto \zeta^{2/3}$. As the surface area of contact of the jet onto the opposite bubble wall is two dimensional and the compressed liquid volume is assumed to be proportional to that area, we have $\Delta V/R_0^3 \propto s^2/R_0^2 \propto \zeta^{4/3}$. With this model plugged into Eq. (3.7) and p_h substituted for Eq. (3.4), we obtain

$$\frac{E_S}{E_0} \propto \frac{\Delta V}{R_0^3\zeta^2} \propto \zeta^{-2/3}. \tag{3.8}$$

The missing scaling factor for Eq. (3.8) comes from the unknown size of the compressed liquid region. An analytical evaluation of this unknown is difficult and would have to account for the nonuniform liquid compression by the curved jet tip. The scaling factor is expected to vary for the distinct sources of deformations, since the jet shapes are different for each case and leave gas or vapor pockets of dissimilar sizes between the jet and the opposite bubble wall, as illustrated in Fig. 3.13 for $\zeta = 10^{-2}$. These vapor pockets are rather large for bubbles collapsing near a rigid or a free surface, while gravity-induced jets hit the opposite bubble wall in a highly uniform way, thereby resulting in the smallest scaling factor. When minimizing the χ^2 deviation between the measurements E_S/E_0 for bubbles deformed by gravity at $\zeta > 10^{-3}$

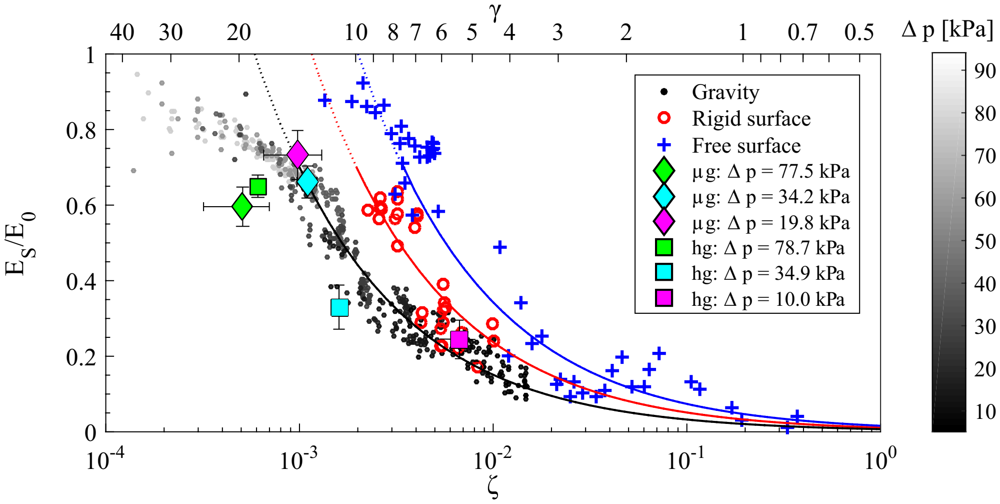

Figure 3.16: Normalized total collapse shock wave energy for bubbles deformed by gravity, a near rigid surface, and a near free surface as a function of ζ (and γ, top axis). Averaged shock energies measured in microgravity (μg) ($0 \pm 0.02g$) and hypergravity (hg) ($1.66 \pm 0.093g$) at three different Δp are also displayed. The gray-scale indicates different driving pressures Δp for bubbles deformed by gravity. The models in solid lines show the fits $0.0073\zeta^{-2/3}$, $0.011\zeta^{-2/3}$, and $0.016\zeta^{-2/3}$ for bubbles deformed by gravity, a rigid surface, and a free surface, respectively. The mean error of E_S/E_0 is 0.04.

and a model in the form $f = a\zeta^b$ with free parameters a and b, we find $a = 0.0078$ and $b = -0.66$. When imposing $b = -2/3$ to conform with Eq. (3.8), the best fit for a is 0.0073. The corresponding fitted scaling factors for the rigid and free surfaces are $a = 0.011$ and 0.016, respectively. Equation (3.8) with these fitted scaling factors is plotted as solid lines for bubbles deformed by gravity, a free surface, and a rigid surface in Fig. 3.16 and agrees reasonably well with the experimental data.

3.5 Discussion

There are several limitations in the presented shock models worth addressing. The microjet is expected to reach the speed of sound for a bubble collapsing at $\zeta \lesssim 0.9(\Delta p/\rho)^{1/2}c^{-1}$ ($\zeta \lesssim 0.006$ at $\Delta p = 98$ kPa), below which the model in Eq. (3.4) may no longer be able to estimate the jet hammer pressures. Furthermore, our model neglects the gas inside the bubble. Compressed and heated gases within highly spherically collapsing bubbles can potentially slow down and destroy the jet and/or delay or prevent its formation. These effects naturally decrease with increasing ζ, since at higher ζ the jet forms earlier in the bubble evolution, when the gases are less compressed. We estimate the bubble gas to seriously hamper the jet for $\zeta < 10^{-3}$, where no observable jets are formed in the bubble rebound in our current setup [143]. This is the likely explanation for the sudden curvature change in the shock energy trend for bubbles deformed by gravity at $\zeta \sim 10^{-3}$, as can be seen in Fig. 3.16. Below this approximate threshold (at which $p_h \sim 7$ GPa for bubbles collapsing here at atmospheric pressure), the shock pressures predicted by the model are overestimated. This threshold value is consistent with previous findings for a spherical collapse at atmospheric pressure, both in our setup (Sec. 3.3.1) and in the literature [40, 41, 39].

The shock energies of bubbles collapsing near a rigid surface show important differences when compared with the measurements performed by Vogel and Lauterborn [94]. Although they observed, similarly to us with bubbles near a free surface, a clear minimum in shock energies at $\gamma = 1$, they also measured shocks beyond $\gamma \sim 3$ to have the same energies as those emitted in a spherical collapse, while at $\gamma = 3$ we measure barely 20% of a typical shock energy from a spherical collapse. This suggests that the experimental conditions play an important role in the collapse shock wave characteristics, including the initial bubble sphericity, which highly differs for parabolic mirror- and lens-based laser focusing methods. Indeed, in Vogel and Lauterborn's study the standoff was varied only up to $\gamma \sim 3$, beyond which a spherical collapse was assumed, while we still find important shock energy variations between $\gamma \sim 5$ and 10.

3.6 Conclusion

We have presented detailed observations of shock wave emissions from the collapse of bubbles with various levels of deformation, quantified by the anisotropy parameter ζ, using simultaneous time-resolved shadowgraphy and needle hydrophone pressure measurements. A gradual pressure rise in the liquid near the bubble wall was observed in the last collapse stage of nearly spherically collapsing bubbles, in agreement with the century-old predictions of Lord Rayleigh. Nonspherical bubble collapses produced multiple shock waves associated with different processes such as the jet impact and the individual collapses of the various separated parts of the bubble. When quantifying these distinct shocks for bubbles collapsing near a free surface, the jet impact shock was found to dominate up to $\zeta \sim 2 \times 10^{-2}$, the bubble tip collapse in the range $2 \times 10^{-2} < \zeta < 0.15$, and the torus collapse at $\zeta > 0.15$. The timings of the individual events, normalized with the bubble collapse time, were also found to vary with ζ.

Models predicting the shock peak pressure and energy were proposed based on the assumption that the shock wave is generated by a jet impact hammer pressure. The pressure model showed excellent agreement with the observed data in the range $10^{-3} < \zeta < 10^{-2}$ for all three sources of bubble deformation used here (gravity, rigid surface, and free surface) and the energy model captured the approximative trend of the measured energies. The total collapse shock wave energy, normalized to the total bubble energy, generally decreased with increasing ζ. However, we found differences between the shock energies from bubbles deformed by different sources, which likely result from the small variations in the jet shapes at their impact onto the opposite bubble wall. Interestingly, these differences do not seem to affect the shock peak pressures, which could be due to the jet speed at the moment of impact (which the hammer pressure is proportional to) being nearly identical for the three sources of bubble deformation at this range of ζ.

4 Luminescence

Luminescence from cavitation bubbles deformed in uniform pressure gradients

Reproduced version of

Outi Supponen, Danail Obreschkow, Philippe Kobel and Mohamed Farhat. *Luminescence from cavitation bubbles deformed in uniform pressure gradients.* Physical Review E **96**(3) 033114 (2017). DOI: 10.1103/PhysRevE.96.033114,

with the permission of American Physical Society.

The author's contribution:
The author designed the luminescence detection system and re-built the experimental setup to meet the requirements imposed by the parabolic flights. She coordinated the team for the 62nd ESA parabolic flight campaign and the 1st Swiss parabolic flight in 2015. She made the experiments and the analysis with the help of the co-authors. She was the first author of this publication.

Abstract

Presented here are observations that demonstrate how the deformation of millimetric cavitation bubbles by a uniform pressure gradient quenches single-collapse luminescence. Our innovative measurement system captures a broad luminescence spectrum (wavelength range, 300–900 nm) from the individual collapses of laser-induced bubbles in water. By varying the bubble size, driving pressure, and perceived gravity level aboard parabolic flights, we probed the limit from aspherical to highly spherical bubble collapses. Luminescence was detected for bubbles of maximum radii within the previously uncovered range, R_0 = 1.5–6 mm, for laser-induced bubbles. The relative luminescence energy was found to rapidly decrease as a function of the bubble asymmetry quantified by the anisotropy parameter ζ, which is the dimensionless equivalent of the Kelvin impulse. As established previously, ζ also dictates the characteristic parameters of bubble-driven microjets. The threshold of ζ beyond which no luminescence is observed in our experiment closely coincides with the threshold where the

microjets visibly pierce the bubble and drive a vapor jet during the rebound. The individual fitted blackbody temperatures range between T_{lum} = 7000 and T_{lum} = 11500 K but do not show any clear trend as a function of ζ. Time-resolved measurements using a high-speed photodetector disclose multiple luminescence events at each bubble collapse. The averaged full width at half-maximum of the pulse is found to scale with R_0 and to range between 10 and 20 ns.

4.1 Introduction

As a cavitation bubble undergoes a spherical collapse, it compresses its enclosed gaseous contents and - presumably - adiabatically heats them to temperatures of several thousands of degrees, which results in light emission called luminescence [43]. The drive to investigate luminescence comes from the intense energy focusing at a bubble collapse, which provides a catalytic host for unique chemical reactions [153, 154], offering potential for cancer therapy [21, 20], environmental remediation [33, 155], and fabrication of nanomaterials [34, 156]. While most past studies have researched sonoluminescence, that is, luminescence from acoustically driven bubbles, light emission has also been detected from hydrodynamic cavitation in engineering flows [157, 158].

Due to the occurrence at the last instant of the collapse, the redistribution of the bubble's energy into luminescence, as well as shock waves, microjets, and elastic rebounds (see introduction in Ref. [97]), must be highly sensitive to topological changes in the cavity volume during the final collapse stage. This represents an important feature, considering that any anisotropy in the pressure field of the surrounding liquid will result in the deformation of an initially spherical bubble, inducing a microjet that pierces the bubble and therefore causes it to undergo a toroidal collapse [122, 143]. The level of compression of the bubble gases is reduced for even slight bubble deformations, manifested in the weakening of the collapse shock-wave emissions [94, 159]. Indeed, luminescence has been shown to vary with the proximity of near surfaces that break the spherical symmetry of the bubble [123, 160, 161]. It has also been shown that the lack of buoyancy enhances the energy concentration at the final stage of bubble collapse [91], even for bubbles that are highly spherical and generally assumed not to be subject to deformation by gravity (maximum bubble radius, $R_0 \sim 40$ μm at atmospheric pressure). Bubbles collapsing with pronounced microjets in multibubble fields have been shown to emit less light (or none) compared to spherically collapsing bubbles [162].

Spectral analyses of luminescence have proposed a wide range of temperatures at a bubble collapse in water, depending on whether the bubble is trapped in an oscillating acoustic field (bubble temperatures $T > 10^4$ K) [43], induced by a laser pulse ($T \sim$ 7000–8000 K) [163, 104], induced by a spark ($T \sim$ 6700 K) [164], or within a bubble cloud ($T <$ 5000 K) [165, 153]. Recent studies reached 1.4×10^4 K for an energetic bubble collapse provoked by piezoelectric tranducers [166] and over 2×10^4 K for a centimetric bubble expanded by a chemical reaction in a free-fall tower [167]. Moreover, luminescence spectra from small bubbles (maximum radius

$R_0 < 1$ mm) show a smooth continuum similar to a blackbody, while spectra of luminescence from large, laser-induced bubbles ($R_0 > 1$ mm) and multibubble sonoluminescence have shown emission lines of excited hydroxyl (OH^-) bands at 310 nm [168, 161] that have been associated with aspherical bubble collapses. It is unclear, however, to what extent the spectral differences in these distinct scenarios are caused by physical or experimental factors, and a systematic picture of the role of pressure-field anisotropies - and the resulting bubble deformation - on luminescence is still lacking.

This work presents observations on the luminescence of initially highly spherical, millimetric bubbles collapsing at different levels of deformation caused by the gravity-induced uniform pressure gradient. We probe the transition from toroidal jetting bubbles in controlled pressure gradients to highly spherical bubbles in microgravity and cover a broad parameter space. Spectral and time-resolved measurements are made on single-cavitation-bubble luminescence from individual collapses of transient, laser-induced vapor bubbles in water, contrasting with the established single-bubble sonoluminecence, which is normally understood as the time-averaged light emitted by an oscillating bubble trapped in an acoustic field. It also differs from the averaged single-cavitation-bubble luminescence, from luminescence of gas bubbles, and from luminescence of bubbles in liquids doped with noble gas.

4.2 Experimental setup

Figure 4.1 shows a schematic of our experiment. We generate highly spherical bubbles by using an immersed parabolic mirror to focus a Q-switched Nd:YAG laser (532 nm, 8 ns) in the middle of a cubic test chamber filled with demineralized water. The water is initially partially degassed to remove large bubbles from the container boundaries, but we presume the water to be mostly air saturated. The bubbles are so spherical that the dominant pressure-field anisotropy deforming the bubble is the gravity-induced pressure gradient [97]. Furthermore, owing to their high sphericity, these bubbles do not suffer a fission instability, i.e., bubble splitting [106, 104], during their collapse, allowing very large bubbles to compress their enclosed gases efficiently and luminesce in the absence of external perturbations. We obtain the bubble's maximum radius R_0 by measuring its collapse time T_c (i.e., half oscillation time) of the bubble with a needle hydrophone, which detects the passage of the shock waves emitted at the generation and the collapse of the bubble. The maximum bubble radius is then obtained via $R_0 = 1.093 T_c (\Delta p/\rho)^{1/2}$ [51], where $\Delta p = p_0 - p_v$ is the driving pressure (p_0 being the static pressure at the height of the bubble and p_v the liquid vapor pressure) and ρ is the liquid density. It is considered unnecessary to correct this relation for the bubble's asphericity, as the deformations in this work remain weak. The temperature of the water is recorded with a thermistor and kept at room temperature (294.2±1 K), and p_v is computed for each bubble individually using the Antoine equation. Simultaneous visualizations of the luminescence, radial evolution of the bubble, and shock-wave emission are made with an ultrahigh-speed CMOS camera (Shimadzu HPV-X2) filming at 10×10^6 frames/s (fps) with an exposure time of 50±10 ns and a back-light LED.

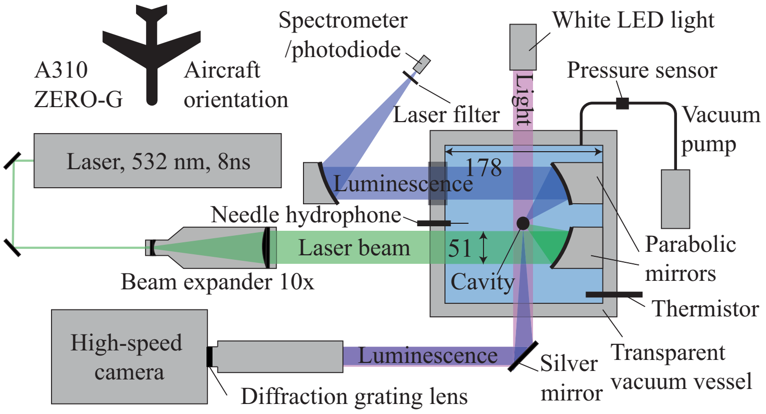
A310
ZERO-G
Aircraft
orientation
Spectrometer
/photodiode
Laser filter
White LED light
Light
Pressure sensor
Vacuum
pump
Laser, 532 nm, 8ns
Luminescence
178
Needle hydrophone
Laser beam
51
Cavity
Parabolic
mirrors
Thermistor
Beam expander 10x
High-speed
camera
Luminescence
Silver
mirror
Transparent
vacuum vessel
Diffraction grating lens

Figure 4.1: Schematic top view of the experimental setup. Dimensions are given in millimeters.

The time-averaged luminescence spectrum from a single bubble collapse is captured in the dark by a spectrometer (Ocean Optics QEPro; exposure time, 8 ms). The light emitted during the bubble collapse is collected using a second, aluminum-coated, immersed parabolic mirror that reflects it through a fused silica window (for UV transparency) onto another parabolic mirror outside the test chamber. We chose aluminum-coated mirrors for their good UV reflection quality. The external mirror focuses the light through a laser-blocking filter onto the entrance of the optical fiber that leads to the spectrometer. Without the filter the laser would saturate the measured spectrum despite the spectrometer's being triggered only after the bubble generation.

The luminescence spectrum is simultaneously measured with a second high-speed camera (Photron SA1.1) that has a CCD sensor (in place of the CMOS camera). It is equipped with an astronomy-quality diffraction grating lens (RSpec, Star Analyzer SA-100) and films at 10^5 fps with an exposure time of 10 μs. The reason for using the CCD instead of the CMOS camera to measure the spectrum is that it guarantees the luminescence to be fully contained in its exposure time, which the latter cannot. The grating lens, placed between the camera objective and the CCD sensor, splits and deviates the light one or more diffraction orders located in a plane perpendicular to the grating lines, thus providing a spectrum on the sensor. A schematic of the CCD light detection system is shown in Fig. 4.2 along with a typical measured luminescence signal. The reasons behind measuring the spectrum additionally with the camera are that it fills in the spectral gap in the spectrometer ($\sim$ 500–700 nm) caused by the laser-blocking filter and, more importantly, corrects the intensity of the spectrum recorded by the spectrometer, which is affected by the bubble's migration away from the parabolic mirror's focal point. The bubble's displacement becomes important, in particular, at higher gravity levels for large bubbles that experience a strong Kelvin impulse [143] (i.e., the integrated momentum of the liquid during the growth and the collapse of the bubble [68]). This displacement can weaken the signal measured with the spectrometer, and therefore it is corrected using the spectrum recorded by the CCD. The CCD spectrum measurement is unaffected by the bubble's displacement, as the luminescence spot stays within the image plane.

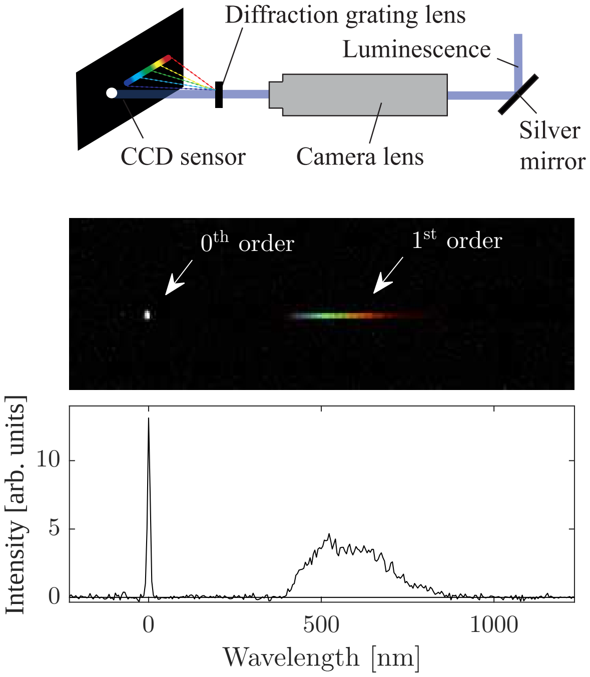

Figure 4.2: Top: Schematic of the CCD luminescence detection system coupled with a diffraction grating lens. Middle: Typical luminescence signal (zeroth- and first-order spectra) as recorded by the CCD sensor. Bottom: Corresponding raw spectrum obtained from the pixel intensities of the image.

The optical path from the luminescence to the spectrometer includes 194 mm water, 6 mm fused silica, two aluminum-coated parabolic mirrors and the laser filter. To reach the camera's CCD sensor, the luminescent light travels through water, acrylic glass, a silver mirror, the camera lens and the grating lens. The wavelength-dependent transmissions of the various elements in the optical paths are shown in Fig. 4.3. The calibration of the spectrometer detector and the absorption and transmission spectra of the various optical components were provided by their respective manufacturers. Water's absorption spectrum in the wavelength range of interest is found in the literature [169]. The spectrum measured by the high-speed camera with the grating filter was calibrated in-house combining the transfer functions of the camera and the optical path using a thermal light source placed inside the test chamber at the location where the bubble was generated. This innovative luminescence measurement system allows for (i) the collection of a substantial amount of light from the rapid, small, and weak luminescence of a single bubble collapse, (ii) the capture of a wide spectrum from a single bubble collapse, including the UV, and (iii) staying far from the bubble so as not to disturb its dynamics.

Time-resolved measurements of the luminescence pulse are made using the same optical path as described above for the spectrometer, but by focusing the light onto a high-speed photodetector (Thorlabs, DET10A/M Si detector) without a laser-blocking filter. The detector

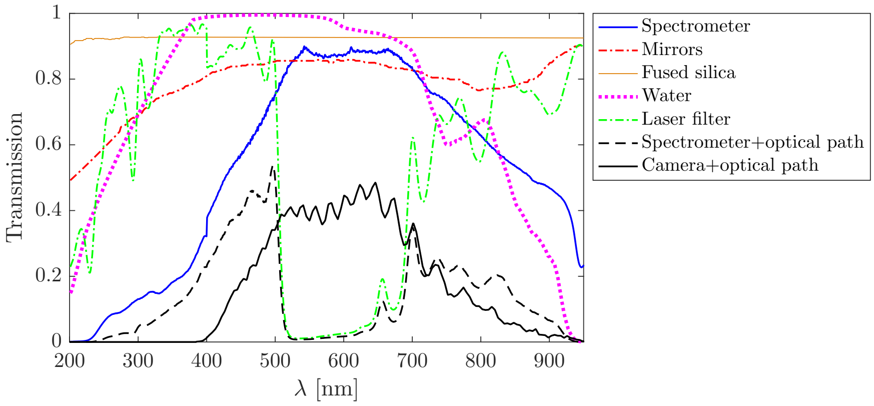

Figure 4.3: Transmission of light as a function of the wavelength λ for the various elements on the optical path from the luminescence emission point to the detectors.

has a 1-ns rise time and is sensitive in the 200- to 1100-nm wavelength range. The photodetector signal is recorded by an oscilloscope (4-GHz bandwidth), which is triggered using the hydrophone signal of the collapse shock wave and applying a 25-μs negative delay to account for the shock-wave propagation over a distance of ~37 mm to reach the hydrophone after the bubble collapse.

Three parameters influencing the bubble luminescence can be independently varied in our experiment: (i) the driving pressure, $\Delta p \equiv p_0 - p_v$ (0.06–1 bar), where p_0 is adjusted using a vacuum pump; (ii) the bubble energy, $E_0 = (4\pi/3)R_0^3\Delta p$ (0.4–28 mJ), adjusted by the laser pulse energy; and (iii) the constant, uniform pressure gradient, ∇p (=$\rho\mathbf{g}$, with the perceived gravitational acceleration $|\mathbf{g}|$ varied between 0 and 2 g, where $g = 9.81$ ms^{-2}), modulated aboard European Space Agency parabolic flights (the 58th, 60th, and 62nd parabolic flight campaigns) and on the first Swiss parabolic flight. The interest in using the hydrostatic pressure gradient to deform bubbles is based on its uniformity in space and time, in contrast to near boundaries. This is an advantage in particular as it probes the influence of pressure gradients induced by any other inertial forces in addition to gravity. Moreover, any practical instance of a smooth pressure field can be approximated to first order by such a uniform pressure gradient, thus extending the scope of this study to any situation involving bubbles in anisotropic pressure fields [46, 143]. These variables yield a wide range of maximum bubble radii, $R_0 \sim 1.5$–10 mm. Such large bubbles present the advantage of easier resolution of the time and space scales associated with their collapse, in contrast to, e.g., single-bubble sonoluminescence experiments. Additional details on the experiment and the parabolic flights may be found in Ref. [97].

We account for the effect of bubble asphericity due to the gravity-induced pressure gradient through the anisotropy parameter $\zeta \equiv |\nabla p| R_0 \Delta p^{-1}$, which is the dimensionless equivalent of the Kelvin impulse [143, 46, 68]. Here ζ is varied by adjusting the maximum bubble radius R_0, the driving pressure Δp, and the pressure gradient $\left|\nabla p\right|$ (through variable gravity). Measuring at variable gravity allows for the decoupling of the roles of the driving pressure (Δp) and bubble deformation (ζ), which is important because the expression of ζ for gravity-induced deformation includes Δp. The pressure-field anisotropy caused by the nearest boundary in our experiment is considered with $\zeta = -0.195\gamma^{-2}$ (which represents the dimensionless Kelvin impulse for bubbles near boundaries [143]), where γ is the standoff parameter $\gamma = s/R_0$ and where $s = 55$ mm is the distance between the bubble center and the parabolic mirror. The resultant ζ is given by the vector sum of the respective directional $\boldsymbol{\zeta}$. We expect luminescence to vary with ζ, since an increasing ζ implies stronger bubble deformation, which, in turn, affects the different events associated with the bubble collapse, such as microjets [143, 46] and shock waves [94, 159].

4.3 Spectral analysis in variable gravity

Selected images of high-speed movies visualizing luminescing bubbles of the same energy E_0 collapsing at different levels of ζ at normal gravity are shown in Fig. 4.4. The bubble interface, the luminescence, and the sharp shock waves are captured in the same movie, owing to the short exposure time (50 ns). We observe a weakening of the luminescent flash with increasing ζ. One may also see a pronounced deflection of light near the bubble wall in the frames preceding the luminescence, which is due to the pressure rise in the surrounding liquid predicted by Lord Rayleigh a century ago [51]. At $\zeta = 3.8 \times 10^{-3}$ there is no visible luminescence and the bubble's deformation is clearly manifested by the emitted shock wave(s) no longer being spherically symmetric.

The luminescence spectrum is well approximated by the blackbody model [104, 170], and since the bubble temperature cannot be directly measured, a fitted blackbody provides a reasonable estimation for it. The effective blackbody temperature and energy of luminescence can be inferred by fitting the spectra with a Planckian function of the form

$$L(\lambda, I, T_{\mathrm{lum}}) = A\frac{I}{\lambda^5}\frac{1}{\exp\left(\frac{hc}{\lambda k_B T_{\mathrm{lum}}}\right) - 1} \text{ [J/nm]} \tag{4.1}$$

where λ is the wavelength, h and k_B are the Planck and Boltzmann constants, respectively, c is the speed of light, A is a constant prefactor determined from calibration, T_{lum} is the blackbody temperature, and I stands for the product of the luminescence pulse duration and the projected emitting surface (which cannot be disentangled with the spatial and temporal resolution of our apparatus). The best-fit values are obtained by fitting Eq. (4.1), after correcting it for the absorption losses in Fig. 4.3, with the measured raw spectra through maximum likelihood for the pair (E_{lum},T_{lum}), where $E_{\mathrm{lum}} = IT_{\mathrm{lum}}^4$ is the luminescence energy through the Stefan-Boltzmann law. The estimated standard error of the maximum likelihood fit is obtained from the covariance matrix (estimated via the inverse of the Hessian matrix) representing the goodness of fit to the data. Figure 4.5 displays a typical measured luminescence spectrum

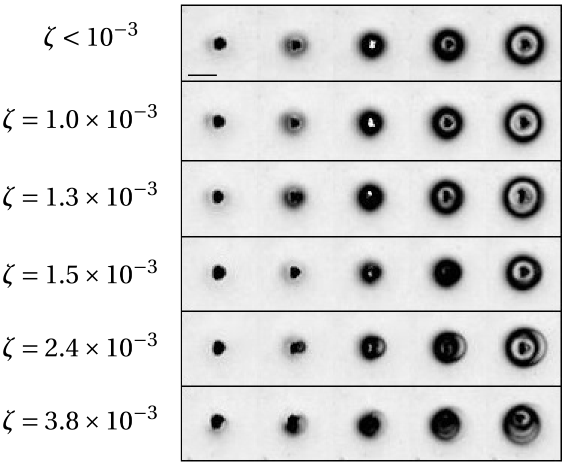
$\zeta < 10^{-3}$
$\zeta = 1.0 \times 10^{-3}$
$\zeta = 1.3 \times 10^{-3}$
$\zeta = 1.5 \times 10^{-3}$
$\zeta = 2.4 \times 10^{-3}$
$\zeta = 3.8 \times 10^{-3}$

Figure 4.4: Visualization of luminescence emitted at the final collapse stage of a single cavitation bubble at various ζ. The luminescent flash is visible in the middle frame and followed by the rebound. The interframe time is 100 ns, the exposure time is 50 ns, and the black line in the top panel shows the 1-mm scale. The bubble energy is the same in all cases ($E_0 \approx 27$ mJ) and ζ is varied by adjusting the driving pressure, from top to bottom, as $\Delta p = 98$, 78, 58, 48, 28, and 18 kPa, yielding maximum bubble radii of $R_0 = 4.1$, 4.3, 4.8, 5.1, 6.1, and 7.1 mm. These bubbles were imaged on-ground at normal gravity.

from a single bubble collapse.

We estimate the total luminescence energy E_{lum} by assuming a uniform light emission in the solid angle of 4π. In this way, 6.7% of all the photons are expected to reach the calibrated spectrometer detector. We use as a reference a highly spherical bubble collapsing in microgravity, which is assumed to undergo no displacement from the focal point of the parabolic mirror.

Figure 4.6(a) shows the luminescence energy E_{lum}, obtained through the best Planckian fit, as a function of the maximum bubble radius R_0 for three different ranges of driving pressure Δp. Only bubbles collapsing highly spherically ($\zeta < 7 \times 10^{-4}$) have been selected in order to exclude deformation-induced hindering of the luminescence, and the data include bubbles collapsing in microgravity. The maximum radii are within the range $R_0 = 1.5$–3.5 mm, which, to our knowledge, extend to the largest reported laser-induced luminescing bubbles collapsing freely and spherically in water. As expected, one may observe an increase in E_{lum} with increasing R_0 for a fixed Δp, the tendency being consistent with the literature [123, 106, 160]. In the literature, however, a decrease in luminescence energy for laser-induced bubbles with increasing maximum radii beyond $R_0 \approx 1.5$ mm has also been reported [160]. This is likely attributed to the use of less pointlike focusing methods (e.g., converging lens) that yield bubbles that are more disturbed in the collapse phase and cause, e.g., bubble splitting [106, 163], such disturbances being enhanced for increasing bubble radius. Bubbles with $R_0 > 3.5$ mm in our experiment are affected by the nearest surface, i.e., the parabolic mirror at a distance of 55 mm from the bubble center, which is accounted for in ζ.

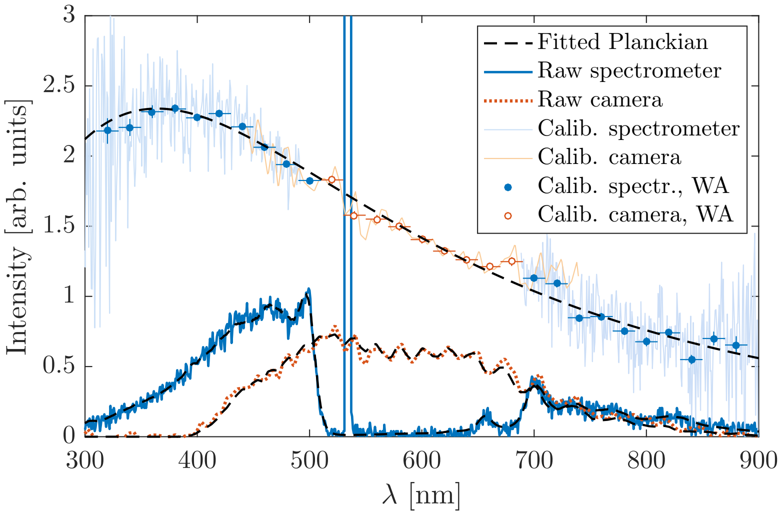

Figure 4.5: Typical luminescence spectrum from a single bubble collapse, measured with a spectrometer with an exposure time of 8 ms and a high-speed CCD camera with an exposure time of 10 μs. Both raw and calibrated spectra are shown, together with the fitted Planckians. Window averages (WAs) of 20-nm windows are also displayed. The peak around 532 nm is caused by the strong laser pulse despite the > 99% attenuation of the filter. Here $R_0 = 3.0$ mm, $\Delta p = 78$ kPa, and $|\mathbf{g}| = 1\ g$.

For a given R_0, a lower Δp yields weaker luminescence, which is expected since $E_{\text{lum}} \propto E_0 = (4\pi/3)R_0^3\Delta p$ [171, 163]. Figure 4.6(b) verifies this relation but still suggests slightly weaker luminescence energies for bubbles collapsing with a lower Δp. This result is consistent with the past observation of more energetic luminescence from bubbles collapsing at higher static pressures for a fixed E_0 [171]. Bubbles at a low Δp have a longer collapse time and thereby an increased surface area and interaction time, possibly yielding increased energy loss by thermal conduction or mass flow by nonequilibrium evaporation or condensation at the bubble wall [171].

The important scatter of our results is due to the limited reproducibility of the luminescence. We find the spectral intensities between individual bubbles under the same conditions to vary by approximately 45%, while the maximum bubble radii vary by less than 1%. These brightness fluctuations are likely related to the microscopic size of the luminescent plasma, which makes it highly sensitive to minor perturbations and easily obscured by nuclei and impurities in the water.

Figure 4.7 displays three examples of typical spectra of single-cavitation-bubble luminescence, with the only varying parameter being the perceived gravity level (0 g, 1 g, and 1.8 g). It is evident that the gravity-induced pressure gradient quenches the single-cavitation-bubble luminescence energy. Surprisingly, on none of the raw spectra do we observe a prominent peak corresponding to OH^- or other emission lines at any wavelength, even for the most deformed

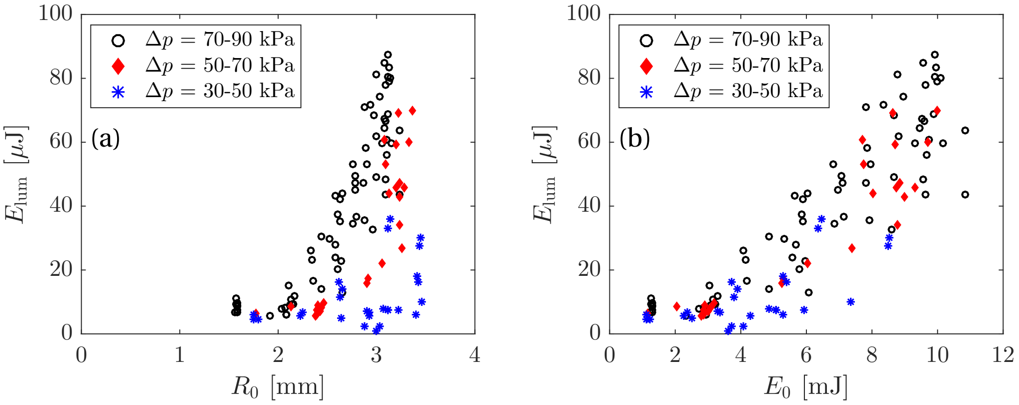

Figure 4.6: Luminescence energy E_{lum} as a function of (a) the maximum bubble radius R_0 and (b) the bubble energy E_0 for three ranges of driving pressures Δp. Each point corresponds to a measurement from a single, spherical collapse ($\zeta < 7 \times 10^{-4}$).

luminescing bubbles. This could, however, be due to the limited wavelength-resolution of our apparatus.

To quantify the fraction of the bubble energy dissipated into luminescence, we normalize the luminescence energy E_{lum} to the bubble energy E_0. We only retain cases where luminescence is detected by both the spectrometer and the CCD camera. Note that the CCD signal helps correcting the spectrum of the spectrometer if the bubble moves out of the focal point of the parabolic mirror during its collapse. The dependence of the relative luminescence energy on the anisotropy parameter ζ is displayed in Fig. 4.8(a). Here ζ is altered by a wide range of R_0, $\mathbf{g}$, and Δp in order to disentangle their respective effects on luminescence from that of the bubble deformation. The maximum Δp was achieved when the test vessel reached the aircraft cabin pressure, i.e., $p_0 \approx 80$ kPa. The results show a rapid quenching of the relative luminescence energy with increasing ζ. Luminescence takes up to approximately 1% of the bubble's initial energy. The rest of the bubble's energy is distributed predominantly into shock-wave emission and the formation of a rebound bubble for spherically collapsing bubbles [48]. Owing to microgravity, we are able to create large bubbles, which in normal gravity would be deformed, that collapse highly spherically at low Δp and emit luminescence. Correspondingly, higher gravity levels allow us to stretch the range of ζ to higher values for a given Δp. Up to the scatter, the data points exhibit a linear trend on a logarithmic scale as a function of ζ regardless of the gravity level. Luminescence is not detected by the spectrometer for anisotropy levels beyond $\zeta \approx 3.5 \times 10^{-3}$, which corresponds to the same Kelvin impulse at $\gamma \approx 7.5$ for bubbles deformed by neighboring surfaces [143]. Note that we only obtain reliable fitted blackbody energies, which require the CCD signal, up to $\zeta \approx 1.8 \times 10^{-3}$ [in Fig. 4.8(a)], due to the poor signal-to-noise ratio of luminescence from more deformed bubbles.

Figure 4.8(b) displays our best-fit estimates of the bubble's blackbody temperatures as a

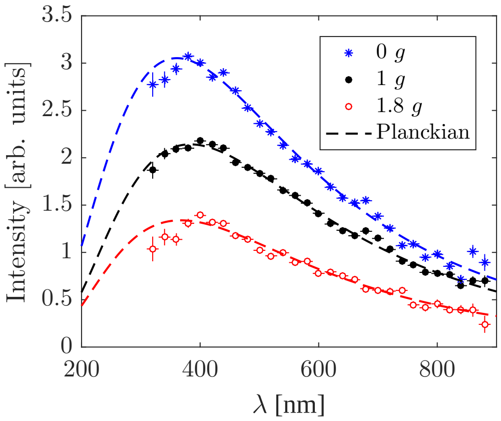

Figure 4.7: Single-cavitation-bubble luminescence spectra at three gravity levels for the same laser pulse energy ($R_0 = 3 \pm 0.1$ mm) and static pressure of the water ($p_0 = 81 \pm 1$ kPa). Each spectrum is measured at a single bubble collapse.

function of ζ. We obtain reliable fitted blackbody temperatures, which only require the spectrometer signal, up to $\zeta \approx 2.5 \times 10^{-3}$. The temperatures fall in the range $T_{\mathrm{lum}} = 7000$–11500 K, which is in good agreement with previous laser-induced bubble luminescence studies, in which the temperatures from averaged spectra varied between 7680 K (close to a solid surface) and 9150 K (at elevated ambient pressure) [163, 161]. This range, however, is attributed to the important scatter (which is expected owing to the experimental and fitting errors) rather than a clear relationship with the governing parameters. The highly spherical bubbles with the highest luminescence energies do not exhibit higher blackbody temperatures than the luminescing deformed bubbles. This result is in disagreement with the observations of Brujan and Williams [163], who found the temperatures (estimated from averaged spectra) to decrease with decreasing distance between the bubble and a rigid boundary, that is, with increasing bubble deformation.

4.4 Time-resolved measurements

The luminescence pulse duration for spherically collapsing laser-induced cavitation bubbles has been shown to be on the nanosecond scale and to scale with the maximum bubble radius R_0. For example, for $R_0 = 0.3$ mm, the full width at half-maximum (FWHM) has been measured as $\tau \approx 3$ ns [106, 163]; for $R_0 = 1$ mm, $\tau \approx 6$–8 ns [160, 163]; and for $R_0 = 1.8$ mm, $\tau \approx 10$ ns [160]. Centimetric bubbles generated by a spark or expanded through a chemical reaction may luminesce for tens of microseconds [164, 167]. Owing to the high sphericity of the initial plasma generating the bubble, large bubbles in our experiment ($R_0 > 2$ mm) are able to collapse spherically without bubble splitting decreasing the efficiency of the final gas compression. We therefore expect the luminescence pulse durations here to exceed those reported in the literature for laser-induced bubbles.

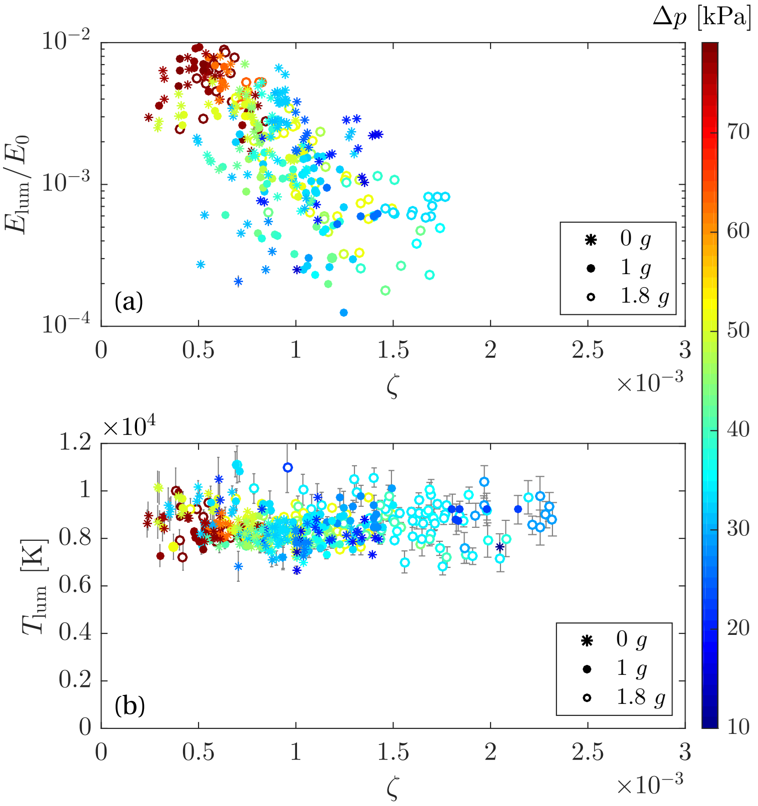

Figure 4.8: Single-cavitation-bubble luminescence (a) relative energy E_{lum}/E_0 and (b) blackbody temperature T_{lum} as a function of the anisotropy parameter ζ. Each data point represents a single bubble measurement. Colors indicate driving pressures and symbols indicate different levels of gravity. Error bars indicate the $\pm\sigma$ uncertainty of the best-fit estimate of the blackbody temperature, while the error for the E_{lum}/E_0 estimate is small ($\sigma \sim 10^{-5}$).

Figures 4.9(a)–4.9(f) show waterfall plots of 20 photodetector signals measured from single bubble collapses with a fixed bubble energy $E_0 \approx 22$ mJ and at different driving pressures Δp. The signals are sorted so that the peak amplitudes are in descending order from bottom to top. Here $t = 0$ μs corresponds to the instant at which the hydrophone detects the collapse shock, which has propagated a distance of 37 mm from the bubble. It should be noted that the amplitudes of the photodetector signals are not corrected for the bubble displacement. All photodetector measurements are made on-ground at normal gravity. The standard deviation of the maximum peak timing with respect to $t = 0$ μs ranges from 8 to 12 ns. Consistent with the spectral analysis in Sec. 4.3, the energy of the luminescence signals decreases with increasing ζ. The number of peaks in the photodetector signals varies between one and four, suggesting multiple events yielding light emission. Similar peaks have been observed in the past in photomultiplier tube measurements for both single and multiple bubble collapses [160, 172]. Such multiple peaks are often randomly distributed in time with respect to the strongest peak,

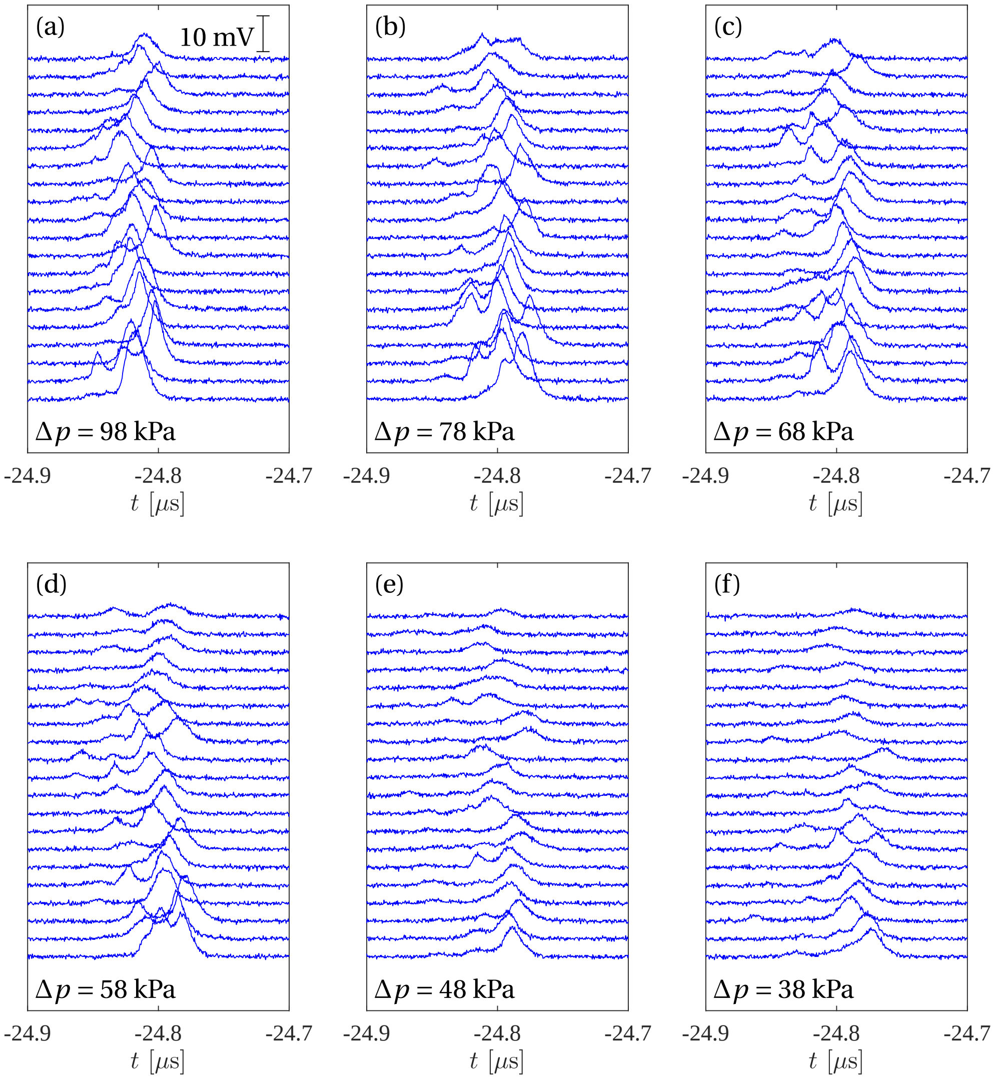

Figure 4.9: Waterfall plots of the luminescence signals measured by the photodetector for different driving pressures: (a) Δp = 98 kPa (R_0 = 3.8 mm, $\zeta = 7.8 \times 10^{-4}$), (b) Δp = 78 kPa (R_0 = 4.0 mm, $\zeta = 9.0 \times 10^{-4}$), (c) Δp = 68 kPa (R_0 = 4.2 mm, $\zeta = 9.9 \times 10^{-4}$), (d) Δp = 58 kPa (R_0 = 4.5 mm, $\zeta = 1.1 \times 10^{-3}$), (e) Δp = 48 kPa (R_0 = 4.7 mm, $\zeta = 1.3 \times 10^{-3}$), and (f) Δp = 38 kPa (R_0 = 5.1 mm, $\zeta = 1.6 \times 10^{-3}$). $E_0 \approx 22$ mJ. Each plot contains 20 signals. The scaling shown in (a) is the same in all plots. Here $t = 0$ μs corresponds to the instant at which the hydrophone detects the collapse shock. The standard deviations for R_0 and ζ are $\sigma_{R_0} \approx 0.03$ mm and $\sigma_\zeta \approx 1.5 \times 10^{-5}$, respectively. Measurements were made at normal gravity.

which, for the majority of cases, is the last event. Figures 4.9(a)–4.9(c) show signals with up to two peaks, and at lower driving pressures [Figs. 4.9(d) and 4.9(f)], where the amplitudes have substantially decreased, even three or four peaks may be observed. The luminescence events occur within a time frame of approximately 200 ns.

Figures 4.10(a)–4.10(l) show the averages of the photodetector signals at three driving pressures (Δp = 98, 58, and 38 kPa) and at four bubble energies (E_0 = 22, 15, 9, and 5 mJ). Each maximum peak is set to $t = 0$ ns when the averaging is performed. The range covered by the individual signals and the standard deviations are also displayed. The more energetic bubbles show multiple peaks [Figs. 4.10(a)–4.10(f)], while at lower energies luminescence is measured as a single peak [Figs. 4.10(g)–4.10(l)]. Figures 4.10(c) and 4.10(j) display signals with similar peak amplitudes, yet the high-energy bubble collapsing at low pressure yields multiple peaks while the low-energy bubble collapsing at atmospheric pressure yields a single peak. Figures 4.10(d) and 4.10(h) display signals for bubbles with the same maximum radius but with different energies, and, again, the higher-energy bubble yields more prominent additional peaks than the low-energy one. However, we find no clear correlation between the number, amplitudes, or timings of the peaks and the bubble's asphericity.

Figures 4.11(a) and 4.11(b) show the measured luminescence durations as the FWHM and the full width, which are extracted directly from the average of 20 individual photodetector signals. The full width here is defined as the duration of the averaged signal above 1% of its peak amplitude (the noise in the averaged signals has been smoothed out sufficiently not to affect this low threshold). In order to complete the graph for previously measured luminescence durations for smaller laser-induced bubbles, FWHM data from Baghdassarian *et al.* (1999) [106] and from Ohl (2002) [160] are included for purposes of comparison. The trend for the duration of these large bubbles remains similar to that for the previously reported smaller bubbles, that is, approximately linear as a function of R_0. While past research has suggested that the pulse duration increases for bubbles collapsing at higher pressures [163] and for bubbles deformed by a neighboring surface [160], the direct roles of Δp and ζ on the pulse duration in our results are unclear. In particular, luminescence durations at Δp = 38 kPa seem to be outliers from the general trend, with the FWHM remaining almost constant for R_0 = 3–5 mm.

Finally, a typical example of an ultra-high-speed CMOS camera recording of the luminescence is shown in Fig. 4.12 where luminescence events are visible in the visualization with a backlight illumination [Fig. 4.12(a)] and in the dark [Fig. 4.12(b)] for a relatively deformed bubble. Figure 4.12(b) shows the luminescent flash in the dark in two frames and thereby implies that the total luminescence event duration here exceeds the interframe time of 100 ns, consistent with the photodetector measurements [see Fig. 4.11(b) for $R_0 \approx 5$ mm]. The images here likely only capture the beginning and the end of the light emission, while the peak intensity occurs between the images (the exposure time 50 ns covers only half of the interframe time). In fact, the CMOS camera systematically captures the luminescent flash in two or even three consecutive frames and occasionally gets saturated. We also observe an upward shift of

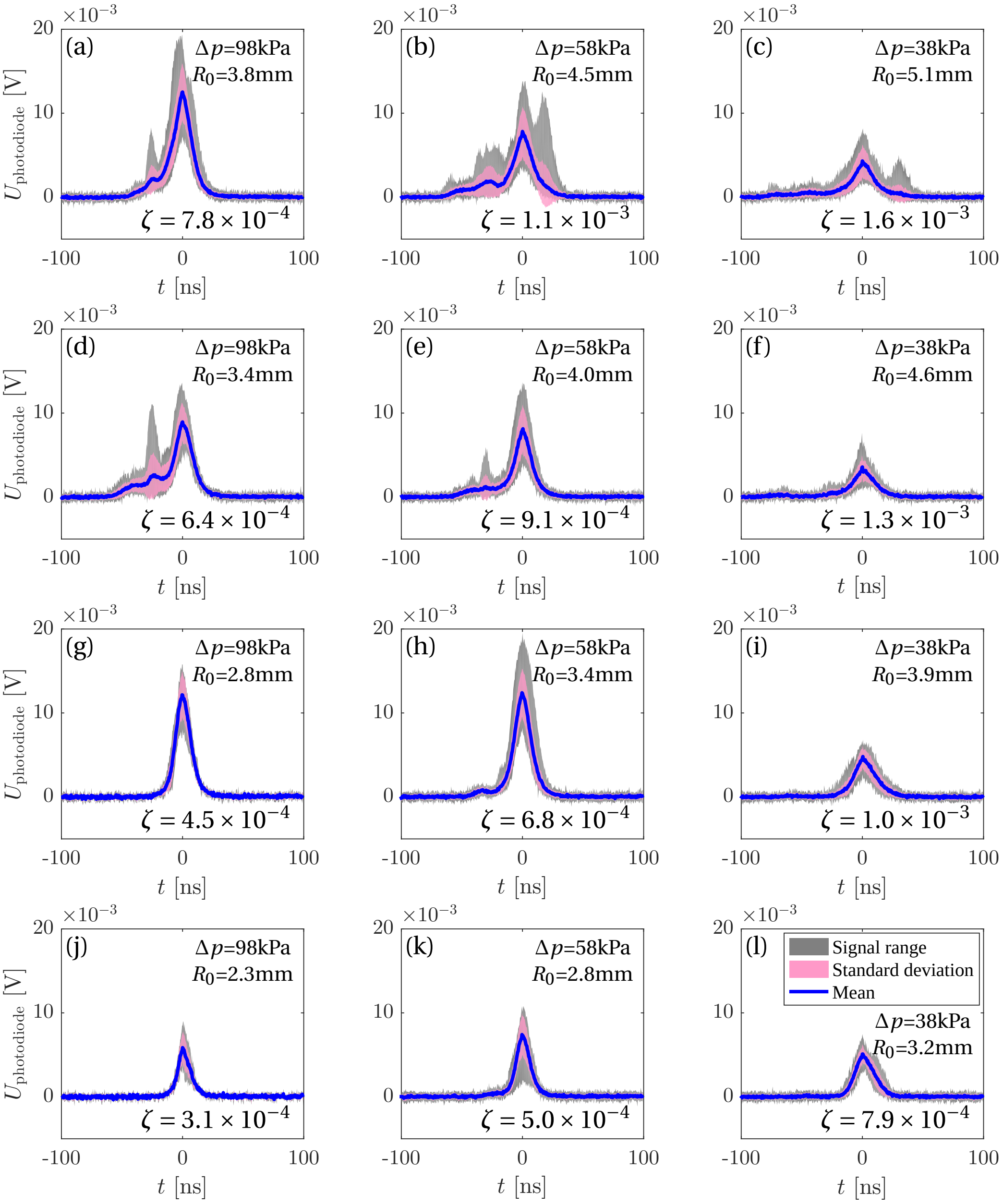

Figure 4.10: Mean of 20 luminescence signals measured by the photodetector for different bubble energies - (a)–(c) $E_0 = 22$ mJ, (d)–(f) $E_0 = 15$ mJ, (g)–(i) $E_0 = 9$ mJ, and (j)–(l) $E_0 = 5$ mJ and three driving pressures: $\Delta p = 98$, 58 and 38 kPa. The ranges covered by the individual signals and the standard deviations are also displayed. Here $t = 0$ ns corresponds to the maximum peak.

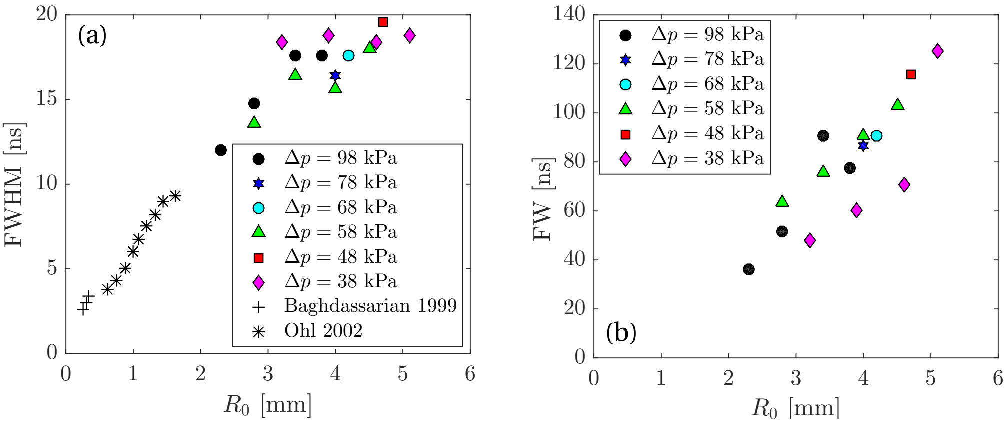

Figure 4.11: (a) Full width at half-maximum (FWHM) and (b) full width (FW; with 1% of the peak amplitude as threshold) of the luminescence as a function of R_0. The durations were extracted directly from the averaged photodetector signals of 20 bubbles. FWHM data at atmospheric pressure from Baghdassarian *et al.* (1999) [106] and from Ohl (2002) [160] are shown for reference.

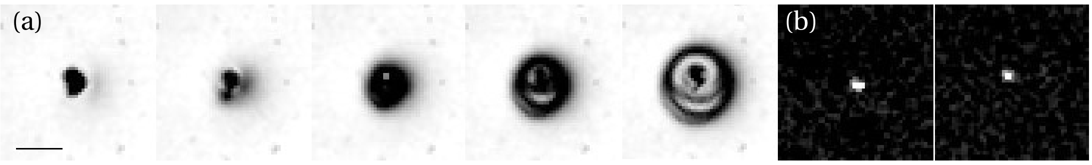

Figure 4.12: Images of the luminescence emission of a bubble collapsing at $\Delta p = 38$ kPa and normal gravity ($R_0 = 5.1$ mm, $\zeta = 1.3 \times 10^{-3}$) captured with an ultra-high-speed CMOS camera: (a) with a backlight LED and (b) in the dark. The black barin the leftmost panel shows the 1-mm scale. The interframe time is 100 ns and the exposure time is 50 ns. The contrast and brightness of the images have been adjusted to optimize the visual clarity of events.

the light spot in the images in Fig. 4.12(b). This might be expected, because according to momentum conservation, most of the bubble's translational motion upon its nonspherical collapse occurs during its last collapse and early rebound stages, when the luminescence is emitted. The bubble centroid's upward displacement during the collapse is clearly visible in Fig. 4.12(a).

4.5 Discussion

The results presented here provide insight into how the topological changes in the cavity volume from a spherical to a jetting bubble affect the degree of adiabatic heating. Luminescence has an appreciable sensitivity to even the finest pressure-field anisotropies in the liquid caused by the gravity-induced pressure gradient. The threshold beyond which luminescence is no

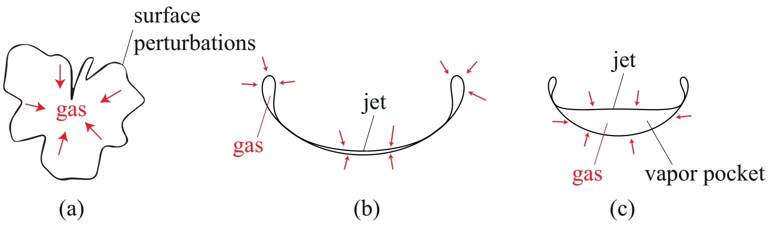

Figure 4.13: Illustration of the possible effect of the bubble's surface perturbations on its gas compression. Sketches of shapes at the final collapse stage for a bubble (a) with surface perturbations, (b) with a downward jet induced by a uniform pressure gradient, and (c) with a downward jet induced by a neighboring free surface.

longer observed, $\zeta \approx 3.5 \times 10^{-3}$, is close to the limit where we start observing jetting bubbles in our experiment ($\zeta \sim 10^{-3}$), the latter, however, being a limit that is difficult to define with precision. Considering a bubble deformation by nearby boundaries yielding an identical Kelvin impulse [$\gamma = \left(0.915\zeta^{-1}\right)^{1/2}$ [143], where, equivalently, $\gamma = s/R_0$, s being the distance between the bubble and the boundary], the threshold at which we no longer detect luminescence here would be equivalent to a bubble collapsing at a distance of 7.5 times its maximum radius from the boundary. This limit disagrees with previous studies on luminescence from laser-induced bubbles deformed by near boundaries, where the equivalent limit is much lower, e.g., $\gamma \sim 3.5$ in Refs. [123] and [163] (corresponding to $\zeta \sim 0.016$). This discrepancy is possibly attributed either to different sources of deformations yielding different levels of gas compression, or to the sensitivity of luminescence to the initial bubble sphericity. The latter hypothesis is supported by our previous observation that the level of deformation at which a microjet visibly pierces the bubble and drives a vapor jet during the rebound for bubbles deformed by near surfaces in our experiment ($\zeta \approx 10^{-3}$ or $\gamma \approx 14$) is also significantly lower compared to the literature (typically $\gamma \approx 5$) [143]. Likewise, we have recently measured the shock-wave energy to start being sensitive to ζ at longer distances away from surfaces ($\gamma \approx 8$ [159]) compared to the literature ($\gamma \approx 3$ [94]). As mentioned earlier, lens-based bubble generation systems, in contrast to the use of a high-convergence parabolic mirror, produce bubbles with higher surface perturbations that are amplified during the last collapse stage [107]. Consequently, a potential microjet, which can be regarded as the lowest-order deviation from a sphere and is thus most effective at inhibiting the final gas compression, may be masked by more important, higher-order perturbations. This could make the bubble experience a collapse that perhaps more effectively compresses the gas and that is less susceptible to external factors, possibly even appearing spherical. This hypothesis is illustrated in Fig. 4.13.

However, luminescence can also occur for jetting bubbles, as has previously been shown for bubbles deformed by a neighboring surface [123], for acoustic cavitation bubbles in multibubble fields in xenon-saturated phosphoric acid [162], and for xenon gas bubbles collapsed by a passing shock wave [173]. A possible reason for our not observing light emission for bubbles that produced clear gravity-driven "vapor jets" upon rebound could be linked to the characteristic shape that the bubble assumes at the moment of the jet piercing. We have previously shown that, according to potential flow theory, the gravity-induced deformation yields a broad jet whose shape is very similar to that of the bubble wall it pierces [143], and thereby the gas compression after the jet impact becomes particularly weak [see Fig. 4.13(b)]. In contrast, when the bubble is deformed by a neighboring rigid or a free surface, at certain ranges of ζ, potential flow theory predicts small vapor "pockets" remaining between the jet and the opposite bubble wall upon the first contact of the jet with it [143], such as in the illustration in Fig. 4.13(c). We have previously observed luminescence from the location at which the jet pierces the bubble wall for bubbles collapsing near a free surface, as shown in Fig. 4.14 (adapted from Ref. [159]). This is due to the contact between the jet and the opposing wall being more irregular, which is characteristic of bubbles near free surfaces. The jet thus divides the bubble into multiple separate segments, one of which is a vapor pocket between the jet and the opposite wall that is individually able to collapse in an almost spherical way, which, in turn, yields an effective compression. This hypothesis is supported by our previous observations where such vapor pockets emitted strong shocks for bubbles near a free surface [159]. However, we are unable to temporally distinguish the jet impact from the individual collapses of the remaining bubble segments at a low enough ζ for luminescence to still be visible. It would be interesting in the future to study more thoroughly the effect of the bubble shape on luminescence by varying this shape with different sources of deformation (e.g., comparing different surfaces and gravity) in a single setup.

A surprising finding is that the spectroscopically estimated blackbody temperatures of luminescence barely vary with the different levels of bubble deformation [Fig. 4.8(b)], while its energy varies by two orders of magnitude [Fig. 4.8(a)]. We do not exclude the possibility that the scatter of the data, partly caused by the fitting error, hides a possible weak variation of the blackbody temperature with ζ. However, it could also be due to the fact that as the radiation power scales as T_{lum}^4, any attempt to increase T_{lum} immediately results in an accelerated loss of energy by radiation. Another potential physical reason could be the presence of water vapor which increases the heat capacity ratio [174, 175, 43]. It has been shown numerically that for sonoluminescent bubbles that have compression ratios beyond $R_0/R_{\mathrm{min}} \sim 20$, water vapor starts affecting the power-law increase in the maximum temperature with the compression ratio, finally asymptoting to $T_{\mathrm{lum}} \approx 10000$ K [174]. It is difficult to measure the minimum bubble size in our experiment because the luminescence and the light deflection caused by the pressure rise in the surrounding liquid "hide" the bubble in the last stage of the collapse (see images in Fig. 4.4). However, when choosing the luminescent flash size as the minimum radius, we get compression ratios $R_0/R_{\mathrm{min}} > 40$, which is already in the regime where vapor affects the heating.

The noncondensible gas trapped inside the bubble plays a key role in luminescence emission. We believe that the bubble contains (i) vapor, of which the partial pressure is assumed to stay at the liquid vapor pressure p_v during most of the bubble's lifetime; (ii) the laser-generated gas (demonstrated in Ref. [37]), which we assume to depend on the energy deposited by the laser to generate the bubble, that is, to be proportional to $E_{\mathrm{laser}} \propto E_0 \propto R_0^3 \Delta p$; and (iii) the diffused

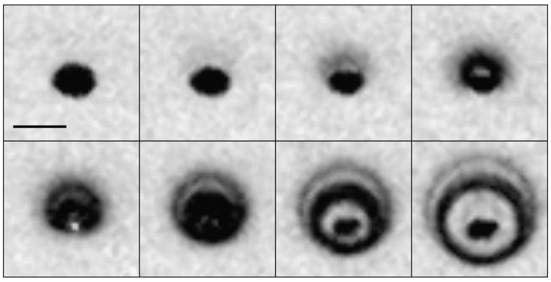

Figure 4.14: Luminescence emission at the location of jet impact for a bubble collapsing near a free surface. R_0 = 4.1 mm, γ = 7.2. The interframe time is 100 ns and the black bar in the top-left panel shows the 1-mm scale. The microjet is directed downwards. Adapted from Ref. [159].

gas from the water to the bubble, which depends both on the total bubble surface during its lifetime, which is proportional to $R_0^3 \Delta p^{1/2}$, and on the diffusion-driving pressure Δp. Each of these likely contributes to the noncondensible gas, which is difficult to measure directly. The laser-generated and diffused gases are both proportional to the bubble's maximum volume, while they may depend on Δp to a different extent. A method has been proposed by Tinguely *et al.* [48] to estimate the initial partial pressure of the noncondensible gas p_{g_0} by fitting the Keller-Miksis model [61] to the observed rebound. Applying this method to the observed radial evolution of spherically collapsing bubbles at various Δp values in microgravity, we can estimate the variation of p_{g_0} as a function of Δp. Our preliminary results find that p_{g_0} remains almost constant ($p_{g_0} \approx 4$ Pa) for the range of Δp covered here, differing less than the standard deviation, as illustrated in Fig. 4.15. Furthermore, the luminescence energy data obtained in this range of Δp in Fig. 4.8 suggest that the bubble's deformation (ζ) is the dominant source of luminescence energy hindering rather than Δp, even though a weak dependence on the latter may exist. Figure 4.6, which shows luminescence energies as a function of the bubble energy at different Δp's, however, suggests some additional dependence of the luminescence energy on Δp. A systematic study with a controlled gas content of the water, preferably in microgravity to remove the effect of bubble deformation by gravity, would be useful to clarify the effect of noncondensible gas on luminescence and on other bubble collapse phenomena.

Finally, it would be interesting to understand the physics behind the multiple luminescence emission events that are measured by the photodetector (Figs. 4.9 and 4.10). These peaks show considerable fluctuations in their numbers, amplitudes, shapes, and timings. The timing of the strongest luminescence event with respect to the emission of the collapse shock wave is remarkably reproducible, varying by only ~ 10 ns (Fig. 4.9). The finding that larger bubbles emit more peaks than smaller ones is consistent with the literature, although the bubble sizes reported in the past were much smaller overall and multiple peaks were observed for bubbles with $R_0 < 2$ mm [160]. The discrepancy between our observations (single peak for $R_0 < 3$ mm) and the past literature is, again, likely due to the high initial sphericity of the bubble in our experiment. The multiple peaks could be associated with different hot spots, which

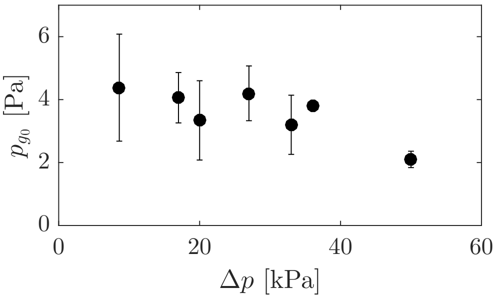

Figure 4.15: Averaged initial partial pressure of the noncondensible gas, estimated by fitting the Keller-Miksis model to the observed rebound radial evolution, as a function of the driving pressure Δp. The data contain bubbles of different radii (1–3.5 mm) collapsing highly spherically ($\zeta < 0.0007$), and error bars show the standard deviation.

could be the result of an inhomogeneous bubble interior or bubble splitting, as suggested by Ohl [160]; this would indeed be strongly affected by the initial bubble sphericity. They could also be linked to plasma instabilities, to minor impurities trapped within the bubble, or to the potential formation of a "hidden" (nonpiercing) microjet, which is challenging to verify since the levels of deformations here are so weak.

4.6 Conclusion

In this work, we have captured broad spectra of single-cavitation-bubble luminescence from individual collapses using an innovative measurement technique. We have measured luminescence from a previously uncovered range of maximum radii (R_0 = 1.5–6 mm) of laser-induced bubbles, thanks to their high initial sphericity. The bubbles were controllably deformed from highly spherical to jetting bubbles under the effect of the gravity-induced hydrostatic pressure gradient. The deformation was quantified with the dimensionless anisotropy parameter ζ, which was adjusted via the maximum bubble radius, driving pressure, and variable gravity aboard parabolic flights. We found a rapid decrease in the relative luminescence energy E_{lum}/E_0 with ζ. No clear variation of the fitted blackbody temperature, which ranged between T_{lum} = 7000 and T_{lum} =11500 K, as a function of ζ or the driving pressure was found. The threshold of luminescence approximately coincides with the ζ at which we start observing vapor-jets in our experiment. The light emission is found to be nonuniform in time for the most energetic bubbles, as multiple events are detected in the time-resolved measurements by a photodetector, while low-energy bubbles emit single luminescence peaks. The luminescence events were found to occur in a time frame of 200 ns. The FWHM of the averaged luminescence signal scales with R_0 and is generally of the order of 10–20 ns.

5 Conclusion and perspectives

5.1 Conclusion

In this thesis, the most powerful phenomena taking place during the collapse of cavitation bubbles, namely micro-jets, shock waves, and luminescence, were investigated for various levels of bubble deformation. An interesting feature of these results is that they have combined, for the first time, orders of magnitude of parameter space in bubble energy, pressure, size and asymmetry in a single perspective. The different collapse phenomena have been measured simultaneously, thus allowing for the reconstruction of the full energy budget of a single bubble, and a theoretical framework (both numerical and analytical) has been established to understand and interpret the collapse properties measured from all these data.

Firstly, to define a rigorous way to quantify the level of a collapsing bubble's deformation caused by different sources of pressure field anisotropy, a detailed analysis on the formation of micro-jets was carried out. Ultra-high-speed visualisations captured the micro-jets, driven by a nearby rigid or a free surface or by the hydrostatic pressure gradient, propagating through the bubble interior and, sometimes, disintegrating within the rebound. The micro-jets were qualitatively divided into three visually distinct regimes: weak, intermediate and strong jets. Such classification was complemented quantitatively through delicate measurements of some of the key observables characterising these jets, such as the jet speed, jet impact timing, bubble centroid displacement, bubble volume at jet impact, and the vapour jet volume. The observations were supported by numerical simulations based on potential flow theory (boundary integral method). Interestingly, upon normalisation, these observables reduced to straightforward functions of the anisotropy parameter ζ, which represents a dimensionless version of the Kelvin impulse. Outside the strong jet regime, all of these functions could be approximated by useful power laws of ζ irrespective of the micro-jet diver. This behaviour was explained through analytical arguments.

Secondly, we investigated the shock wave emission from bubbles collapsing with varying levels of deformation. Detailed time-resolved observations of the multiple shock emission, which was associated with the jet impact-induced water hammer upon piercing the bubble and with the individual collapses of the different bubble segments, were performed using simultaneous high-speed imaging and hydrophone pressure measurements. Combining statistical analysis on a large number of data with theoretical arguments, we developed semi-empirical models approximating the peak pressures and energies of the shock waves as a function of ζ.

Finally, luminescence properties from bubbles deformed by the hydrostatic pressure gradient, modulated in variable gravity aboard parabolic flights, were explored as a function of ζ. An innovative luminescence measurement system was developed involving the simultaneous uses of a spectrometer and a high-speed CCD camera equipped with a diffraction grating lens. Such a system, combined with a bubble generation technique allowing for large bubbles to collapse spherically, is able to capture the spectra (300-900 nm) of the light emitted at individual bubble collapses. We found rapid quenching of luminescence energy as a function of ζ regardless of the gravity level, yet the fitted blackbody temperatures did not vary in a clear manner as a function of the governing parameters.

Overall, the Kelvin impulse has proven to be a valuable concept in describing the dynamics of non-spherically collapsing bubbles. The use of its dimensionless equivalent ζ implies approximating any pressure field by a uniform, stationary pressure field, which is justified if the characteristic time-scales are on the order of - or larger than - the bubble's Rayleigh collapse time. These results contribute to the understanding of different cavitation effects in known pressure fields and may serve as an exquisite benchmark for numerical simulations.

5.2 Perspectives

The final collapse phenomenon that was not discussed separately in this thesis is the rebound bubble. Despite rebounds not directly demonstrating interesting damaging properties similar to the other collapse events, knowing their dynamics as a function of the bubble deformation is important. This is because a considerable amount of the bubble's energy may go to the rebound's formation. Rebound bubbles may find themselves closer to surfaces than their 'mother' bubbles that have migrated towards the surface during their oscillation, and the subsequent collapse of these rebounds may be more damaging to the surface compared to the first collapse because of this proximity. Furthermore, our preliminary results suggest that, at a certain range of ζ, the shocks emitted at the second collapse can be more energetic compared to the first collapse (also previously observed in ref. [94]).

Further research should be done to quantify the amount of non-condensible gas inside the bubble. The bubble interior is affected by diffusion, condensation and accelerations, and require thorough modelling to obtain accurate predictions. With a controlled and monitored gas content of the liquid, one could assess the role and contents of the non-condensible gases within the bubble, and their effect on the different collapse phenomena.

It would be interesting to expand the predictive models presented in this work to other sources of bubble deformation, such as travelling compression waves, neighbouring oscillating bubbles, or directed focused ultrasound. Defining an anisotropy parameter ζ for such highly time-dependent events is challenging, possibly requiring to determine a time-averaged 'effective' pressure gradient. Also, predicting the dynamic properties of bubbles collapsing near (or confined within) complex geometries would be useful.

Since cavitation has recently been given increasing importance in medical applications, a predictive framework, similar to the one presented in this work, for bubbles in medical environments, such as in blood vessels or organic tissues, would be useful. This could be done by experimenting with single bubbles in non-Newtonian liquids similar to body fluids, near and within elastic structures (gels, sponges) and confinements (blood vessel-like structure), with varied gas contents, and within bubble clouds.

Finally, using Background-Oriented Schlieren [176], which has already been applied to measuring the shock waves generated by laser-induced bubbles [177, 178], one could experimentally quantify the pressure build-up occurring in the liquid around a spherically collapsing bubble during the latter's last phases of collapse (discussed in section 3.3.1). It would be interesting to determine how well Rayleigh's incompressible model predicts the pressures, which, in this model, are solely dependent on the compression ratio of the bubble, R_0/R, and the driving pressure Δp. Also, a systematic study on how the deformation affects this pressure build-up could be conducted to better understand the first shock waves emitted from weakly deformed bubbles (see figure 3.6). This could clarify the possible connection between the pressure rise and the shock waves, and their role on, for example, cavitation-induced crystallisation of liquids [146].

Bibliography

[1] F. Young. *Cavitation.* McGraw-Hill Book Company (UK) Limited, 1989.

[2] C. Brennen. *Cavitation and Bubble Dynamics*, volume 44. Oxford engineering science series, Oxford University Press, New York, 1995.

[3] J. Franc and J. Michael. *Fundamentals of cavitation*, volume 76. Springer, 2004.

[4] D. Silberrad. Propeller erosion. *Engineering*, 33:33–35, 1912.

[5] X. Escaler, E. Egusquiza, M. Farhat, F. Avellan, and M. Coussirat. Detection of cavitation in hydraulic turbines. *Mechanical systems and signal processing*, 20(4):983–1007, 2006.

[6] W.A. Spraker. The effects of fluid properties on cavitation in centrifugal pumps. *Journal of Engineering for Power*, 87(3):309–318, 1965.

[7] E. Rambod, M. Beizaie, M. Shusser, S. Milo, and M. Gharib. A physical model describing the mechanism for formation of gas microbubbles in patients with mitral mechanical heart valves. *Annals of Biomedical Engineering*, 27(6):774–792, 1999.

[8] J. Katz. Cavitation phenomena within regions of flow separation. *Journal of Fluid Mechanics*, 140:397–436, 1984.

[9] M. Dreyer, J. Decaix, C. Münch-Alligné, and M. Farhat. Mind the gap: a new insight into the tip leakage vortex using stereo-piv. *Experiments in Fluids*, 55(11):1849, 2014.

[10] J.K. Jakobsen and R.B. Keller Jr. Liquid rocket engine turbopump inducers. 1971.

[11] D. Dowson and C.M. Taylor. Cavitation in bearings. *Annual Review of Fluid Mechanics*, 11(1):35–66, 1979.

[12] H. Cochard. Cavitation in trees. *Comptes Rendus Physique*, 7(9-10):1018–1026, 2006.

[13] M. Versluis, B. Schmitz, A. von der Heydt, and D. Lohse. How snapping shrimp snap: Through cavitating bubbles. *Science*, 289(5487):2114–2117, 2000.

[14] S.N. Patek and R.L. Caldwell. Extreme impact and cavitation forces of a biological hammer: strike forces of the peacock mantis shrimp *Odontodactylus scyllarus*. *The Journal of Experimental Biology*, 208(19):3655–3664, 2005.

[15] W. Sass, M. Braunlich, H.-P. Dreyer, E. Matura, W. Folberth, H.-G. Priesmeyer, and J. Seifert. The mechanisms of stone disintegration by shock waves. *Ultasound in Medicine & Biology*, 17(3):239–243, 1991.

[16] M.R. Bailey, V.A. Khokhlova, O.A. Sapozhnikov, S.G. Kargl, and L.A. Crum. Physical mechanisms of the therapeutic effect of ultrasound (a review). *Biomicrofluidics*, 49(4):369–388, 2003.

[17] R.O. Cleveland and J.A. McAteer. The physics of shock wave lithotripsy. In *Smith's textbook on endourology*, volume 1, chapter 38, pages 529–558. 2007.

[18] C.D. Kelman. Phaco-emulsification and aspiration: A new technique of cataract removal: A preliminary report. *American Journal of Ophthalmology*, 64(1):23–35, 1967.

[19] P. Marmottant and S. Hilgenfeldt. A bubble-driven microfluidic transport element for bioengineering. *Proceedings of the National Academy of Sciences of the USA*, 101(26):9523–9527, 2004.

[20] T. Yu, Z. Wang, and T. J. Mason. A review of research into the uses of low level ultrasound in cancer therapy. *Ultrasonics Sonochemistry*, 11(2):95–103, 2004.

[21] I. Rosenthal, J. Z. Sostaric, and P. Riesz. Sonodynamic therapy - a review of the synergistic effects of drugs and ultrasound. *Ultrasonics Sonochemistry*, 11(6):349–363, 2004.

[22] K. Ferrara, R. Pollard, and M. Borden. Ultrasound microbubble contrast agents: Fundamentals and application to gene and drug delivery. *Annual Review of Biomedical Engineering*, 9:415–447, 2007.

[23] N. Nomikou and A. P. McHale. Exploiting ultrasound-mediated effects in delivering targeted, site-specific cancer therapy. *Cancer Letters*, 296(2):133–143, 2010.

[24] S. Ibsen, C.E. Schutt, and S. Esener. Microbubble-mediated ultrasound therapy: a review of its potential in cancer treatment. *Drug design, development and therapy*, 7:375–388, 2013.

[25] C.E. Brennen. Cavitation in medicine. *Interface Focus*, 5(5):20150022, 2015.

[26] A. Vogel. Nonlinear absorption: intraocular microsurgery and laser lithotripsy. *Phys. Med. Biol.*, 42(5):895–912, 1997.

[27] W.D. Song, M.H. Hong, B. Lukyanchuk, and T.C. Chong. Laser-induced cavitation bubbles for cleaning of solid surfaces. *Journal of Applied Physics*, 95(6):2952, 2004.

[28] D. Fernandez Rivas, B. Verhaagen, J.R.T. Seddon, A.G. Zijlstra, L.-M. Jiang, L.W.M. van der Sluis, M. Versluis, D. Lohse, and H.J.G.E. Gardeniers. Localized removal of layers of metal, polymer, or biomaterial by ultrasound cavitation bubbles. *Biomicrofluidics*, 6(3):034114, 2012.

[29] Z. Yin and A. Prosperetti. A microfluidic ‘blinking bubble’ pump. *J. Micromech. Microeng.*, 15(3):643–651, 2005.

[30] R. Dijkink and C.-D. Ohl. Laser-induced cavitation based micropump. *Lab on a Chip*, 8(10):1676–1681, 2008.

[31] Y. Tagawa, N. Oudalov, A. El Ghalbzouri, C. Sun, and D. Lohse. Needle-free injection into skin and soft matter with highly focused microjets. *Lab on a Chip*, 13(7):1357–1363, 2013.

[32] A. Patrascioiu, J.M. Fernández-Pradas, J.L. Morenza, and P. Serra. Microdroplet deposition through a film-free laser forward printing technique. *Applied Surface Science*, 258(23):9412–9416, 2012.

[33] T. J. Mason. Sonochemistry and the environment: Providing a green link between chemistry, physics and engineering. *Ultrasonics Sonochemistry*, 14(4):476–483, 2007.

[34] K. S. Suslick and G. J. Price. Applications of ultrasound to materials chemistry. *Annual Review Material Science*, 29(1), 1999.

[35] L. Albanese, R. Ciriminna, F. Meneguzzo, and M. Pagliaro. Beer-brewing powered by controlled hydrodynamic cavitation: Theory and real-scale experiments. *Journal of Cleaner Production*, 142:1457–1470, 2017.

[36] G.N. Kawchuk, J. Fryer, J.L. Jaremko, H. Zeng, L. Rowe, and R. Thompson. Real-time visualization of joint cavitation. *PLoS ONE*, 10(4):e0119470, 2015.

[37] T. Sato, M. Tinguely, M. Oizumi, and M. Farhat. Evidence for hydrogen generation in laser- or spark-induced cavitation bubbles. *Applied Physics Letters*, 102(7):074105, 2013.

[38] S. Fujikawa and T. Akamatsu. Effects of the non-equilibrium condensation of vapor on the pressure wave produced by the collapse of a bubble in a liquid. *J. Fluid Mechanics*, 97:481–512, 1980.

[39] J. Holzfuss, M. Rüggeberg, and A. Billo. Shock wave emissions of a sonoluminescing bubble. *Physical Review Letters*, 81(24):5434–5437, 1998.

[40] R. Pecha and B. Gompf. Microimplosions: Cavitation collapse and shock wave emission on a nanosecond time scale. *Physical Review Letters*, 84(6):1328, 2000.

[41] I. Akhatov, O. Lindau, A. Topolnikov, R. Mettin, N. Vakhitova, and W. Lauterborn. Collapse and rebound of a laser-induced cavitation bubble. *Physics of Fluids*, 13(10):2805, 2001.

[42] W. Lauterborn and C-D. Ohl. The peculiar dynamics of cavitation bubbles. In *In Fascination of Fluid Dynamics*, pages 63–76. Springer, 1998.

[43] M. Brenner, S. Hilgenfeldt, and D. Lohse. Single-bubble sonoluminescence. *Reviews of Modern Physics*, 74(2):425, 2002.

[44] W. Lauterborn and T. Kurz. Physics of bubble oscillations. *Rep. Prog. Phys*, 73(10):106501, 2010.

[45] T.B. Benjamin and A.T. Ellis. The collapse of cavitation bubbles and the pressures thereby produced against solid boundaries. *Philosophical Transactions of the Royal Society*, 260:221–240, 1966.

[46] D. Obreschkow, M. Tinguely, N. Dorsaz, P. Kobel, A. de Bosset, and M. Farhat. Universal scaling law for jets of collapsing bubbles. *Physical Review Letters*, 107(20):204501, 2011.

[47] O. Lindau and W. Lauterborn. Cinematographic observation of the collapse and rebound of a laser-produced cavitation bubble near a wall. *Journal of Fluid Mechanics*, 479:327–348, 2003.

[48] M. Tinguely, D. Obreschkow, P. Kobel, N. Dorsaz, A. de Bosset, and M. Farhat. Energy partition at the collapse of spherical cavitation bubbles. *Physical Review E*, 86(4):046315, 2012.

[49] Q.X. Wang. Local energy of a bubble system and its loss due to acoustic radiation. *Journal of Fluid Mechanics*, 797:201–230, 2016.

[50] G. Stokes. Add. MS. 7656. NB23, 1847. Notebook preserved in the Cambridge University Library.

[51] L. Rayleigh. On the pressure developed in a liquid during the collapse of a spherical cavity. *Philosophical Magazine*, 34:94–98, 1917.

[52] D. Obreschkow, P. Kobel, N. Dorsaz, A. de Bosset, C. Nicollier, and M. Farhat. Cavitation bubble collapse inside liquid spheres in microgravity. *Physical Review Letters*, 97(9):094502, 2006.

[53] M. Tinguely. *The effect of pressure gradient on the collapse of cavitation bubbles in normal and reduced gravity*. PhD thesis, Ecole Polytechnique Fédérale de Lausanne, Switzerland, 2013.

[54] S. Hilgenfeldt, M. P. Brenner, S. Grossman, and D. Lohse. Analysis of rayleigh-plesset dynamics for sonoluminescing bubbles. *Journal of Fluid Mechanics*, 365:171–204, 1998.

[55] D. Obreschkow, M. Bruderer, and M. Farhat. Analytical approximations for the collapse of an empty spherical bubble. *Physical Review E*, 85(6):066303, 2012.

[56] P. Amore and F.M. Fernández. Mathematical analysis of recent analytical approximations to the collapse of an empty spherical bubble. *J. of Chemical Physics*, 138(8):084511, 2013.

[57] N.A. Kudryashov and D.I. Sinelshchikov. Analytical solutions of the rayleigh equation for empty and gas-filled bubble. *Journal of Physics A: Mathematical and Theoretical*, 47(40):405202, 2014.

[58] M. Plesset. The dynamics of cavitation bubbles. *Journal of Applied Mechanics*, 16(3):227–282, 1949.

[59] L. Trilling. The collapse and rebound of a gas bubble. *Journal of Applied Mechanics*, 16(3):14–17, 1952.

[60] J. Keller and I. Kolodner. Damping of underwater explosion bubble oscillations. *Journal of Applied Physics*, 27(10):1152–1161, 1956.

[61] J.B. Keller and M. Miksis. Bubble oscillations of large amplitude. *The Journal of the Acoustical Society of America*, 68(2):628–33, 1980.

[62] A. Prosperetti. The equation of bubble dynamics in a compressible fluid. *Physics of Fluids*, 30(11):3626–3628, 1987.

[63] A. Prosperetti and A. Lezzi. Bubble dynamics in a compressible liquid. part 1. first-order theory. *Journal of Fluid Mechanics*, 168:457–478, 1986.

[64] A. Lezzi and A. Prosperetti. Bubble dynamics in a compressible liquid. part 2. second-order theory. *Journal of Fluid Mechanics*, 185:289–321, 1987.

[65] G. Hauke, D. Fuster, and C. Dopazo. Dynamics of a single cavitating and reacting bubble. *Physical Review E*, 75(6):066310, 2007.

[66] S.W. Gong, S.W. Ohl, E. Klaseboer, and B.C. Khoo. Scaling law for bubbles induced by different external sources: Theoretical and experimental study. *Physical Review E*, 81(5):056317, 2010.

[67] J.R. Blake and D.C. Gibson. Cavitation bubbles near boundaries. *Ann. Rev. Fluid Mech.*, 19(1):99–123, 1987.

[68] J.R. Blake. The kelvin impulse: application to cavitation bubble dynamics. *J. Austral. Math. Soc. Ser. B*, 30(2):127–146, 1988.

[69] J.R. Blake, D.M. Leppinen, and Q. Wang. Cavitation and bubble dynamics: the kelvin impulse and its applications. *Interface focus*, 5(5):20150017, 2015.

[70] B.B. Taib, G. Doherty, and J.R. Blake. High order boundary integral modelling of cavitation bubbles. Proceedings of 8th Australasian Fluid Mechanics Conference, 1983.

[71] P.B. Robinson, J.R. Blake, T. Kodama, A. Shima, and Y. Tomita. Interaction of cavitation bubbles with a free surface. *Journal of Applied Physics*, 89(12):8225, 2001.

[72] Y. Tomita, P.B. Robinson, R.P. Tong, and J.R. Blake. Growth and collapse of cavitation bubbles near a curved rigid boundary. *Journal of Fluid Mechanics*, 466:259–283, 2002.

[73] S. Zhang, J.H. Duncan, and G.L. Chahine. The final stage of the collapse of a cavitation bubble near a rigid wall. *Journal of Fluid Mechanics*, 257:147–181, 1993.

[74] A. Pearson, J.R. Blake, and S.R. Otto. Jets in bubbles. *Journal of Engineering Mathematics*, 48:391–412, 2004.

[75] Q.X. Wang and J.R. Blake. Non-spherical bubble dynamics in a compressible liquid. part 1. travelling acoustic wave. *Journal of Fluid Mechanics*, 659:191–224, 2010.

[76] Q.X. Wang and J.R. Blake. Non-spherical bubble dynamics in a compressible liquid. part 2. acoustic standing wave. *Journal of Fluid Mechanics*, 679:559–581, 2011.

[77] E. Johnsen and T. Colonius. Implementation of weno schemes in compressible multi-component flow problems. *Journal of Computational Physics*, 219(2):715–732, 2006.

[78] E. Johnsen and T. Colonius. Shock-induced collapse of a gas bubble in shockwave lithotripsy. *J. Acoust. Soc. Am.*, 124(4):2011–2020, 2008.

[79] E. Johnsen and T. Colonius. Numerical simulations of non-spherical bubble collapse. *Journal of Fluid Mechanics*, 629:231–262, 2009.

[80] G.L. Chahine. Modeling of cavitation dynamics and interaction with material. In *Experimental and Numerical Techniques for Cavitation Erosion Prediction, Series Fluid Mechanics and Its Applications*, volume 106, chapter 6. Springer, 2014.

[81] C.-T. Hsiao, J.-K. Choi, S. Singh, G.L. Chahine, T.A. Hay, Y.A. Ilinskii, E.A. Zabolotskaya, M.F. Hamilton, G. Sankin, F. Yuan, and P. Zhong. Modelling single- and tandem-bubble dynamics between two parallel plates for biomedical applications. *Journal of Fluid Mechanics*, 716:137–170, 2013.

[82] C.-T. Hsiao, A. Jayaprakash, A. Kapahi, J.-K. Choi, and G.L. Chahine. Modelling of material pitting from cavitation bubble collapse. *Journal of Fluid Mechanics*, 755:142–175, 2014.

[83] G.L. Chahine, A. Kapahi, J.-K. Choi, and C.-T. Hsiao. Modeling of surface cleaning by cavitation bubble dynamics and collapse. *Ultrasonics Sonochemistry*, 29:528–549, 2016.

[84] P. Koukouvinis, M. Gavaises, O. Supponen, and M. Farhat. Simulation of bubble expansion and collapse in the vicinity of a free surface. *Physics of Fluids*, 28(5):052103, 2016.

[85] P. Koukouvinis, M. Gavaises, O. Supponen, and M. Farhat. Numerical simulation of a collapsing bubble subject to gravity. *Physics of Fluids*, 28(3):032110, 2016.

[86] S. Li, Y.B. Li, and A.M. Zhang. Numerical analysis of the bubble jet impact on a rigid wall. *Applied Ocean Research*, 50:227–236, 2015.

[87] A.M. Zhang, S. Li, and J. Cui. Study on splitting of a toroidal bubble near a rigid boundary. *Physics of Fluids*, 27(6):062102, 2015.

[88] A.M. Zhang and Y.L. Liu. Improved three-dimensional bubble dynamics model based on boundary element method. *Journal of Computational Physics*, 294:208–223, 2015.

[89] S. Li, R. Han, A.M. Zhang, and Q.X. Wang. Analysis of pressure field generated by a collapsing bubble. *Ocean Engineering*, 117:22–38, 2016.

[90] L.T. Liu, X.L. Yao, A.M. Zhang, and Y.Y. Chen. Numerical analysis of the jet stage of bubble near a solid wall using a front tracking method. *Physics of Fluids*, 29(1):012105, 2017.

[91] T. Matula. Single-bubble sonoluminescence in microgravity. *Ultrasonics*, 38(1):559–565, 2000.

[92] E. A. Brujan, T. Ikeda, and Y. Matsumoto. Jet formation and shock wave emission during collapse of ultrasound-induced cavitation bubbles and their role in the therapeutic applications of high-intensity focused ultrasound. *Physics in medicine and biology*, 50(20):4797, 2005.

[93] M. Dular and O. Coutier-Delgosha. Thermodynamic effects during the growth and collapse of a single cavitation bubble. *Journal of Fluid Mechanics*, 736:44–66, 2013.

[94] A. Vogel and W. Lauterborn. Acoustic transient generation by laser-produced cavitation bubbles near solid boundaries. *J. Acoust. Soc. Am.*, 84(2):719, 1988.

[95] E.-A. Brujan, K. Nahen, P. Schmidt, and A. Vogel. Dynamics of laser-induced cavitation bubbles near an elastic boundary. *Journal of Fluid Mechanics*, 433:251–281, 2001.

[96] E. Robert, J. Lettry, M. Farhat, P.A. Monkewitz, and F. Avellan. Cavitation bubble behavior inside a liquid jet. *Physics of Fluids*, 19(6):067106, 2007.

[97] D. Obreschkow, M. Tinguely, N. Dorsaz, P. Kobel, A. de Bosset, and M. Farhat. The quest for the most spherical bubble: experimental setup and data overview. *Experiments in Fluids*, 54(4):1503, 2013.

[98] A.M. Zhang, P. Cui, J. Cui, and Q.X. Wang. Experimental study on bubble dynamics subject to buoyancy. *Journal of Fluid Mechanics*, 776:137–160, 2015.

[99] S. Zhang, S.P. Wang, and A.M. Zhang. Experimental study on the interaction between bubble and free surface using a high-voltage spark generator. *Physics of Fluids*, 28(3):032109, 2016.

[100] R.H. Cole. *Underwater explosions*. Princeton University Press, 1948.

[101] E. Klaseboer, K.C. Hung, C. Wang, C.W. Wang, B.C. Khoo, P. Boyce, S. Debono, and H. Charlier. Experimental and numerical investigation of the dynamics of an underwater explosion bubble near a resilient/rigid structure. *Journal of Fluid Mechanics*, 537:387–413, 2005.

[102] P. Cui, M. Zhang, and S.P. Wang. Small-charge underwater explosion bubble experiments under various boundary conditions. *Physics of Fluids*, 28(11):117103, 2016.

[103] D. Obreschkow, N. Dorsaz, P. Kobel, A. de Bosset, M. Tinguely, J. Field, and M. Farhat. Confined shocks inside isolated liquid volumes: A new path of erosion? *Physics of Fluids*, 23(10):101702, 2011.

[104] O. Baghdassarian, H-C. Chu, B. Tabbert, and G. Williams. Spectrum of luminescence from laser-created bubbles in water. *Physical Review Letters*, 86(21):4934, 2001.

[105] A. Vogel, S. Busch, K. Jungnickel, and R. Birngruber. Mechanisms of intraocular photodisruption with picosecond and nanosecond laser pulses. *Lasers in Surgery and Medicine*, 15(1):32–43, 1994.

[106] O. Baghdassarian, B. Tabbert, and G.A. Williams. Luminescence characteristics of laser-induced bubbles in water. *Physical Review Letters*, 83(12):2437, 1999.

[107] M.S. Plesset and T.P. Mitchell. On the stability of the spherical shape of a vapor cavity in a liquid. *Quarterly of Applied Mathematics*, 13(4):419, 1956.

[108] K.Y. Lim, P.A. Quinto-Su, E. Klaseboer, B.C. Khoo, V. Venugopalan, and C.-D. Ohl. Non-spherical laser-induced cavitation bubbles. *Physical Review E*, 81(1):016308, 2010.

[109] R.E.A. Arndt. Cavitation in fluid machinery and hydraulic structures. *Ann. Rev. Fluid Mech.*, 13(1):273–328, 1981.

[110] E. Stride and M. Edirisinghe. Novel microbubble preparation technologies. *Soft Matter*, 4(12):2350–2359, 2008.

[111] A. Vogel, W. Lauterborn, and R. Timm. Optical and acoustic investigations of the dynamics of laser-produced cavitation bubbles near a solid boundary. *Journal of Fluid Mechanics*, 206:299–338, 1989.

[112] A. Philipp and W. Lauterborn. Cavitation erosion by single laser-produced bubbles. *Journal of Fluid Mechanics*, 361:75–116, 1998.

[113] C.-D. Ohl, T. Kurz, R. Geisler, O. Lindau, and W. Lauterborn. Bubble dynamics, shock waves and sonoluminescence. *Philos. Trans. R. Soc. A*, 357(1751):269–294, 1999.

[114] D.C. Gibson. Cavitation adjacent to plane boundaries. *Proc. 3rd Australasian Conf. on Hydraulics and Fluid Mechanics*, (2597), 1968.

[115] C.D. Ohl and R. Ikink. Shock-wave-induced jetting of micron-size bubbles. *Physical Review Letters*, 90(21):214502, 2003.

[116] G.N. Sankin, W.N. Simmons, S.L. Zhu, and P. Zhong. Shock wave interaction with laser-generated single bubbles. *Physical Review Letters*, 95(3):034501, 2005.

[117] B. Gerold, P. Glynne-Jones, C. McDougall, D. McGloin, S. Cochran, A. Melzer, and P. Prentice. Directed jetting from collapsing cavities exposed to focused ultrasound. *Applied Physics Letters*, 100(2):024104, 2012.

[118] G.N. Sankin, F. Yuan, and P. Zhong. Pulsating tandem microbubble for localized and directional single-cell membrane poration. *Physical Review Letters*, 105(7):078101, 2010.

[119] Y.L. Levkovskii and V.P. II'in. Effect of surface tension and viscosity on the collapse of a cavitation bubble. *Inzhenerno-Fizicheskii Zhurnal*, 14(5):903–908, 1968.

[120] D.C. Gibson and J.R. Blake. The growth and collapse of bubbles near deformable surfaces. *Applied Scientific Research*, 38(1):215–224, 1982.

[121] G.L. Chahine and A. Bovis. Oscillation and collapse of a cavitation bubble in the vicinity of a two-liquid interface. *Cavitation and Inhomogeneities in Underwater Acoustics, Springer Series in Electrophysics*, 4:23–29, 1980.

[122] O. Supponen, P. Kobel, D. Obreschkow, and M. Farhat. The inner world of a collapsing bubble. *Physics of Fluids*, 27(9):091113, 2015.

[123] C.-D. Ohl, O. Lindau, and W. Lauterborn. Luminescence from spherically and aspherically collapsing laser induced bubbles. *Physical Review Letters*, 80(2):393, 1998.

[124] A.M. Zhang, P. Cui, and Y.Wang. Experiments on bubble dynamics between a free surface and a rigid wall. *Experiments in fluids*, 54(10):1–18, 2013.

[125] W. Lauterborn and C.-D. Ohl. Cavitation bubble dynamics. *Ultrasonics sonochemistry*, 4(2):65–75, 1997.

[126] P. Kobel, D. Obreschkow, A. de Bosset, N. Dorsaz, and M. Farhat. Techniques for generating centimetric drops in microgravity and application to cavitation studies. *Experiments in Fluids*, 47(1):39–48, 2009.

[127] Q.X. Wang, K.S. Yeo, B.C. Khoo, and K.Y. Lam. Vortex ring modelling of toroidal bubbles. *Theoretical and Computational Fluid Dynamics*, 19(5):303–317, 2005.

[128] G.L. Chanine and Ph.F. Genoux. Collapse of a cavitating vortex ring. *Journal of Fluids Engineering*, 105(4):400–405, 1983.

[129] M.S. Plesset and R.B. Chapman. Collapse of an initially spherical vapour cavity in the neighbourhood of a solid boundary. *Journal of Fluid Mechanics*, 47:283–290, 1970.

[130] E.-A. Brujan, G.S. Keen, A. Vogel, and J.R. Blake. The final stage of the collapse of a cavitation bubble close to a rigid boundary. *Physics of Fluids*, 14(1):85–92, 2002.

[131] E.-A. Brujan, K. Nahen, P. Schmidt, and A. Vogel. Dynamics of laser-induced cavitation bubbles near elastic boundaries: influence of the elastic modulus. *Journal of Fluid Mechanics*, 433:283–314, 2001.

[132] C.F. Hung and J.J. Hwangfu. Experimental study of the behaviour of mini-charge underwater explosion bubbles near different boundaries. *Journal of Fluid Mechanics*, 651:55–80, 2010.

[133] Y. Tomita and T. Kodama. Interaction of laser-induced cavitation bubbles with composite surfaces. *Journal of Applied Physics*, 94(5):2809–2816, 2003.

[134] P. Gregorčič, R. Petkovšek, and Janez Možina. Investigation of a cavitation bubble between a rigid boundary and a free surface. *Journal of Applied Physics*, 102(9):094904, 2007.

[135] W. Lauterborn. Cavitation bubble dynamics - new tools for an intricate problem. *Applied Scientific Research*, 38(1):165–178, 1982.

[136] J.E. Field. The physics of liquid impact, shock wave interactions with cavities, and the implications to shock wave lithotripsy. *Phys. Med. Biol.*, 36(11):1475–1484, 1991.

[137] R. Hickling and M.S. Plesset. Collapse and rebound of a spherical bubble in water. *Physics of Fluids*, 7(1):7–14, 1964.

[138] S. Fujikawa and T. Akamatsu. Effects of the non-equilibrium condensation of vapour on the pressure wave produced by the collapse of a bubble in a liquid. *Journal of Fluid Mechanics*, 97:481–512, 1979.

[139] D. Fuster, C. Dopazo, and G. Hauke. Liquid compressibility effects during the collapse of a single cavitating bubble. *J. Acoust. Soc. Am.*, 129(1):122–131, 2011.

[140] F. Magaletti, L. Marino, and C.M. Casciola. Shock wave formation in the collapse of a vapor nanobubble. *Physical Review Letters*, 114(6):064501, 2015.

[141] L.K. Wang, Z.F. Zhang, and S.P. Wang. Pressure characteristics of bubble collapse near a rigid wall in compressible fluid. *Applied Ocean Research*, 59:183–192, 2016.

[142] W. Lauterborn and A. Vogel. Bubble dynamics & shock waves. In C.F. Delale, editor, *Shock Wave Science and Technology Reference Library*, volume 8, pages 67–103. Springer, Berlin, 2013.

[143] O. Supponen, D. Obreschkow, M. Tinguely, P. Kobel, N. Dorsaz, and M. Farhat. Scaling laws for jets of single cavitation bubbles. *Journal of Fluid Mechanics*, 802:263–293, 2016.

[144] A. Vogel, S. Busch, and U. Parlitz. Shock wave emission and cavitation bubble generation by picosecond and nanosecond optical breakdown in water. *J. Acoust. Soc. Am.*, 100(1):148–165, 1996.

[145] B. Ward and D.C. Emmony. Direct observation of the pressure developed in a liquid during cavitation bubble collapse. *Applied Physics Letters*, 59(18):2228–2230, 1991.

[146] J.R. Sukovich, P.A. Anderson, A. Sampathkumar, D.F. Gaitan, Y.A. Pishchalnikov, and R.G. Holt. Outcomes of the collapse of a large bubble in water at high ambient pressures. *Physical Review E*, 95(4):043101, 2017.

[147] G.L. Chahine. Interaction between an oscillating bubble and a free surface. *Journal of Fluids Engineering*, 99(4):709–716, 1977.

[148] J.R. Blake and D.C. Gibson. Growth and collapse of a vapour cavity near a free surface. *Journal of Fluid Mechanics*, 111:123–140, 1981.

[149] Q.X. Wang, K.S. Yeo, B.C. Khoo, and K.Y. Lam. Nonlinear interaction between gas bubble and free surface. *Computers & Fluids*, 25(7):607–628, 1996.

[150] A. Pearson, E. Cox, J.R. Blake, and S.R. Otto. Bubble interactions near a free surface. *Engineering Analysis with Boundary Elements*, 28(4):295–313, 2004.

[151] H. Schoeffmann, H. Schmidt-Kloiber, and E. Reichel. Time-resolved investigations of laser-induced shock waves in water by use of polyvinylidenefluoride hydrophones. *Journal of Applied Physics*, 63(46):46–51, 1988.

[152] A.G. Doukas, A.D. Zweig, J.K. Frisoli, R. Blrngruber, and T.F. Deutsch. Non-invasive determination of shock wave pressure generated by optical breakdown. *Applied Physics B*, 53(4):237–245, 1991.

[153] Y. T. Didenko, W. B. McNamara, and K. S. Suslick. Temperature of multububble sonoluminescence in water. *Journal of Physical Chemistry A*, 103(50):10783, 1999.

[154] Y. T. Didenko and K. S. Suslick. The energy efficiency of formation of photons, radicals and ions during single-bubble cavitation. *Nature*, 418(6896):394, 2002.

[155] Y. G. Adewuyi. Sonochemistry in environmental remediation. 2. heterogeneous sonophotocatalytic oxidation processes for the treatment of pollutants in water. *Environmental Science & Technology*, 39(22):8557–8570, 2005.

[156] A. Gedanken. Using sonochemistry for the fabrication of nanomaterials. *Ultrasonics Sonochemistry*, 11(2):47–55, 2004.

[157] T.G. Leighton, M. Farhat, J.E. Field, and F. Avellan. Cavitation luminescence from flow over a hydrofoil in a cavitation tunnel. *Journal of Fluid Mechanics*, 480:43–60, 2003.

[158] M. Farhat, A. Chakravarty, and J.E. Field. Luminescence from hydrodynamic cavitation. *Proceedings of the Royal Society of London A: Mathematical, Physical and Engineering Sciences*, 480(rspa.2010.0134), 2010.

[159] O. Supponen, D. Obreschkow, P. Kobel, M. Tinguely, N. Dorsaz, and M. Farhat. Shock waves from nonspherical cavitation bubbles. *Physical Review Fluids*, 2(9):093601, 2017.

[160] C.-D. Ohl. Probing luminescence from nonspherical bubble collapse. *Physics of Fluids*, 14(8):2700–2708, 2002.

[161] E.A. Brujan and G.A. Williams. Luminescence spectra of laser-induced cavitation bubbles near rigid boundaries. *Physical Review E*, 72(1):016304, 2005.

[162] C. Cairós and R. Mettin. Simultaneous high-speed recording of sonoluminescence and bubble dynamics in multibubble fields. *Physical Review Letters*, 118(6):064301, 2017.

[163] E. Brujan, D.S. Hecht, F. Lee, and G.A. Williams. Properties of luminescence from laser-created bubbles in pressurized water. *Physical Review E*, 72(6):066310, 2005.

[164] L. Zhang, X. Zhu, H. Yan, Y. Huang, Z. Liu, and K. Yan. Luminescence flash and temperature determination of the bubble generated by underwater pulsed discharge. *Applied Physics Letters*, 110(3):034101, 2017.

[165] W. B. McNamara, Y. T. Didenko, and K. S. Suslick. Sonoluminescence temperatures during multi-bubble cavitation. *Nature*, 401(6755):772, 1999.

[166] M.C. Ramsey and R.W. Pitz. Energetic cavitation collapse generates 3.2 mbar plasma with a 1.4 j driver. *Physical Review Letters*, 110(15):154301, 2013.

[167] J. Duplat and E. Villermaux. Luminescence from collapsing centimeter bubbles expanded by chemical reaction. *Physical Review Letters*, 115(9):094501, 2015.

[168] T.J. Matula, R.A. Roy, P.D. Mourad, W.B. McNamara III, and K.S. Suslick. Comparison of multibubble and singe-bubble sonoluminescence spectra. *Physical Review Letters*, 75(13):2602, 1995.

[169] G.M. Hale and M.R. Querry. Optical constants of water in the 200-nm to 200-μm wavelength region. *Applied Optics*, 12(3):555–563, 1973.

[170] R.A. Hiller, S.J. Putterman, and B.P. Barber. Spectrum of synchronous picosecond sonoluminescence. *Physical Review Letters*, 69(8):1182, 1992.

[171] B. Wolfrum, B. Kurz, T. Lindau, and W. Lauterborn. Luminescence of transient bubbles at elevated ambient pressures. *Physical Review E*, 64(4):046306, 2001.

[172] J.R. Sukovich, A. Sampathkumar, P.A. Anderson, R.G. Holt, Y.A. Pishchalnikov, and D.F. Gaitan. Temporally and spatially resolved imaging of laser-nucleated bubble cloud sonoluminescence. *Physical Review E*, 85(5):056605, 2012.

[173] B. Kappus, S. Khalid, and S. Putterman. 100-watt sonoluminescence generated by 2.5-atmosphere-pressure pulses. *Physical Review E*, 83(5):056304, 2011.

[174] B.D. Storey and A.J. Szeri. Water vapour, sonoluminescence and sonochemistry. *Proceedings of the Royal Society London A*, 456(1999):1685–1709, 2000.

[175] R. Toegel, B. Gompf, R. Pecha, and D. Lohse. Does water vapor prevent upscaling sonoluminescence? *Physical Review Letters*, 85(15):3165, 2000.

[176] M. Raffel. Background-oriented schlieren (bos) techniques. *Experiments in Fluids*, 56(3):60, 2015.

[177] S. Yamamoto, Y. Tagawa, and M. Kameda. Application of background-oriented schlieren (bos) technique to a laser-induced underwater shock wave. *Experiments in Fluids*, 56(5):93, 2015.

[178] K. Hayasaka, Y. Tagawa, T. Liu, and M. Kameda. Optical-flow-based background-oriented schlieren technique for measuring a laser-induced underwater shock wave. *Experiments in Fluids*, 57(12):179, 2016.

OUTI SUPPONEN

Born in Brussels, 03.09.1990

Education

2017	Dr. Sc in Mechanical Engineering, École Polytechnique Fédérale de Lausanne
2013	MEng in Aeronautical Engineering, Imperial College London
2011	Erasmus exchange at École Centrale de Lyon
2009	European Baccalaureate, European School of Brussels II

Research experience

Apr-Sep 2012	Intern at the Laboratory for Energy Conversion, ETH Zurich

Awards

Edmund Optics Educational Gold Award 2015
Gallery of Fluid Motion Award, APS DFD 2014

Languages Finnish, French, English, Italian, German

Peer-reviewed publications

Supponen O., Obreschkow D., Kobel P. and Farhat M. "Luminescence from cavitation bubbles deformed in uniform pressure gradients". *Phys. Rev. E* **96**(3) 033114 (2017)

Supponen O., Obreschkow D., Kobel P., Tinguely M., Dorsaz N. and Farhat M. "Shock waves from nonspherical cavitation bubbles". *Phys. Rev. Fluids* **2**(9) 093601 (2017)

Supponen O., Obreschkow D., Tinguely M., Kobel P., Dorsaz N. and Farhat M. "Scaling laws for jets of single cavitation bubbles". *J. of Fluid Mechanics* **802**, pp. 263-293 (2016)

Koukouvinis Ph., Gavaises M., Supponen O. and Farhat M. "Simulation of bubble expansion and collapse in the vicinity of a free surface". *Phys. of Fluids* **28**(5) 052103 (2016)

Koukouvinis Ph., Gavaises M., Supponen O. and Farhat M. "Numerical simulation of a collapsing bubble subject to gravity". *Phys. of Fluids* **28**(3) 032110 (2016)

Supponen O., Kobel P., Obreschkow D. and Farhat M. "The inner world of a collapsing bubble". *Phys. of Fluids* **27**(9) 091101 (2015)

Nedić J., Supponen O., Ganapathisubramani B. and Vassilicos J.C. "Geometrical influence on vortex shedding in turbulent axisymmetric wakes". *Phys. of Fluids* **27**(3) 035103 (2015)

Supponen O., Obreschkow D., Kobel P. and Farhat M. "Detailed Jet Dynamics in a Collapsing Bubble". *J. of Physics, Conference Series*, **656**(1) 012038 (2015)